
Silesian University of Technology
Faculty of Automatic Control, Electronics and Computer Science
Department of Measurements and Control Systems

# Noise and vibration reduction of a device enclosed in a thin-walled casing with the use of structural interactions

Doctoral Dissertation

by

**Anna Chrapońska**

Supervisor
**Prof. dr hab. inż. Marek Pawełczyk**

2022
Gliwice, POLAND

*To my husband Michał*

*and my parents Barbara and Marek*

# Contents

# Abstract

Enhancement of noise level, as a result of vibration of the structures, has been observed along with the technological progress. Different domestic and industrial appliances may generate noise, which can cause damage to human health. Researchers put efforts to reduce exposure to noise and vibration in the environment, and three types of methods may be distinguished: active, semi-active, and passive ones. Also, different types of casings enclosing noise-generating devices may be employed. Many applications of the noise and vibration control methods are examined in an anechoic environment. Thus, a concept of a device casing under active structural acoustic control is further developed, where the casing is placed at a wall or in a corner, to provide intentional interactions between the casing and the reflective surfaces. The casings are frequently built of the single plates, and the field of research on the double-panel structures has not been thoroughly explored yet. Hence, the dissertation introduces also a novel modification of a double-panel structure with solenoids employed as the couplings between the panels.

In the first part of the research, the aim of the experiments was to analyze primary and secondary paths of the lightweight device casing placed at a wall, and to analyze active control performance of the casing placed in a corner. The experiment for the casing placed at a wall provided relevant information about the beneficial distances between the casing and the wall, in terms of magnitude decrease at the specific frequencies. Increase or decrease of the amplitude responses of primary and secondary paths was similar, hence the balance between them was sustained, so they did not have a negative impact on active control performance. Results for the casing placed in a corner showed that the appropriate error microphones' arrangement and a corner-casing distance may lead to global noise reduction level enhancement in a wider frequency range, in comparison to the results obtained inside the acoustic foam-covered laboratory. The error microphones placed in a narrow space between the casing and the corner may negatively impact the active control performance, and for the specific casing-corner distance values it was beneficial to turn them off. The influence of actuators (located on the panels facing the corner) on the active control system performance was examined. The important role of vibrational couplings

between the casing panels was confirmed. The actuators excited the whole casing efficiently and it was equally beneficial to locate them at the panels near to the corner walls as at the opposite side. The research outcome provides a possibility to simplify the control system in a particular configuration by reducing the number of sensors and actuators.

In the second part of the research, panels of the double-panel structure interacted with each other by means of electromagnetic actuators called solenoids. The influence of such setup on vibroacoustic properties of the structure was examined. Five couplings were mounted between the panels, as preliminary setup with one solenoid did not provide satisfactory results. The first experiment was performed with the vibration sensors, and two phenomena were observed. The vibration energy was transferred to different areas of the radiating panel if, for the specific coupling, duty cycle of a modulated voltage signal increased. There was a stronger transfer of vibrations from the incident panel to the radiating one, if all five couplings were activated with a specific duty cycle value of the voltage signal. The central solenoid's activation had the most significant impact on the vibration reduction at the radiating panel. However, the influence of other couplings on vibration reduction at the radiating panel was not without significance, even if they acted as the mass loadings only in a particular configuration. The analysis of radiating panel's vibration in frequency domain indicated that proposed locations of the couplings may provide vibration reduction in a wide frequency band, but to ensure that the best effect is achieved, an optimization algorithm should be developed. Also, an estimate of Sound Transmission Loss was determined. The promising effect of coupling the structure with electromagnetic elements was observed in a wide frequency band, where STL was enhanced. Thus, the modified structure provides satisfactory results in terms of both vibration reduction and noise insulation. It has been confirmed that employment of the double-panel structures for noise and vibration reduction, with the use of additional couplings, is reasonable.

# Streszczenie

Współcześnie, w związku z postępem technologicznym, obserwuje się wzrost poziomu hałasu będącego rezultatem drgań struktur. Hałas generowany przez urządzenia domowe i przemysłowe może powodować uszczerbek na zdrowiu. Wysiłki naukowców skupiają się na redukcji ekspozycji na hałas i drgania w środowisku. Wyróżnia się trzy rodzaje metod redukcji drgań i hałasu: aktywne, półaktywne oraz pasywne. Wykorzystuje się także obudowy mieszczące w sobie urządzenia generujące hałas. Wiele badań dotyczących metod redukcji drgań i hałasu odbywa się w komorach bezechowych bądź w pomieszczeniach, których ściany pokryte są odpowiednim materiałem. Takie warunki nie uwzględniają zjawiska odbijania się fali dźwiękowej od rzeczywistych powierzchni w pomieszczeniach użytkowych. Idea obudowy poddanej aktywnemu strukturalnemu sterowaniu akustycznemu jest zatem rozwijana w środowisku rzeczywistym, z celowo wprowadzonymi interakcjami pomiędzy obudową a powierzchniami odbijającymi. Obudowy mieszczące w sobie urządzenia generujące hałas nierzadko są wykonywane z cienkich pojedynczych paneli, a obszar nauki poświęcony strukturom dwupanelowym wciąż nie został dogłębnie przebadany. Istnieje zatem możliwość zaproponowania nowych rozwiązań wzbogacenia struktur dwupanelowych w celu poprawy ich własności wibroakustycznych. W pracy przedstawiono badania struktury dwupanelowej zmodyfikowanej za pomocą solenoidów jako elementów sprzęgających.

W pierwszej części badań, w celu globalnej redukcji hałasu w pomieszczeniu wykorzystano metodę aktywnej strukturalnej kontroli hałasu. Lekka cienkościenna obudowa urządzenia znajdowała się w dwóch ustawieniach: przy ścianie oraz w narożu. W badaniach przeanalizowano ścieżki pierwotne i wtórne oraz wydajność systemu sterowania. Wyniki dostarczyły informacji o najbardziej korzystnym dystansie pomiędzy obudową a ścianą pod kątem redukcji wzmocnienia ścieżek pierwotnych i wtórnych w określonych pasmach częstotliwości. Wykazano, że wzrost bądź spadek wzmocnienia ścieżek pierwotnych i wtórnych jest zrównoważony, a zatem nie wpływają one niekorzystnie na wydajność systemu sterowania. Wyniki dla obudowy w narożu wykazały, iż odpowiednie ustawienie mikrofonów błędu oraz dobór dystansu obudowa-naroże mogą prowadzić do wzrostu poziomu globalnej redukcji

hałasu w szerszym zakresie częstotliwości niż w pomieszczeniu pokrytym pianką akustyczną. Mikrofony błędu umieszczone w przestrzeni między obudową a narożem mogą negatywnie wpływać na wydajność systemu sterowania i dla wybranych ustawień korzystniej było z nich zrezygnować. Zauważono także wpływ wzbudników na panelach naprzeciw naroża na wydajność systemu sterowania, wynikający ze zjawiska sprzężeń wibracyjnych między panelami obudowy cienkościennej. Wzbudniki efektywnie wzbudzają całą obudowę, stąd umieszczenie ich na przeciwległych panelach jest równie korzystne. Uzasadniono możliwość uproszczenia systemu sterowania w wybranych konfiguracjach pod kątem liczby mikrofonów błędu i urządzeń wykonawczych.

W drugiej części badań wprowadzono interakcje pomiędzy panelami struktury dwupłytowej, używając solenoidów jako elementów sprzęgających. Pomiędzy panelami umieszczono pięć elementów sprzęgających, ponieważ wstępne badania z pojedynczym, centralnym solenoidem nie przyniosły zadowalających rezultatów. Pierwsze eksperymenty przeprowadzono z użyciem czujników drgań. Zaobserwowano zjawiska przenoszenia energii drgań do innych obszarów panelu zewnętrznego w przypadku wzrostu współczynnika wypełnienia sygnału napięciowego dla elementu sprzęgającego, a także silniejszego przenoszenia drgań z panelu wewnętrznego do zewnętrznego, gdy wszystkie solenoidy były włączone i ustawiono odpowiedni współczynnik wypełnienia. Aktywacja centralnego solenoidu miała największy wpływ na redukcję drgań panelu zewnętrznego, jednak nie bez znaczenia pozostaje wpływ pozostałych elementów sprzęgających strukturę dwupanelową, nawet jeżeli w danej konfiguracji pełnią jedynie rolę obciążeń masowych. Analiza drgań w dziedzinie częstotliwości wskazała, iż jest możliwa redukcja drgań w szerokim zakresie częstotliwości w proponowanej konfiguracji, jednak w celu uzyskania możliwie najlepszych efektów należy rozwijać algorytm optymalizacji. Wyznaczono również estymaty STL (z ang. *Sound Transmission Loss*). Ich wzrost zaobserwowano w szerokim pasmie częstotliwości przy zastosowaniu sekwencji opisywanej jako najlepszy przypadek. Modyfikacja struktury dwupanelowej przyniosła zadowalające rezultaty w kontekście redukcji drgań oraz wzrostu izolacyjności akustycznej. Potwierdzono, iż zastosowanie struktur dwupanelowych, z wykorzystaniem solenoidów jako sprzężeń, do celów redukcji drgań i hałasu jest uzasadnione.

# Acknowledgments

The author would like to thank Professor Marek Pawełczyk for his supervision, guidance and excellent support.

The author would also like to thank Jarosław Rzepecki, who was not only a perfect co-worker, but also a true friend and supporter at all times of joint research.

The author would also like to thank members of the Department of Measurements and Control Systems for their precious comments and friendly atmosphere.

The research has been partially supported by the National Science Centre, Poland, under the Grant no. DEC-2017/25/B/ST7/02236.

The greatest thanks are to my Husband, my Family, and my Friends for their love, support and motivation.

# List of Abbreviations

**ANC** — **A**ctive **N**oise **C**ontrol

**ANVC** — **A**ctive **N**oise-**V**ibration **C**ontrol

**ASAC** — **A**ctive **S**tructural **A**coustic **C**ontrol

**FIR** — **F**inite **I**mpulse **R**esponse

**FxLMS** — **F**iltered-**x** **L**east **M**ean **S**quares

**LMS** — **L**east **M**ean **S**quares

**MFC** — **M**acro-**F**iber **C**omposites

**MIMO** — **M**ultiple-**I**nput **M**ultiple-**O**utput

**PSD** — **P**ower **S**pectral **D**ensity

**PWM** — **P**ulse **W**idth **M**odulation

**RMS** — **R**oot **M**ean **S**quare

**SSD** — **S**ynchronized **S**witch **D**amping

**STL** — **S**ound **T**ransmission **L**oss

# List of Symbols

| | |
|---|---|
| $\alpha$ | Absorption coefficient |
| $\Delta$ | Distance of a sound source |
| $\eta$ | Loss factor |
| $\gamma$ | Damping ratio (Chapter 4.3.3) |
| $\gamma$ | Mass of a panel per unit area (Chapter 4.3.2) |
| $\hat{S}(z)$ | Model of a secondary path |
| $\nu$ | Poisson ratio |
| $\omega$ | Angular frequency |
| $\phi_{mn}(x, y)$ | Mode shape function |
| $\Pi_{in}$ | Incident sound power |
| $\Pi_r$ | Transmitted sound power |
| $\rho$ | Mass density per unit volume of a panel |
| $\rho_0$ | Air density |
| $\tau$ | Transmitted to incident pressure power ratio coefficient |
| $\theta$ | Elevation angle of an incidence sound wave |
| $\varphi$ | Azimuth angle of an incidence sound wave |
| $a$ | Width of a panel |
| $a_i$ | Damping coefficient of an $i$th panel |
| $b$ | Height of a panel |
| $c$ | Speed of sound in air |
| $d$ | Cavity depth of a double-panel structure (Chapter 4) |

| | |
|---|---|
| $d$ | Distance between a lightweight casing and a wall/corner (Chapter 3) |
| $d(n)$ | Primary disturbance |
| $D_i$ | Flexural rigidity of an $i$th panel |
| $E$ | Young's modulus |
| $e(n)$ | Residual error signal |
| $f$ | Frequency |
| $f_{mn}$ | Resonant frequency ($m$, $n$) |
| $G$ | Rigidity modulus |
| $h$ | Thickness of a panel |
| $k$ | Wave number |
| $k_x, k_y, k_z$ | Components of a wave vector $\mathbf{k}$ |
| $M$ | Loading's mass |
| $m_i$ | Area mass of $i$th panel (Chapter 4.3.4) |
| $n$ | $n$th sample |
| $p$ | Sound pressure at the wall's surface |
| $P(z)$ | Primary path |
| $q(x, y)$ | Lateral static loading |
| $R$ | Complex reflection factor |
| $r(n)$ | Filtered reference signal |
| $S(z)$ | Secondary path |
| $t$ | Continuous time |
| $u(n)$ | Output of an adaptive filter |
| $v_n$ | Velocity component normal to the wall |

| | |
|---|---|
| $W(x, y)$ | Panel lateral displacement's amplitude |
| $W(z)$ | Control filter |
| $w_i$ | Transverse displacement $i$ of a panel |
| $x(n)$ | Reference signal |
| $x, y$ | Space coordinates |
| $X_m(x), Y_n(y)$ | Independent beam functions |
| $Z$ | Wall impedance |
| $z$ | Complex variable, time shift operator |

# List of Tables

# List of Figures

# 1. Introduction

## 1.1. Research background

Nowadays, due to the technological progress, noise level enhancement has been observed as a result of structures' vibrations. Machines and devices commonly used in industry, and in everyday life, generate noise, which may cause health damage [1]. The risk of a harmful effect on human health depends on the duration of exposure to noise as well as on the noise frequency [2]. Lack of control of these factors is especially dangerous to employees in the industrial work environment [3]. Noise is one of the factors influencing mental performance [4]. Environmental noise may cause many different diseases, e.g. stroke, heart disease, depression or lower job performance [5, 6, 7]. Therefore, high efforts are made to reduce the noise pollution in the human environment.

As the number of industrial equipment (e.g. engines, blowers, fans, compressors) increases, the issue of acoustic noise enlarges [8]. Appliances such as ventilation systems, fans, pumps are, among others, the main sources of low frequency noise [4], which is of main interest in this research. There are many types of environmental noise sources, such as transportation (railway [9, 10], aircraft [11, 12], wind turbines [13], coastal and port activities [14]).

Another problem is mechanical vibration, met as a source of noise in transportation, manufacturing and household appliances [8]. For instance, vibration frequencies in the seat suspensions have an impact on human body systems [15]. The process of mechanical vibration consists of four main stages (Fig. 1): generation, transmission, propagation and radiation, which entail different types of problems [16]. For instance, typical issues related to generation stage are misalignments and unbalances. At the transmission stage, an issue of shock and vibration isolation has to be faced. Damping is an example of an issue related to propagation, while radiation stage is related to sound transmission and radiation.

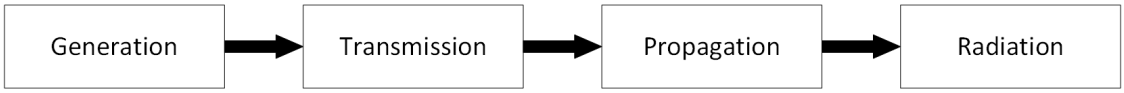


Figure 1: The process of mechanical vibration (based on [16]).

Exposure to vibration is especially dangerous at low frequencies up to 100 Hz [17]. Health damage caused by vibration depends on its source. For instance, floor vibration leads to negative health effects on workers in offices [18]. Skeletal pathologies may be caused by handheld machines [19].

The goal of research in the field of noise and vibration control is to reduce exposure to both noise and vibration in the environment. The solution depends on the examined case: for instance, in an urban space, Bus Signal Priority may be employed to reduce road traffic noise [20]. Modeling is typically an important part of the whole process [21, 22].

Three main types of methods to reduce noise and vibration exist, i.e. active, semi-active and passive ones. Each of them is described in the following Chapter 1.2.

## 1.2. Methods for noise and vibration reduction

### 1.2.1. Passive methods

In a passive approach to reduce air-borne noise, different objects may be employed, e.g. mufflers, barriers, absorbers, silencers [23]. For reduction of the structure-borne vibration and noise, change of mass or stiffness of the system may be sufficient, but sometimes isolators or damping materials have to be employed to isolate or dissipate the vibration [23]. However, passive sound absorbers are not efficient at low frequencies, because the acoustic wavelength becomes large in comparison to an absorber's thickness, and such solution is expensive in terms of weight and bulk [24].

### 1.2.2. Active methods

Active control methods may be employed in the noise and vibration control systems alternatively or complementary to other solutions [25, 26, 27, 28]. In the active control systems, external sources are driven to achieve a minimization of sound and/or vibration [29]. Such approach may be employed e.g. to control noise which enters through open windows [30, 31]. Vibration may be reduced with an active approach employed e.g. by means of thin wall casings built of modern materials [32].

Different active approaches to reduce noise and vibration exist. The classical concept of Active Noise Control (ANC), where the secondary sources are employed to cancel noise from the primary source, has been under rapid development since 1990s. In many cases, it turned out to be less expensive and more efficient than the passive methods, at the low frequencies of sound [33, 34]. ANC is based on the superposition principle. Algorithm's operations are usually performed in an adaptive way due to changes in acoustic field or structural properties [35]. One of the main disadvantages of the classical active control approach is that the noise is reduced only in limited local zones while being reinforced at other areas. Hence, such solution may be insufficient if people are moving inside an enclosure or if the noise is nonstationary [36]. Another disadvantage is a need to introduce a high number of secondary sources, which implies an increase of both cost and environmental burden [37]. Other solutions have therefore emerged, such as Active Noise-Vibration Control (ANVC) or Active Structural Acoustic Control (ASAC).

In ANVC systems, the desired acoustic control source is produced by exciting the flexible enclosure walls with the use of inertial or strain actuators [29]. The different approach is ASAC, which takes advantage of structural actuators (e.g. shakers or piezoelectric patches [38]) integrated into the walls to reconstruct their vibration [29].

### 1.2.3. Semi-active methods

In case of semi-active methods, system properties can be modified without providing external energy to the system [39]. Also, stability of the system is ensured. Semi-active methods, in contrast to the passive ones, are robust to changing environmental conditions [40].

Hybrid methods have the benefits of both passive and active techniques [41]. SSD, Synchronized Switch Damping, is one of the examples. It is robust to environmental variation [42].

## 1.3. Single panels versus double-panel structures

For the purpose of noise and vibration reduction, a casing enclosing noise-generating device may be employed. Such casing may be built of single- or double

panels, depending on the research scenario. In this dissertation, both single panels and double-panel structures are used as the walls of the employed device casings. Double walls have several advantages over single panels, as described below. The simple scheme of a double-panel structure is presented in Figure 2. Double-panel

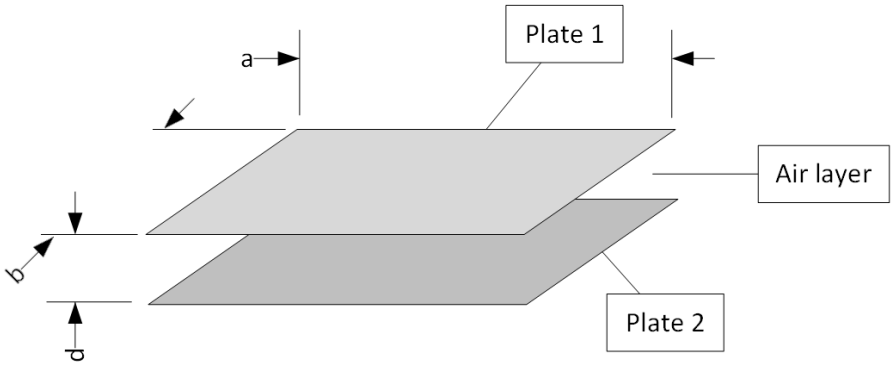


Figure 2: Double-panel structure: basic scheme.

structure consists of two panels with the dimensions of $a \times b$ and a fluid layer between them. In this dissertation, the considered fluid is air. The distance between panels, $d$, is called the cavity depth.

Double-panel structures are characterized by better sound insulation properties than single panels [43]. Better sound insulation of a structure implies greater sound energy dissipation and a decrease of vibration power [44]. Another advantages of the double-panel structures are: high stiffness-to-weight ratio, high strength and good thermal isolation [45]. The use of double-panel structures is observed in many branches of industry, such as: railway vehicles [46], underwater marine [47], turbofans [48], aerospace [49, 50], buildings and transportation [51]. They are employed in both passive [52, 53] and active systems [54, 55, 56, 57].

To specify acoustic performance of a double-panel structure, different indicators may be used, e.g. Sound Transmission Loss (STL) [58]. STL is commonly used in research as a criterion of noise reduction [52]. It is employed in the room acoustics as sound reduction index R [59], which relates to a sound transmission between two enclosures [29]. In case of double-panel structures, STL estimation is more complex due to the interactions between the panels and the enclosed fluid cavity, and multiple resonances may be observed in STL estimate [53]. In case of finite double-panel structures, boundary conditions were identified as one of the factors

influencing STL estimation [60].

One of the important advantages of the double-panel structures is a possibility to add the links between the panels [61]. The energy transmission is then influenced by structural details, cavity dimensions, and links' properties [62]. For instance, Mao and Shen [63] proposed a mass-spring-damper system to improve STL of a double-panel structure. Mao [64] later also examined Electromagnetic Shunt Damper. Oleyade [65] proposed a model of clamped double wall with magnetic stiffness. Langfeldt et al. [66] examined Helmholtz resonators between the double panels.

It has to be emphasized that the use of double-panel structures may have drawbacks. In the low frequency band, acoustic performance of a double-panel structure may be worse than that of a single panel due to the mass-air-mass resonance phenomenon [67, 56, 68]. In such situation, an active control approach may be applied [69]. Acoustic performance of a double wall may also be improved with the use of absorbents in the cavity between the panels [70, 71]. With such a core, the structure is considered as a sandwich panel [72]. For instance, Shen et al. [73] improved double wall's sound insulation property by introducing a poroelastic core. Gulia and Gupta [74] used glass wool filter and Sonic Crystal assembly in their sandwich panel to improve STL. De Melo Filho et al. [75, 76] examined locally resonant metamaterials and metamaterial foam core sandwich panel. Fu et al. developed a model of orthogonally rib-stiffened double laminated composite plates structure [77]. Qiao et al. [78] examined a periodically rib-stiffened double panel with porous lining. Another approach may be the light-weight micro-perforated panels resistant to humidity [79, 80].

In this dissertation, an outcome of the author's research in the field of double walls is described. Scenarios with one [39] and five [81, 82] couplings between the panels were examined. The author of this thesis along with other research project team members submitted three Polish patent applications [83, 84, 85] in which three theoretical concepts of links between the double panels were proposed: active, semi-active and passive ones.

## 1.4. Motivation for the research

Many applications of methods for noise and vibration reduction are examined in an anechoic laboratory environment. Such conditions do not take into account an effect of sound reflections in the real enclosures. This dissertation further develops a novel approach to active structural acoustic control by means of lightweight device casing interacting with a reflective wall and a corner, proposed originally by Prof. Pawełczyk's team at the Department of Measurements and Control Systems. Such approach is closer to reality than the experiments performed in a laboratory enclosure whose walls are covered with acoustic foam.

Also, devices are frequently enclosed within simple single-panel casings, and the field of double-panel structures has not been thoroughly examined yet. Hence, there exist many possibilities to introduce novel modifications between the panels of the double-panel structures for the purpose of their vibroacoustic performance's enhancement. A novel concept in the field of modified double-panel structures is presented and examined, as there is not any previous research, known to the author, which would consider insertion of the solenoids between the double panels to improve the vibroacoustic properties of the structure.

## 1.5. Objective and thesis of the dissertation

The main objective of the dissertation is to contribute to the idea of the use of structural interactions as a method to reduce noise and/or vibration generated by a device enclosed in a thin-walled casing.

The thesis is formulated as follows:

**Specific applications of interactions in a double-panel structure, or between device casing panels and reflective enclosure walls, may be deployed to improve vibroacoustic properties of the casing, which implies reduction of radiated noise and vibration.**

## 1.6. Contents of the dissertation

The dissertation consists of a total number of five chapters. The first, following chapter is an introduction, describing briefly methods to reduce noise and vibration;

as well as single panels and double-panel structures, which are used to build the walls of the device casings employed in the research.

Chapter 2 presents laboratory equipment used in the described research to perform experiments. Both lightweight and rigid casings enclosing noise-generating device are presented and discussed. The use of selected sensors and actuators as part of the laboratory setup is explained.

Chapter 3 describes research experiments performed with the use of lightweight device casing. The casing is placed intentionally at a wall and in a corner, both of which are composed of reflective surfaces characterized by a low absorption coefficient. Active Structural Acoustic Control method is applied to achieve global noise reduction in the enclosure. Primary and secondary paths, as well as active control system performance, are discussed.

Chapter 4 describes research dedicated to the double-panel structures. Different models for both single and double panels are analyzed and implemented to better understand their vibroacoustic properties. A double-panel structure modification consisting of solenoids between the panels is examined experimentally. Scenarios with one and five solenoids between the panels are analyzed. The influence of introduced modification on vibroacoustics of the rigid device casing is determined in several ways.

Chapter 5 contains conclusions, author's contributions, and perspectives for future research.

# 2. Laboratory equipment

## 2.1. Lightweight device casing

Device casing used in the research described in Chapter 3 is a lightweight steel casing [86]. It is placed inside a laboratory enclosure, whose walls are covered with a sound-absorbing foam. Figure 3 presents the lightweight device casing placed in a reflective corner (such setup is described in details in Chapter 3.3.2). The lightweight device casing has been employed in numerous research studies, e.g. [36, 86, 87, 88, 89, 90].

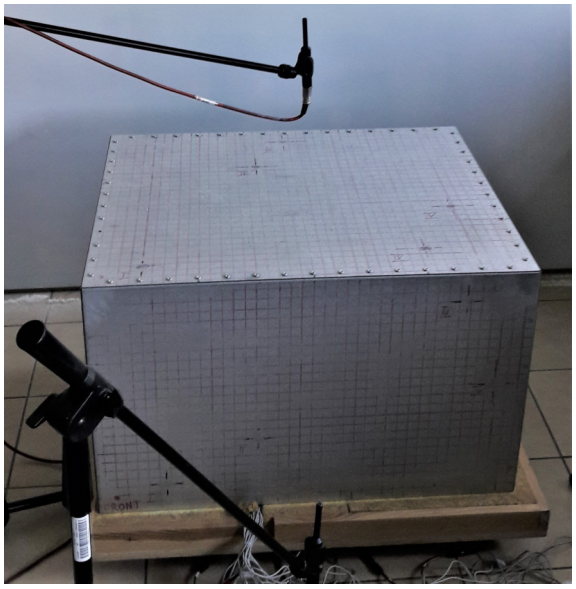

Figure 3: The lightweight device casing.

Lightweight casing has the dimensions of 500 mm × 630 mm × 800 mm. Each of its walls, except the sound-insulated basis, is built of 1 mm thick steel panel. Panels are bolted together at the corresponding edges [91]. In contrary to a rigid casing (Chapter 2.2), the panels are not attached to any kind of frame — they form a self-supporting structure.

## 2.2. Rigid casing

The rigid device casing has been employed in numerous research studies, e.g. [92, 93, 94, 95, 40, 81, 39, 96, 97]. It has the external dimensions of 600 mm × 600 mm × 600 mm [98]. It is composed of a heavy frame made of profiles

(Figure 4) and the panels, which build casing walls along with the smaller frames (Fig. 5). The additional small frames are used to attach the panels to the heavy frame in 20 points each. Such assembly provides boundary conditions which are assumed to be fully clamped at the panels' edges. It is assumed that if a panel has the dimensions of $a \times b$, then its transverse displacements $w_1$ and $w_2$ can be defined as follows [99]:

$$x \in \{0, a\}, \quad 0 \leq y \leq b, \quad w_1 = w_2 = 0, \quad \frac{\partial w_1}{\partial x} = \frac{\partial w_2}{\partial x} = 0; \tag{1}$$

$$y \in \{0, b\}, \quad 0 \leq x \leq a, \quad w_1 = w_2 = 0, \quad \frac{\partial w_1}{\partial y} = \frac{\partial w_2}{\partial y} = 0. \tag{2}$$

The basis of the casing is covered with acoustic foam. Other walls of the casing are built of panels. Each panel has the dimensions of 460 mm × 460 mm before the assembly. After the assembly to the heavy frame by means of a smaller frame, the vibrating surface of each panel has the dimensions of 420 mm × 420 mm.

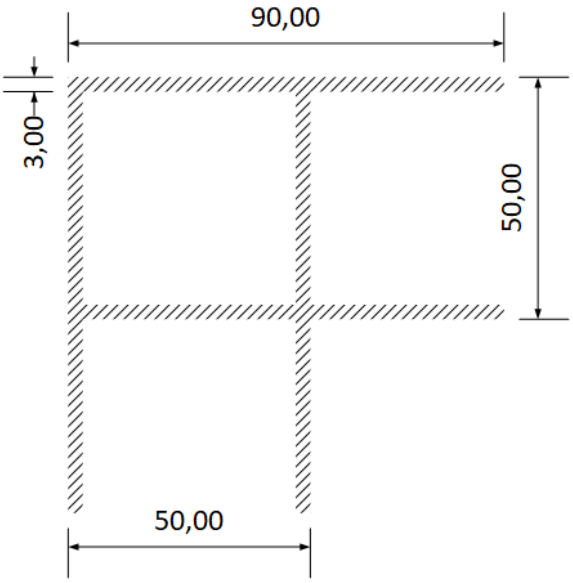


Figure 4: Profiles: cross section (dimensions in mm).

Figure 6 shows a photograph of the rigid device casing.

## 2.3. Sensors and actuators

### 2.3.1. NXT EX-1 exciters

In the research with lightweight device casing, due to the use of ASAC algorithm, exciters were employed to control vibration of the casing walls. As the actuators,

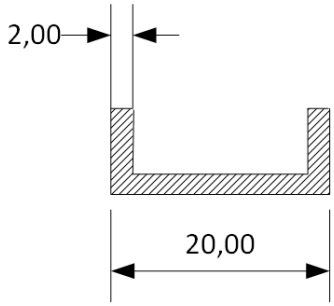


Figure 5: Smaller frame: cross section (dimensions in mm).

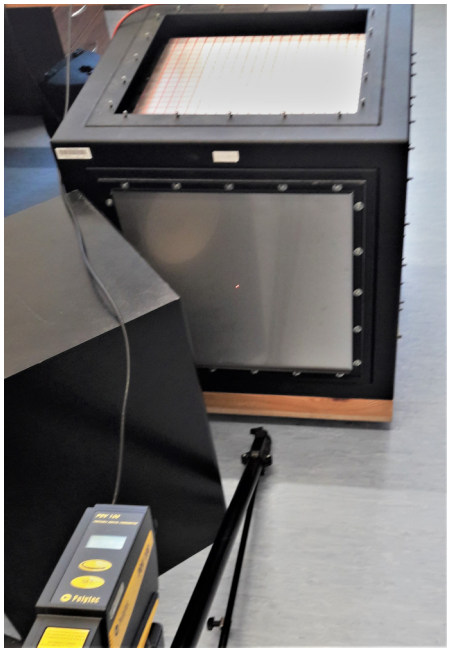

Figure 6: Photograph of the rigid device casing.

lightweight NXT EX-1 exciters were used. Properties of EX-1 Exciter Speaker are listed in Table 1.

Table 1: Properties of EX-1 Exciter Speaker [100].

| | |
|---|---|
| power | 5 W |
| weight | 115 g |
| dimensions | ⌀ 70 mm × 19 mm |

As the lightweight device casing is considered, the inertial mass actuators EX-1 are mounted on the inner side of the casing panels. There are 5 exciters on the top casing wall, and a total number of 4 actuators on each of: left, right, back and front casing walls. Hence, there are 21 exciters employed in this research. Number and placement of the actuators was specified by Wrona and Pawełczyk [86] in the

process of optimization, whose goal was to maximize a measure of the controllability of the system.

### 2.3.2. Beyerdynamic MM-1 microphones

Microphones were used as the sensors in the experiments with both lightweight and rigid casing. In the experiments with the lightweight device casing, ten microphones were employed: one as a reference microphone, five ones as the error sensors, and four ones as the monitoring/room sensors. The use of room microphones was necessary due to the active control employment, as its performance in terms of global noise reduction had to be determined. In the experiment with the rigid casing, two microphones were used to obtain the Sound Transmission Loss estimates: one as a reference sensor inside the casing and one as the outer microphone placed at a specified distance from the radiating panel of the casing's double wall.

In the experiments, Beyerdynamic MM-1 measurement microphones were used. Photograph of a sensor is shown in Figure 7.

Figure 7: Beyerdynamic MM-1 microphone.

Properties of Beyerdynamic MM-1 microphones are listed in Table 2.

Table 2: Properties of Beyerdynamic MM-1 microphones [101].

| | |
|---|---|
| directional characteristic | omnidirectional |
| frequency range | 20–20000 Hz |
| maximum Sound Pressure Level | 122 dB |
| weight | 88 g |
| capsule diameter | 9 mm |
| dimensions | 133 × 19/9 mm |

### 2.3.3. MFC M8514-P2 patches

Macro-Fiber Composite (MFC) M8514-P2 patches were used as the vibration sensors in the research with double-panel structures. They were attached to the radiating (outer) panel of the structure. Such setup is described in details in Chapter 4.2.2. Properties of MFC M8514-P2 elements are presented in Table 3.

Table 3: Properties of MFC M8514-P2 elements [102].

| | |
|---|---|
| active length | 85 mm |
| active width | 14 mm |
| overall length | 100 mm |
| overall width | 18 mm |
| capacitance | 138 nF (± 20%) |
| free strain | -630 ppm (± 10%) |
| blocking force | -76 N (± 10%) |

Figure 8 presents MFC elements glued to the radiating panel of the casing's double wall.

Figure 8: MFC elements glued to the radiating panel of the casing's double wall.

MFCs were attached to the outer panel of the double-panel structure to measure its vibration, as piezocomposites are characterized by their high-quality properties, e.g. high flexibility and low weight [103]. MFCs are an important type of smart materials, producing electrical charge while exposed to mechanical deformations [104].

Placement of MFCs on the radiating panel can be specified arbitrarily or determined in the optimization process. Proper localization of piezocomposites guarantees observability of all modes considered in modal analysis.

### 2.3.4. Solenoids

In the research dedicated to the double-panel structures, solenoids as the electromagnetic couplings between the panels of a double-panel structure were employed. Their properties are shown in Table 4.

Table 4: Properties of a solenoid.

| | |
|---|---|
| total mass | 35 g |
| maximum voltage | 12 V |
| maximum current | 1.5 A |
| maximum stroke | 10 mm |
| maximum force | 5 N |

Solenoid consists of a ferromagnetic coil and a core. When the voltage is applied to the coil, an electromotive force is induced inside the coil. Hence, ferromagnetic core is being held inside the coil, while it is supplied by voltage. If voltage is 0 V, then core is able to move freely inside the coil, and both components of the coupling act as a mass loading.

The solenoid coils were mounted to the outer side of the incident panel, and the cores were mounted to the inner side of the radiating panel. Figure 9a presents ferromagnetic core with the mounting element used in the preliminary experiment, where only one solenoid was placed between the panels' centres. Figure 9b presents a coil with the mounting element used in the same preliminary experiment.

In the preliminary experiment, core was mounted to a plastic wheel and glued to the radiating panel's inner surface by means of a double-sided tape. Figure 9c presents ferromagnetic core (with the mounting element) placed inside the coil already attached to the inner panel. Such concept of assembly turned out to be ineffective because of the influence of heat and vibration on the mounting elements. Hence, in the next experiments, thin blades were used instead of plastic wheels in case of ferromagnetic cores. Each core was glued to the corresponding blade, and

the whole component was then glued to the radiating panel's inner surface. The mounting element, in case of coils, was replaced by 3D-printed plastic element designed by J. Rzepecki. The coils where then mounted to the printed elements, which in turn were glued to the incident panel's outer surface.

The couplings were supplied with voltage signal modulated by means of Pulse Width Modulation (PWM) method. Duty cycle of a PWM signal characterized by a peak-to-peak voltage equal to 11 V was set in range from 0% to 99%.

(a) (b) (c)

Figure 9: Assembly of a solenoid in a preliminary experiment: (a) Ferromagnetic core with the mounting element. (b) Coil with the mounting element. (c) Ferromagnetic core with the mounting element placed inside the mounted coil.

# 3. Structural interactions between the device casing and an enclosure

## 3.1. Introduction

In this dissertation, among other topics, the influence of structural interactions between the lightweight device casing and the reflective enclosure walls on the global noise reduction levels is analyzed. In the experiments performed prior to the research described in this dissertation, the lightweight device casing was placed in a laboratory enclosure, whose walls were covered with sound-absorbing foam and there were no reflective surfaces near the casing panels. Hence, sound reflections from the laboratory walls were neglected.

In the following Chapter, a different approach is described, with the casing intentionally placed at a reflective wall and in a corner, to check the influence of such setup on an active control performance. The distance was chosen to be small enough to provide a substantial influence of sound reflections on active control performance. The aim of these experiments was to analyze primary and secondary paths of the lightweight device casing placed at a wall — with intentional sound reflections from the reflective wall, and to analyze active control performance of a lightweight device casing placed in a corner. The outcomes from the described experiments were also published in [89, 36], as the results were relevant, and the following analyses are partially based on these findings.

Device casing interacts with a reflective enclosure wall. Hence, selected fundamentals of a theory in the field of acoustical engineering had to be reviewed. The author focused on selected fundamentals of the room acoustics, sound reproduction, and low-frequency loudspeakers. The review is presented below, in Chapter 3.1.1.

### 3.1.1. Selected fundamentals of the room acoustics

As the presented research is focused on the low-frequency noise and takes into account an influence of reflective surfaces, the basic idea of subwoofers (low-frequency loudspeakers) was examined. During the process of designing a low-frequency loudspeaker, assumed acoustical properties have to be taken into account, for instance

sound response quality. A subwoofer should be characterized by small size (especially in home theaters) and high output capability [105] to ensure flat response in the low frequency range. However, an improvement of bandwidth comes at the expense of size and efficiency [105]. A specific type of subwoofers, where a cone is towards a floor, is called down-firing or downward-facing (Fig. 10) [105]. Many innovations have been introduced in the field of low-frequency loudspeakers. The example may be a honeycomb speaker system [106] or an active room compensation setup [107] in which an optimal arrangement of a loudspeaker may lead to its smooth low frequency response and the room modes cancellation [108].

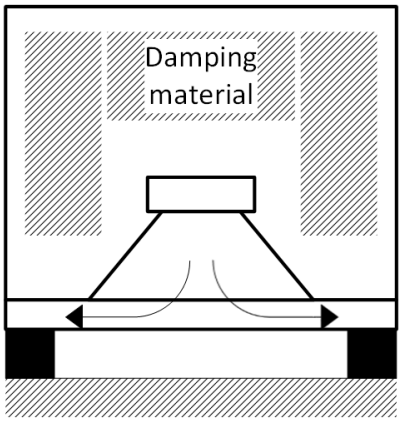


Figure 10: Downward-firing subwoofer (based on [105]).

Long et al. [109] state that coupling a low-frequency loudspeaker to one or more reflecting surfaces may increase its efficiency and overall output, if the distance is less than or equal to one-sixth of a wavelength. In case of low-frequency loudspeakers, the best effects are expected if subwoofer is coupled to a wall on a solid floor or placed in a room corner. Subwoofer coupled to a hard reflecting surface at a distance of one-sixth of a wavelength is characterized by an increased efficiency because the geometrical directivity increases the power output for the same voltage input [110]. It is achieved due to the sound reflections from the nearby surfaces. Exact placement of a subwoofer in a corner influences an excitation of the room modes. If a subwoofer is placed exactly in a corner, the greatest number of the room modes is excited. If it is not desirable to pour energy into the fundamental axial modes, the subwoofer should be placed at an intermediate point along the floor-wall junction [110].

Another aspect is the process of plane sound wave reflection by a surface. Wall impedance and absorption coefficient are of special importance in this field [111].

Absorption coefficient is used to specify whether the wall is soft or rigid. It can be defined as [111]:

$$\alpha = 1 - |R|^2; \tag{3}$$

where $R$ is a complex reflection factor dependent on the incident wave's frequency and direction. The fully absorbent walls are characterized by an absorption coefficient equal to 1. If the wall is rigid, then its absorption coefficient is close to 0 and the maximal reflectivity is 1. In case of soft wall, $R$ is equal to -1.

The wall impedance describes the physical behaviour of a wall and is characterized by the following equation [111]:

$$Z = \left(\frac{p}{v_n}\right)_{\text{surface}}; \tag{4}$$

where $v_n$ is a velocity component normal to the wall and $p$ is a sound pressure at the surface. The reciprocal of $Z$ is called wall admittance.

The idea of downward-firing subwoofer was adapted to a setup with a lightweight casing and the flat reflecting surfaces. Active control approach is considered effective in the low frequency band, hence a sound emitted by a loudspeaker placed inside a casing is characterized by a frequency up to 500 Hz. It was examined if active control performance can be maintained or even improved by placing a device casing at a wall or in a corner.

Another important aspect in the field of room acoustics is the possible existence of room modes. If the modes of the enclosure are within the examined frequency range, they may influence performance of sensors and actuators in the control system. Hence, besides the use of a reflective wall and a corner in the experiments described in this dissertation, walls of the laboratory enclosure were covered with pyramid acoustic foam panels to diminish room modes influence on the measurements.

## 3.2. Lightweight device casing placed at a wall

### 3.2.1. Laboratory setup

In the experiments with the lightweight device casing (described in Chapter 2.1) placed at a wall, a noise-generating device (loudspeaker) is placed inside the casing.

Loudspeaker acts as a primary noise source and is located on a sound-insulated basis.

Inside the casing, a microphone is placed as a reference sensor. As the error sensors, four microphones are placed outside the casing, at the distance of 500 mm from the corresponding casing panels: left, right, front and top ones. As the casing is placed towards the reflective wall with its back panel, error sensor is not located between this panel and the wall, as space is too narrow to put a microphone there.

On the panels of the lightweight device casing, NXT EX-1 exciters are mounted as the actuators, which control the vibration of the casing panels. Actuators' operation is determined based on the signals acquired by the error microphones. Explanation of exciters placement optimization process is described in details in [86].

Laboratory enclosure walls are permanently covered with the pyramid acoustic foam panels. As the scenario of device casing placed at a reflective wall was examined, the rigid wall had to be placed in the enclosure additionally. The assumption was that the wall should be characterized by high density and smoothness to provide the lowest possible absorption coefficient of its surface. It also should be lightweight and prepared similarly to a typical enclosure wall. As a basis for the wall, Oriented Strand Board (OSB) panel was selected. The plasterboard was mounted as the surface layer. After the assembly, measured wall thickness was 30.5 mm, and the dimensions of the wall were 2.6 m $\times$ 2.07 m [89]. The plasterboard surface was covered with a layer of primer and two layers of oil-based gloss paint to lower its absorption coefficient.

Plasterboard is considered a reflective material in industry and is characterized by the low absorption coefficient values in a broad frequency range (Table 5).

Table 5: Absorption coefficient of a plasterboard versus frequency [112].

| Frequency / Material | 125 Hz | 250 Hz | 500 Hz | 1 kHz | 2 kHz | 4 kHz |
|---|---|---|---|---|---|---|
| Plasterboard | 0.29 | 0.1 | 0.06 | 0.05 | 0.04 | 0.04 |

The experimental setup is presented in Figure 11. The scheme of the lightweight device casing placed at a wall with an experimental setup of error microphones is shown in Figures 12a–12b. Figure 12b presents a close-up of the error sensors' setup

Figure 11: Experimental setup of the lightweight device casing placed at a wall.

in relation to the device casing. Both schemes were created with the use of free online modeling software — SketchUp [113].

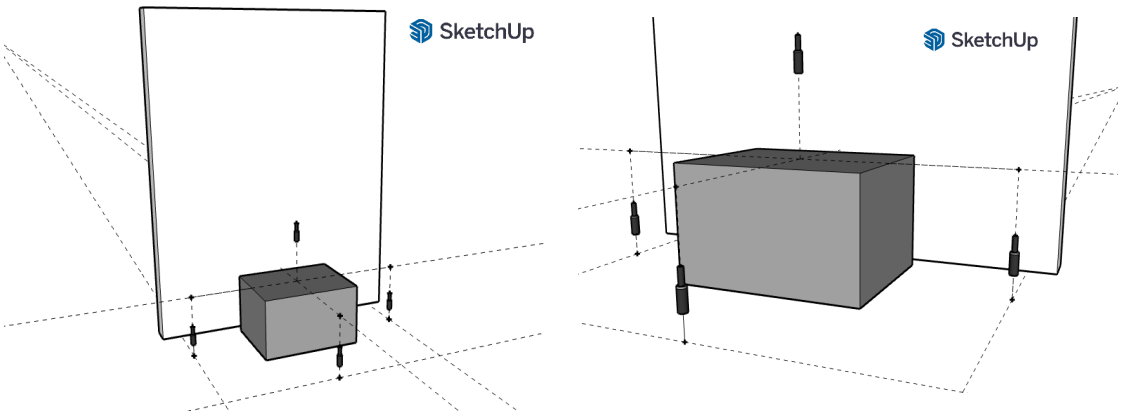


(a) (b)

Figure 12: (a) Scheme of the lightweight device casing placed at a wall. (b) A close-up on the arrangement of error sensors.

The lightweight device casing is located at the wall with its back panel, at a specific distance $d$. As stated in Chapter 3.1.1, low-frequency loudspeakers are the most efficient when coupled to a reflective surface at a distance less than or equal to one-sixth of a wavelength:

$$d \leq \frac{c}{6 \cdot f}. \tag{5}$$

Hence, to cover a low frequency range of noise, distance $d$ values between the

casing's back panel and the wall were selected, taking this rule into account. The group of distances between the casing and the wall was selected arbitrarily: both shorter and greater ones were included. Table 6 presents a comparison of selected distance $d$ values and the frequencies corresponding to them as in Eq. (5), with the assumption that the speed of sound in air ($c$) at 20 °C is equal to 343.21 m/s. Hence,

Table 6: Distance values versus frequencies.

| Distance $d$ [m] | Frequency $f$ [Hz] |
|---|---|
| 0.035 | 1634.3 |
| 0.055 | 1040 |
| 0.075 | 762.7 |
| 0.095 | 602.1 |
| 0.115 | 497.4 |
| 0.135 | 423.7 |
| 0.235 | 243.4 |
| 0.335 | 170.8 |

low frequencies were covered, and the upper ones were added as the second group.

### 3.2.2. Primary paths analysis

The research described in the following Chapter was also published in [89], and the following analysis applies to the same experiments, but presents also a novel and extended description of the results. Both primary and secondary paths' models were obtained as Finite Impulse Response (FIR) models' of length equal to 512 [89]. The paths were identified with the use of multi-sinusoidal signal. Frequency sampling was set to 2 kHz [89]. The amplitude function of the identified impulse response estimate is referred to below as amplitude response [36]. Primary path is an acoustic path between an input, which is primary noise (reference signal), and the signal acquired by one of the error microphones. Reference signal is measured by a reference microphone placed inside the casing. Hence, in this research, primary paths are considered as the paths between a loudspeaker placed inside the casing, and the error microphones corresponding to the left, right, top and front panels of the device casing, respectively (Figs. 13a–13d).

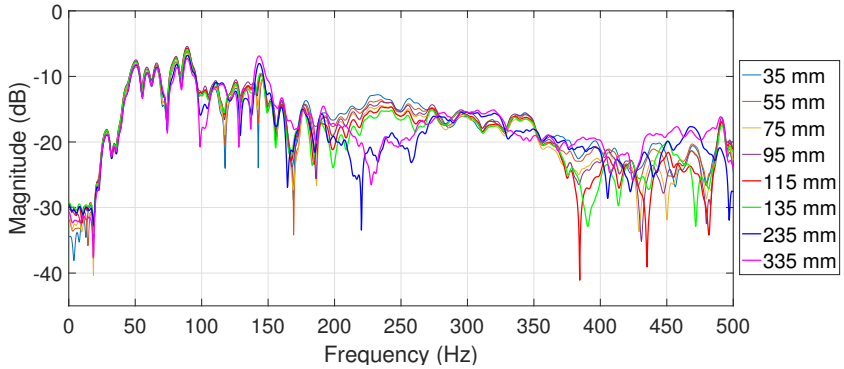


(a)

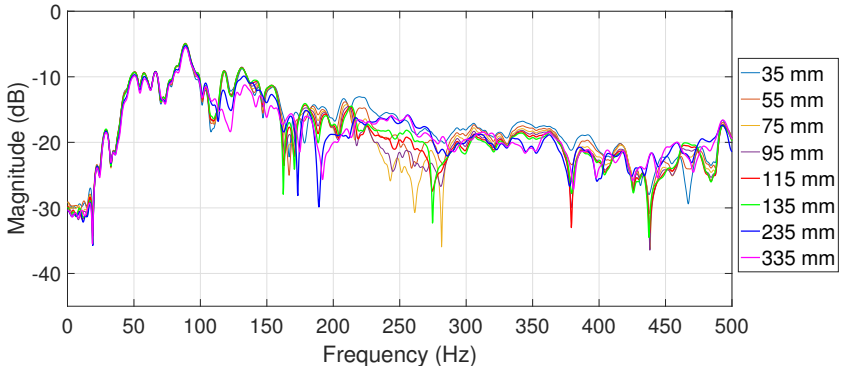


(b)

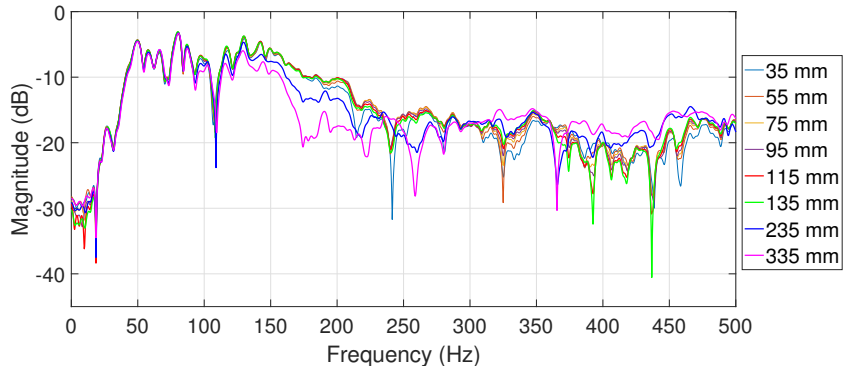


(c)

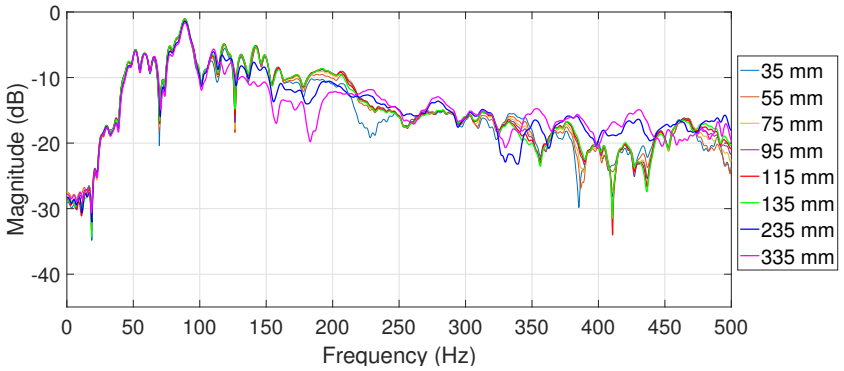


(d)

Figure 13: The amplitude functions of the frequency functions of the impulse response estimates for the primary paths between the primary noise source and the: (a) front, (b) top, (c) left, and (d) right error microphones, at all examined distances.

The amplitude functions of the frequency functions of the impulse response estimates for the primary paths selected for further analysis are presented in Figs. 13a–13d. The frequency range is up to 500 Hz on the graphs. Y axis range is set from −45 dB to 0 dB to maintain consistency of the graphs. As half of the distances cover the low frequency band (Table 6), curves corresponding to them are emphasized on the graphs with wider lines and brighter colors. These distances are referred to below as Group 1 (115 mm, 135 mm, 235 mm, 335 mm) [89]. The second group of distances is referred to below as Group 2 (35 mm, 55 mm, 75 mm, 95 mm) [89].

Figure 13a presents comparison of the amplitude functions of the frequency functions of the impulse response estimates for the primary paths between the primary noise source and the front error microphone, at all examined distances. The front error microphone is the one located at the distance of 500 mm from the casing front panel's centre (Figure 12b). It is observed that at the particular frequencies magnitude decreases as the distance $d$ value increases. Such effect is visible around 200–270 Hz for six distance values (from 35 mm to 135 mm). For the two greatest distances, these noise frequencies are not emitted as strongly. Above 375 Hz, magnitude decreases the most if the distance is 115 mm or 135 mm, in many narrow frequency subranges. These two distances correspond to the similar noise frequencies in Table 6.

Figure 13b presents the amplitude functions of the frequency functions of the impulse response estimates for the primary paths between the primary noise source and the top error microphone, at all examined distances. The top error microphone is the one located above the casing top panel's centre at the distance of 500 mm (Figure 12b). An expected phenomenon of magnitude decrease in case of increasing distance is observed around 290–360 Hz and around 200 Hz. However, there exist many frequencies, at which such effect is not observed. For instance, between 225 Hz and 275 Hz, magnitude is the lowest at the distances of 75 mm and 95 mm. Magnitude increases there along with an increase of most of the distance values. Effects as observed in Figure 13a are not visible.

It has to be emphasized that the panels of the lightweight device casing are vibrationally coupled due to the fact they are directly coupled with each other. Hence, back casing panel is coupled with the front one, and the effects observed for

the front panel may be referred to the back one. This is also true for the left and right casing panels. Figure 13c presents the amplitude functions of the frequency functions of the impulse response estimates for the primary paths between the primary noise source and the left error microphone for all examined distances. The left error microphone is the one located at the distance of 500 mm from the casing left panel's centre (Figure 12b). Above 375 Hz, magnitude is the lowest at many frequencies for the distance equal to 135 mm which corresponds to the similar noise frequencies in Table 6. Around 125–225 Hz and 250–275 Hz, magnitude decreases if the distance increases. There is a significant peak of magnitude decrease around 240 Hz for the shortest distance 35 mm. Around 330 Hz, magnitude increases along with the distance between the casing and the wall, which means that this noise frequency is emitted more strongly if the distance between the casing and the wall is greater.

Figure 13d presents the amplitude functions of the frequency functions of the impulse response estimates for the primary paths between the primary noise source and the right error microphone for all examined distances. The right error microphone is the one located at the distance of 500 mm from the casing right panel's centre (Figure 12b). Although left and right casing panels are vibrationally coupled, Figures 13c and 13d slightly differ from each other. For instance, a peak is observed at 240 Hz in Fig. 13c, where the magnitude is the lowest for distance equal to 35 mm. In Fig. 13d, the mentioned peak is replaced with a frequency range from around 215 Hz to 250 Hz. Also, at 250–275 Hz, the observed effect is in contrary to the one noticed in Fig. 13c — the magnitudes are lower for the short distances. Generally, both Figures are similar, and the slight differences may be related to slight asymmetry of error sensors locations, in relation to the wall.

Comparing Figs. 13a–13d, one common observation may be made that at the frequencies up to 150 Hz the magnitude levels are greater than above this band. Such behaviour is similar to that of subwoofers which reproduce the low frequencies of sound.

### 3.2.3. Secondary paths analysis

The research described in the following Chapter was also published in [89], and the following analysis applies to the same experiments, but presents also a novel and

extended description of the results. Secondary path is an acoustic path between input signal to one of the actuators (exciters), and the signal acquired by one of the error microphones. The amplitude functions of the frequency functions of the impulse response estimates for the secondary paths selected for further analysis are presented in Figs. 14a–15b.

The frequency range from 40 Hz to 500 Hz is considered, as the active control is employed, and its high efficiency is observed in the low noise frequency band. The actuators start to transmit vibration above 40 Hz, hence data obtained at 0–40 Hz are not taken into account in the analysis. Y axis range is set from −60 to −10 dB to maintain consistency of the results' presentation.

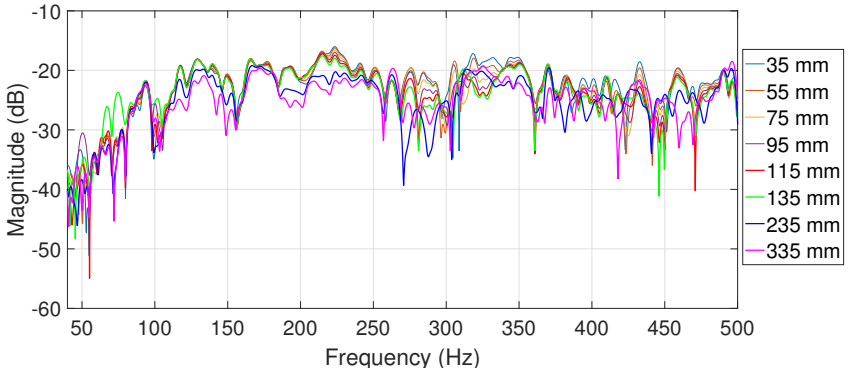


(a)

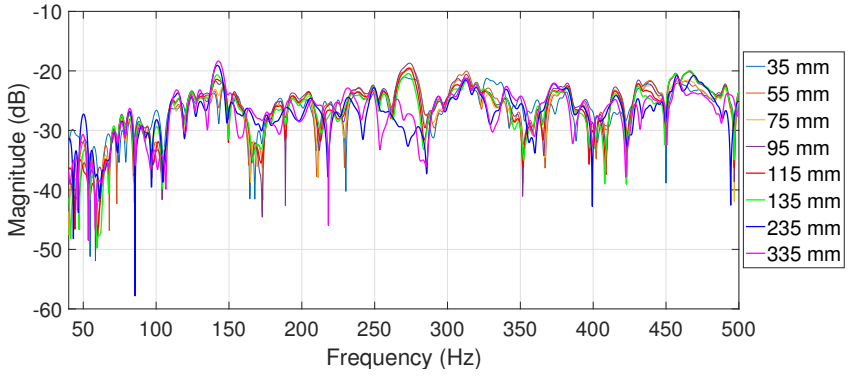


(b)

Figure 14: The amplitude functions of the frequency functions of the impulse response estimates for the secondary paths between actuator (a) no. 2, (b) no. 0 mounted on the back casing panel and the error microphone corresponding to the (a) top, (b) front casing panel, at all examined distances between the casing and the wall.

As half of the distances cover the low frequency range from Table 6, curves corresponding to them are emphasized on the graphs by means of wider lines and brighter colors. These distances are referred to below as Group 1 (115 mm, 135 mm, 235 mm, 335 mm) [89]. The second group of distances is referred to below as Group 2 (35 mm, 55 mm, 75 mm, 95 mm) [89].

Figure 14a shows the amplitude functions of the frequency functions of the impulse response estimates for the secondary paths between actuator no. 2 mounted on the back casing panel and the error microphone corresponding to the top casing panel, at all examined distances between the casing and the wall. There is a significant increase of magnitude (around 7 dB) at the frequency 75 Hz in case of the distance equal to 135 mm, in comparison to the curves obtained for other distance values. Two peaks of magnitude decrease are observed at around 270 Hz and 285 Hz for the distance equal to 235 mm, which is not the greatest one, but corresponds to these frequencies (Table 6). At many frequencies, magnitude is greater for shorter distances. It is observed for instance at 175–250 Hz and around 350 Hz.

Figure 14b shows the amplitude functions of the frequency functions of the impulse response estimates for the secondary paths between actuator no. 0 mounted on the back casing panel and the error microphone corresponding to the front casing panel, at all examined distances between the casing and the wall. As the front error microphone is the one most distant from the wall, the magnitudes of the amplitude responses of the secondary paths are lower than in Figure 14a. Magnitudes are higher for the two greatest distances at the frequencies around 160–175 Hz. Three peaks of magnitude decrease are observed for distances equal to 35 mm and 95 mm. Similar effect as in Figure 14a is observed at around 260–280 Hz for a curve corresponding to distance value equal to 235 mm.

Figure 15a presents the amplitude functions of the frequency functions of the impulse response estimates for the secondary paths between actuator no. 3 mounted on the back casing panel and the error microphone corresponding to the left casing panel for all examined distances between the casing and the wall. The magnitudes of all curves are significantly increased in comparison to Figures 14a–14b. This may be explained by the location of the left microphone, which may be more vulnerable to sound reflections from the wall than the top and front ones. The magnitudes for

most of the distance values increase above 365 Hz. At many frequencies, magnitude is higher if the distance is shorter. There are only several frequencies, at which magnitude decreases significantly for a particular distance. Such cases are observed at 305 Hz for 135 mm, as well as at 240 Hz and 420 Hz for 235 mm.

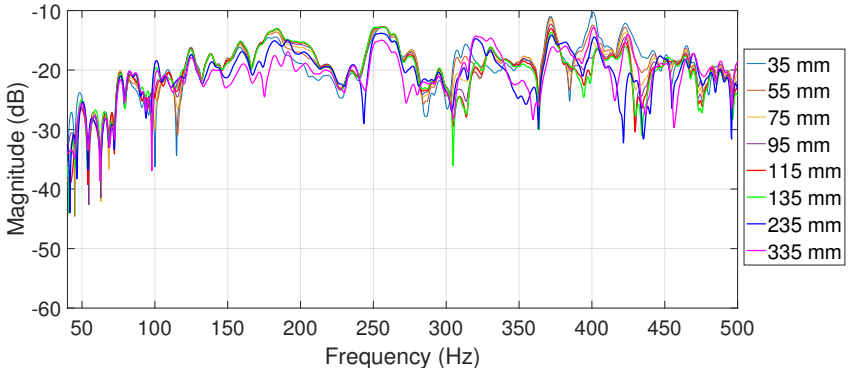


(a)

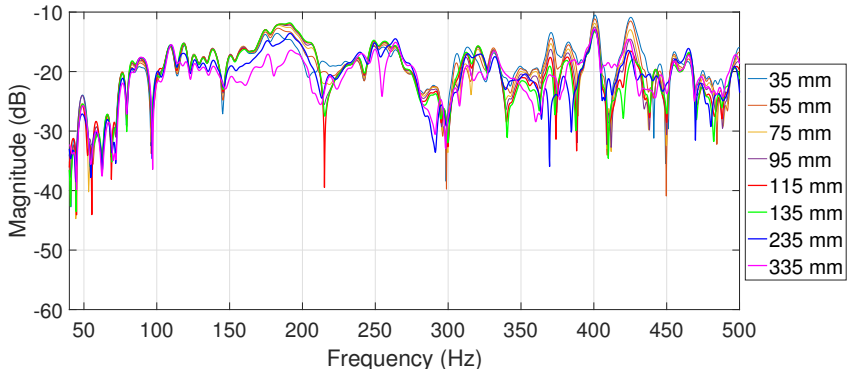


(b)

Figure 15: (a) The amplitude functions of the frequency functions of the impulse response estimates for the secondary paths between actuator no. 3 mounted on the back casing panel and the error microphone corresponding to the (a) left, (b) right casing panel, at all examined distances between the casing and the wall.

Figure 15b presents the amplitude functions of the frequency functions of the impulse response estimates for the secondary paths between actuator no. 3 mounted on the back casing panel and the error microphone corresponding to the right casing panel, at all examined distances between the casing and the wall. As in Figure 15a, the magnitude levels are higher than in Figures 14a–14b. This may be explained by the right microphone's placement, analogous to that of the left one. Levels and shapes of magnitude curves are generally similar to those presented in Figure 15a.

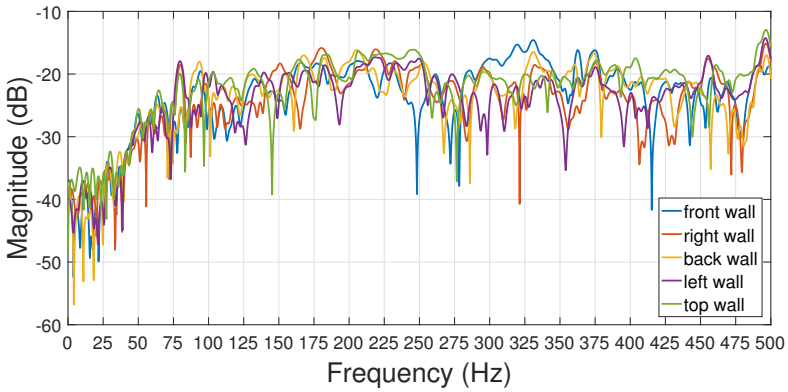


Figure 16: The amplitude functions of the frequency functions of the impulse response estimates for the secondary paths between actuator no. 1 mounted on each casing panel and the error microphone corresponding to the top casing panel, at the distance equal to 235 mm between the back casing panel and the wall.

However, magnitude decreases significantly at different frequencies and for different distance values. For instance, at 215 Hz it is observed for 115 mm, and at around 300 Hz for 75 mm and 95 mm.

A different kind of graph is presented in Figure 16, where comparison of the amplitude functions of the frequency functions of the impulse response estimates for the secondary paths between actuator no. 1 on each of the five casing panels and the error microphone corresponding to the top casing panel is shown, at the distance between the casing back panel and the wall equal to 235 mm. The frequency corresponding to this value of distance $d$ equals 243.4 Hz (Table 6).

Curves are compared with the assumption that exactly one actuator on each casing panel is selected, and the distance value is constant. Presented graph allows to compare the actuators' operation at different frequencies on different panels. The graph confirms that the actuators start to operate above 40 Hz. Around 240–250 Hz, which is a range including a frequency corresponding to the distance $d = 235$ mm (Table 6), an effect of magnitude decrease is observed for the actuator mounted on the front panel, which is vibrationally coupled with the back panel. Then, the magnitude increases and becomes the highest at above 300 Hz, where many peaks of magnitude decrease are observed for the actuators mounted on the left and right panels.

## 3.3. Lightweight device casing placed in a corner

The research described in the following Chapter was also published in [36], and the following analysis applies to the same experiments, but presents also a novel and extended description of the results. In the following Chapter, the experiments with the lightweight device casing placed in a corner are described. The Active Structural Acoustic Control approach is employed to achieve a global noise reduction in an enclosure [36]. Such approach requires the use of actuators instead of the loudspeakers as the secondary sources, which means that vibrations of the casing panels are actively controlled. This results in reduced noise emission to the environment.

As described in Chapter 1.2.2, ASAC has some advantages over classical Active Noise Control method [35, 114]. In the classical ANC, only the local zones of quiet can be achieved, and, as a consequence, the noise is reinforced elsewhere, whereas ASAC approach provides a global noise reduction in an enclosure. In the previous research, other authors confirmed efficiency of ASAC approach and reported the achievements in their publications, e.g. [91, 115, 116].

Prior to the research described in this dissertation, the lightweight device casing was placed in the laboratory enclosure whose walls were covered with pyramid acoustic foam panels. None of the casing walls interacted with reflective surfaces. In the research described below, the casing was placed in a corner composed of two reflective walls. Such placement of the casing is intentional to provide a facilitated operation of an active control system [36]. The space between the casing's back and right panels and the corner is small, and thus such setup may induce strong resonances in the mentioned space. This in turn will influence primary and secondary paths and the overall active control performance. Proposed approach refers to the realistic (domestic and industrial) setups with the noise generating devices located close to the reflective surfaces. Conducted research indicates the advantages that may be taken from the intentional sound reflections. As it is shown below, proposed setup composed of the lightweight device casing, error microphones and the corner, leads to a global noise reduction in a wide frequency band. To provide a complete analysis, primary and secondary paths are also analyzed. Hence, a thorough study of active control performance is presented.

### 3.3.1. Filtered-x Least Mean Squares algorithm

Active methods to reduce noise and/or vibration leverage algorithms for efficient control of the actuators, based on the signals acquired by the error sensors. One of the most popular algorithms used in the active control systems is Filtered-x Least Mean Squares (FxLMS) [117, 118]. This algorithm is popular because of design robustness, easy implementation and low computational complexity [119]. Figure 17 presents a basic scheme of FxLMS algorithm for a single-channel control system.

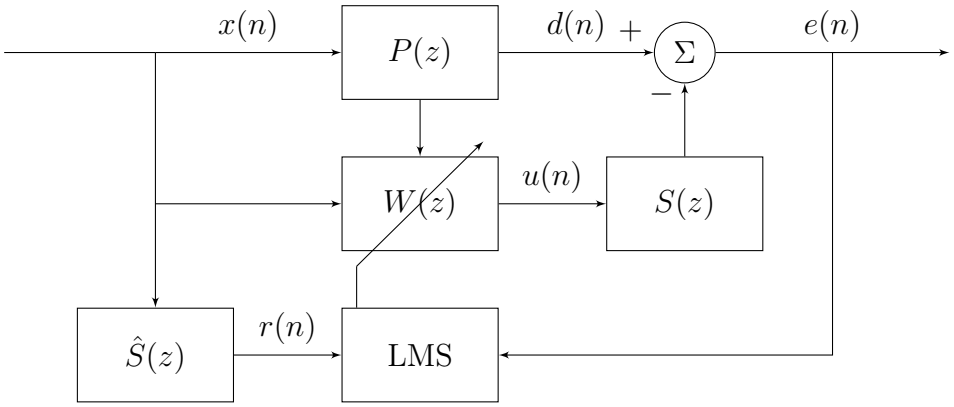


Figure 17: Scheme of FxLMS algorithm [33].

In Figure 17, $P(z)$ is the primary path, $S(z)$ is the secondary path, $\hat{S}(z)$ is the secondary path's model and $W(z)$ means a control filter, adapted with the use of LMS (Least Mean Squares) algorithm. As the algorithm's name says, a reference signal $x(n)$ is passed through $\hat{S}(z)$ (the secondary path's model) to produce an output $r(n)$ - a filtered reference signal [33]. Signal $x(n)$, if passed through the primary path $P(z)$, gives an output signal $d(n)$ - the primary disturbance. An output of the adaptive filter $W(z)$ is marked as $u(n)$. It is passed through $S(z)$ to obtain a negative input to the summation node. Once both inputs are summed, a residual error signal $e(n)$ is obtained. The goal of the control system is to minimize the sum of squares of $e(n)$ over the length of $W(z)$.

FxLMS algorithm has some drawbacks, such as a contradiction between convergence rate and steady-state performance due to a fixed step size [120]. It means that if step size is larger, convergence rate will be faster, but steady-error also will increase, and in the opposite case steady-state error will be reduced but convergence will decrease [121]. This can be overcome by introducing a variable step size, whose

initial value is set to a larger value for faster convergence, and then step size is decreased to reduce steady-state error [120].

If there are more inputs and outputs in a control system, MIMO (Multiple-Input Multiple-Output) FxLMS algorithm [122, 91, 123] has to be employed, as such a complex control system has a high computational demand. As in the control system described in this dissertation, the plant is controlled by multiple inputs and returns multiple outputs, such approach is employed in the described experiments. The control system was implemented prior to this research [124], hence it is not included as part of the dissertation in details.

### 3.3.2. Laboratory setup

In the experiments performed using the lightweight device casing [86] (which is described in Chapter 2.1) placed in a corner, a noise-generating device (a loudspeaker) is placed inside the casing. Loudspeaker acts as a primary noise source and is located on a sound-insulated basis. The loudspeaker was selected as a sound source instead of any particular industrial device, because it allows to better evaluate the active control system performance [36].

Figure 18 presents the experimental setup. It is composed of the lightweight device casing, the microphones, and the corner built of reflective walls. Microphones act as the sensors: one reference microphone is placed inside the casing to acquire the primary noise, five error microphones are located around the casing, and four monitoring microphones are located arbitrarily in the laboratory enclosure distant from the casing to acquire noise emitted globally. Room microphones are used to evaluate active control performance only, and are not the inputs to the control system. Placement of the room microphones corresponds to possible locations of the end users [125].

Vibrations of the casing panels are controlled by means of NXT EX-1 exciters, which are described in Chapter 2.3.1. The exciters are mounted to the casing panels on their inner surface. Five actuators are mounted to the top panel, and four actuators are mounted to each of the following panels: front, back, left and right one. Number and placement of the actuators was specified by Wrona and Pawełczyk prior to this research in the process of optimization as described in [86].

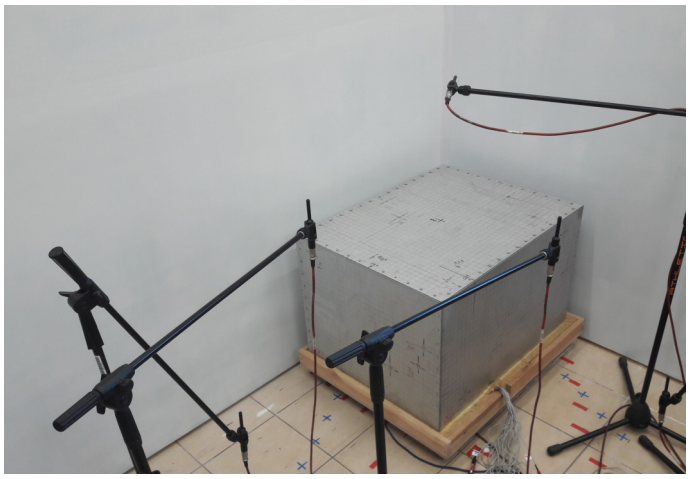

Figure 18: Lightweight device casing placed in a corner: the experimental setup.

The lightweight device casing is placed in a corner with its back and right panels. Several distances between the casing and the corner are examined, according to the rule explained in Chapter 2.1. Active methods are considered as the most efficient in the low frequency band, conventionally understood as up to 500 Hz [126]. In this range, most of the common domestic and industrial appliances have their dominating frequencies. As such frequency range (0–500 Hz) is of interest, distance $d$ values were selected according to this rule. Distance varies from 0.1 m to 0.8 m with step size set to 0.1 m. Table 7 presents a comparison of selected distance values and the corresponding frequencies as in Eq. (5), with the assumption that speed of sound in air $c$ at 20 °C is equal to 343.21 m/s. The values of distance in Table 7 stand for the distance between back and right casing panels, and the corner walls corresponding to them.

Table 7: Distances versus frequencies.

| Distance $d$ [m] | Frequency $f$ [Hz] |
|---|---|
| 0.1 | 572 |
| 0.2 | 286 |
| 0.3 | 190.7 |
| 0.4 | 143 |
| 0.5 | 114.4 |
| 0.6 | 95.3 |
| 0.7 | 81.7 |
| 0.8 | 71.5 |

Same as in Chapter 3.2, it is assumed that the corner walls are rigid and reflective, like in the industrial and domestic enclosures which may be encountered in reality. The walls were built in the same way as in Chapter 3.2, and the material was based on Table 5. As a result, the corner composed of dense and smooth walls was built.

### 3.3.3. Arrangement of the error microphones around the device casing

An important aspect of the experimental setup is an arrangement of error microphones, as it influences active control performance. Different ideas to arrange the error microphones were developed. Initial concept assumed that the error microphones would be placed on the sphere surrounding device casing [127]. Generally, spherical microphone arrays are employed in a wide range of applications [128], and spherical design is a complex and wide field of study itself [129, 130]. Spatial sampling on a sphere is an important aspect and requires the fulfillment of theoretical assumptions [127]. In this dissertation, device casing is placed in a reflective corner, hence the sphere surrounding the casing is reduced to one-eighth of a sphere. Such setup would require additional modeling and simulation. Hence, as the dissertation is focused in details on different topics, the initial concept was simplified, and the design of microphones' arrangement was based partially on experimental measurements with arbitrarily adjusted setups to evaluate efficiency of considered setups in terms of active control performance. The sphere was visualized by means of FreeCAD (Figure 19a). The casing had to be fully enclosed within the sphere. It was assumed that positions of the left, front and top error microphones would be the same as in the previous experiments with the device casing placed at a wall. Hence, each of these microphones was placed at the distance of 500 mm from the corresponding panel's centre. The sphere boundaries had to fit these microphones and include placements for two remaining microphones: both right and back one. The back microphone had to be equally distant from left, top and right ones, and the right microphone had to be equally distant from back, top and front ones. The sphere radius was 823 mm. Microphones' arrangement was set by means of GeoGebra 3D Calculator. The active control experiment was performed for such arrangement of the error microphones. The results were not satisfactory regarding the active control performance (Figure 20).

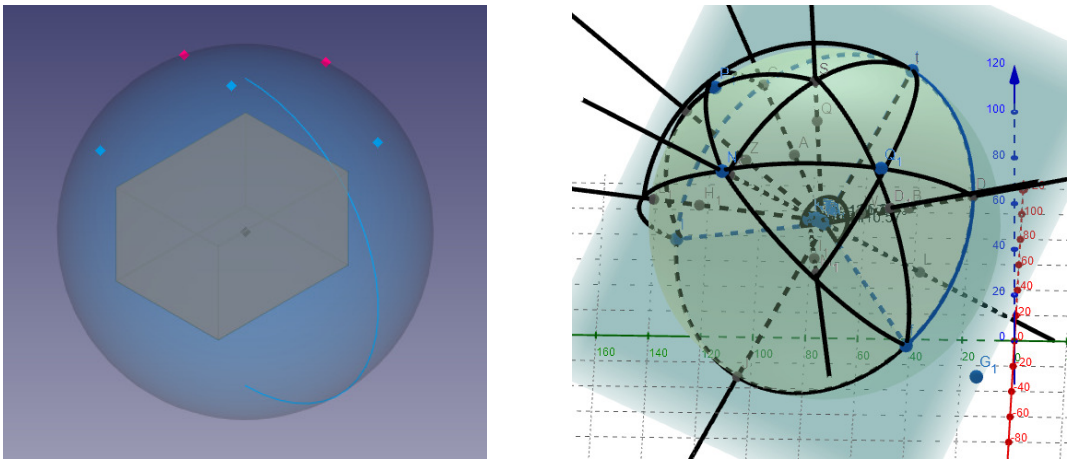

(a) (b)

Figure 19: Preliminary approach to error microphones' arrangement. (a) FreeCAD. (b) GeoGebra 3D Calculator.

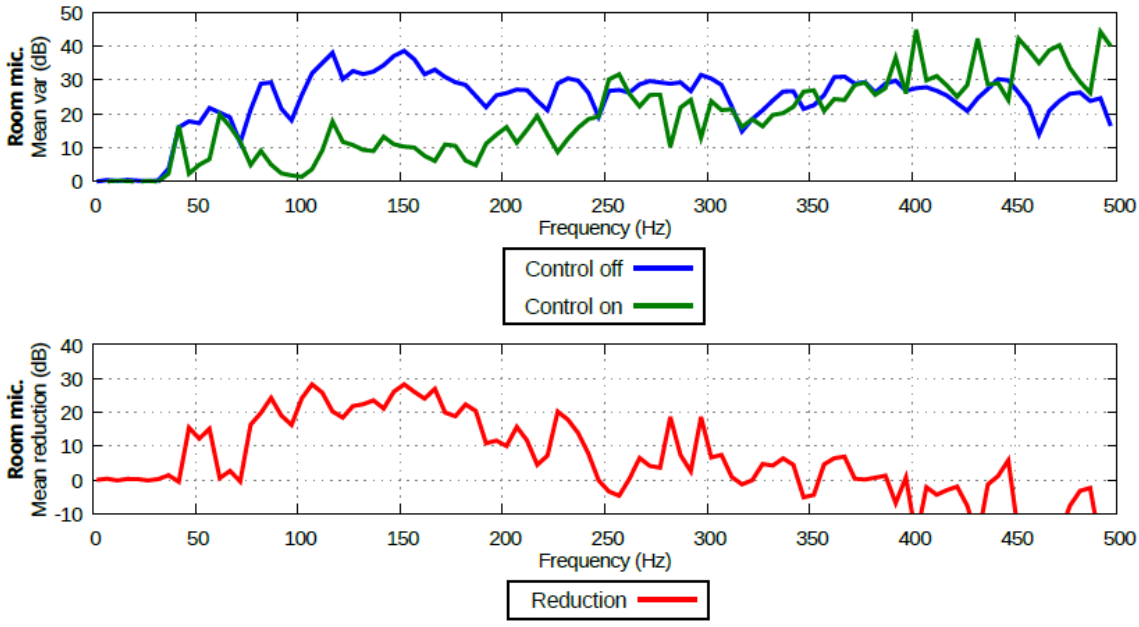


Figure 20: Active control performance for a preliminary setup.

Further increase of the sphere radius did not improve the preliminary results. After preliminary experiments, the concept was slightly changed. The new approach was inspired by the spherical design, but was not strictly relying on the assumptions. Finally, based on the outcome from preliminary experiments, two setups were selected, referred to below as Setup 1 and Setup 2. These setups were later compared based on their influence on active control performance, what is described in details in Chapter 3.3.6.

In both setups, left, front and top error microphones are located at the distance of 500 mm each from the corresponding panel's centre. The only difference between these setups is the arrangement of back and right error microphones [36]. Both setups are shown in Figure 21. In Setup 1, back and right error microphones are placed between the casing and the corner (Figure 21a). Back error microphone is located between the corresponding corner wall and the back casing panel's centre, equally distant to both surfaces. Right error microphone is located between the corresponding corner wall and the right casing panel's centre, equally distant to both surfaces.

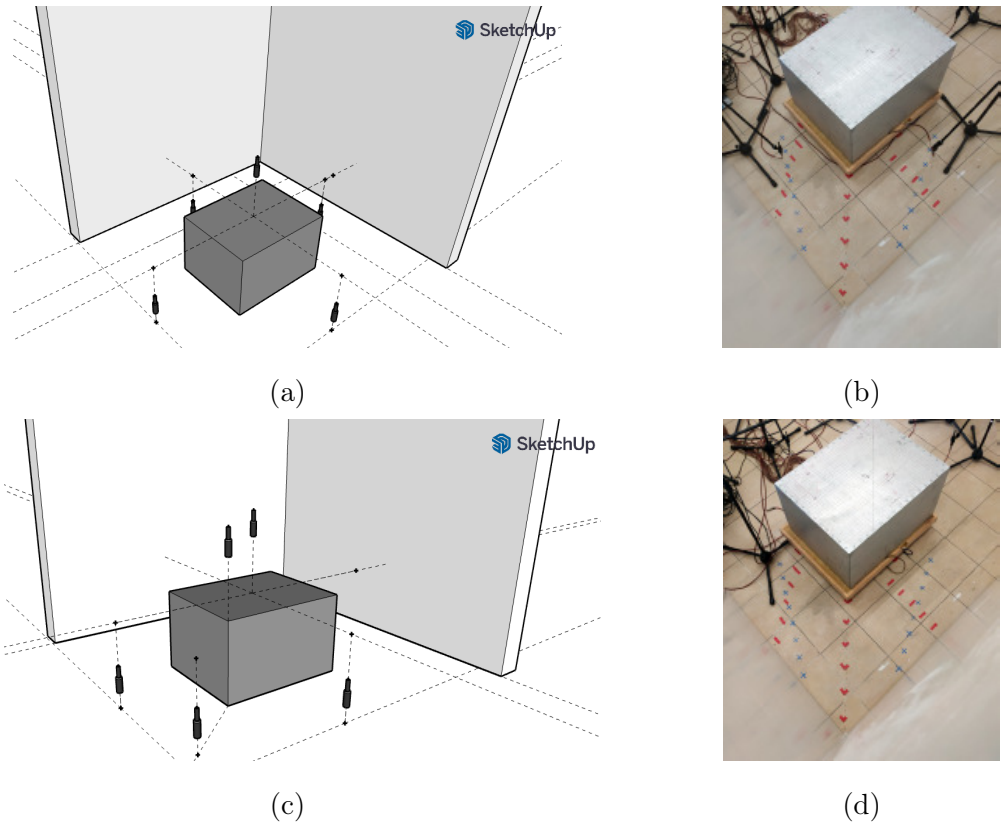


Figure 21: Arrangement of the error microphones. (a), (b) Setup 1. (c), (d) Setup 2.

Figure 21b presents Setup 2, where back and right error microphones are placed in the arbitrarily selected locations among other error microphones (left, front and top ones). None of the error microphones is placed in the space between the casing and the corner. Back error microphone in Setup 2 is located next to the top error microphone, at the distance of 500 mm from the lightweight device casing's corresponding corner. Right error microphone in Setup 2 is located among left and front

error microphones, at the distance of 500 mm from the lightweight device casing's corresponding edge. While all of the error microphones have to be moved when the distance between the casing and the corner changes, the monitoring (room) microphones remain in their locations.

### 3.3.4. Primary paths analysis

The research described in the following Chapter was also published in [36], and the following analysis applies to the same experiments, but presents also a novel and extended description of the results. Knowledge of primary and secondary paths' models supports the development of control system [91]. The amplitude functions of the frequency functions of the impulse response estimates for the primary paths are presented as the magnitude versus frequency graphs. Curves are plotted for all selected distances between the casing and the corner, i.e. 0.1–0.8 m [36]. Figure 22 presents the amplitude functions of the frequency functions of the impulse response estimates for the primary paths obtained for right error microphone, in both setups of error microphones [36]. As the location of right error microphone is different in both examined setups, amplitude responses obtained in Setup 1 (Figure 22a) and in Setup 2 (Figure 22b) also differ from each other. Maximum magnitude levels are higher in Setup 1 than in Setup 2. At most of the frequencies in Setup 1, magnitude increases when the distance between the casing and the corner decreases. This is not observed in Setup 2 (Figure 22b), where right error microphone is moved from the space between the casing and the corner to the space among other error microphones. As the right error microphone is located in the narrow space between the casing and the corner, it becomes vulnerable to the additional resonances in the gap where it is located, especially for the shortest distance between the casing and the corner. In such a case, it does not acquire a signal representative for the noise emitted by the lightweight device casing, and the signal is affected by the resonances occurring in the gap [36]. It is noted for the four shortest distances in Setup 1, i.e. 0.1–0.4 m. Such measurements acquired by right error microphone, influenced by the additional resonances, may negatively impact the active control performance.

Figure 23 presents the amplitude functions of the frequency functions of the impulse response estimates for the primary paths obtained for back error microphone

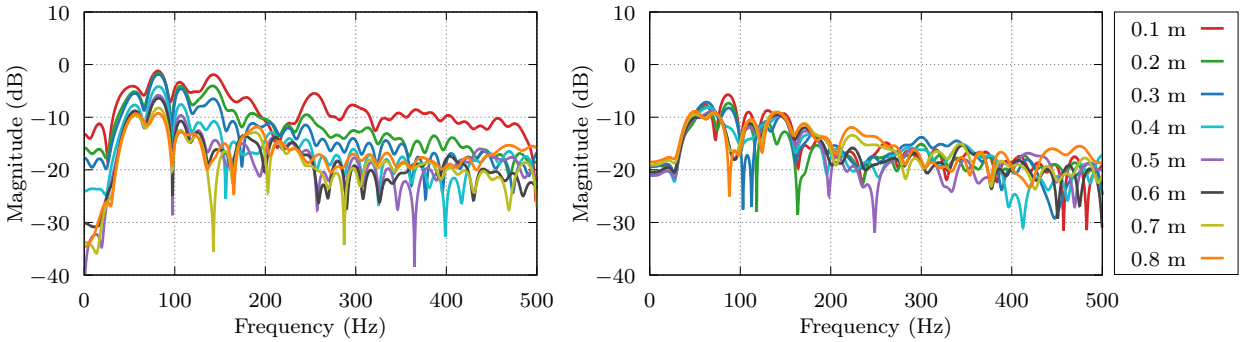


(a) Setup 1. (b) Setup 2.

Figure 22: The amplitude functions of the frequency functions of the impulse response estimates for the primary paths obtained for right error microphone in both setups of error microphones [36].

in both setups — Setup 1 (Figure 23a) and Setup 2 (Figure 23b) of error microphones [36]. Similar observations as in the case of Fig. 22 can be made. However, the magnitude levels in both setups are greater in comparison to Figure 22. This may be explained by the different positions of right and back error microphones, as the casing is not a cube, and the dimensions of back and right wall are different. Hence, the distance between right microphone and the corner walls' junction, and the distance between back error microphone and the corner walls' junction, are different.

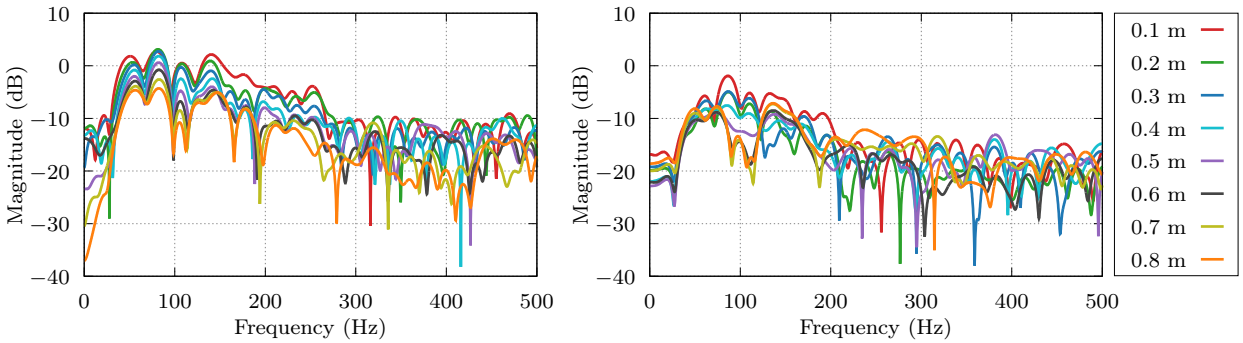


(a) Setup 1. (b) Setup 2.

Figure 23: The amplitude functions of the frequency functions of the impulse response estimates for the primary paths obtained for back microphone in both setups of error microphones [36].

Figure 24 presents the amplitude functions of the frequency functions of the impulse response estimates for the primary paths obtained for top error microphone in

both setups — Setup 1 (Figure 24a) and Setup 2 (Figure 24b) of error microphones [36]. Position of the top error microphone is the same in both setups, i.e. its relation to the corresponding lightweight device casing corner is the same. Hence, the amplitude responses look similar in both setups. The magnitude levels are lower in comparison to Figures 22–23. This indicates the obtained results are consistent. Below 125 Hz, an effect of magnitude increase for decreasing distance between the casing and the corner is noticeable for both setups. This means that when the casing is moved closer to the corner, then low frequencies of noise are emitted more strongly. Above 125 Hz, this trend cannot be observed [36].

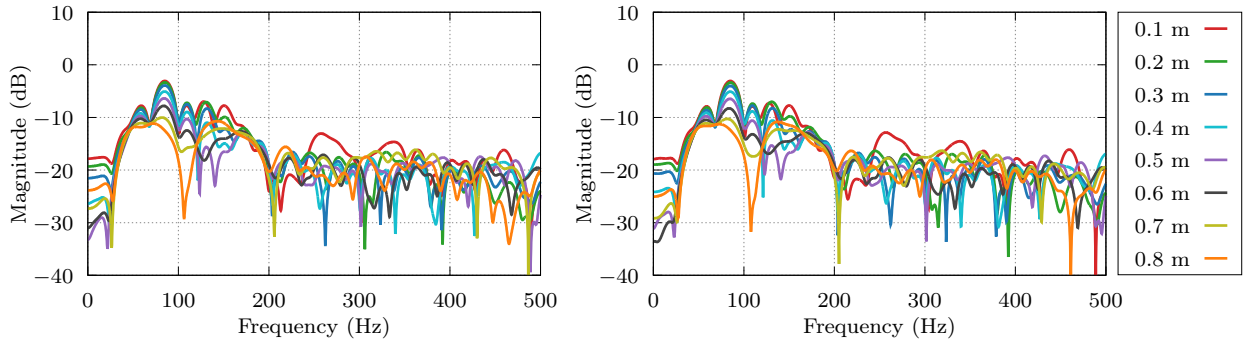


(a) Setup 1. (b) Setup 2.

Figure 24: The amplitude functions of the frequency functions of the impulse response estimates for the primary paths obtained for top error microphone in both setups of error microphones [36].

Figure 25 presents the amplitude functions of the frequency functions of the impulse response estimates for the primary paths obtained for one of the room microphones in both setups — Setup 1 (Figure 25a) and Setup 2 (Figure 25b) of error microphones [36]. Room microphone's location was not changed during the experiments. The general decrease of the magnitudes in both setups is observed if the room microphone is considered. It is an expected behaviour, as the room microphone is distant from the casing and from the reflective corner surfaces. The amplitude responses are similar in both setups, which indicates the consistency of the results [36]. Magnitudes are higher below 125 Hz, and the effect of magnitude increase for decreasing distance is noticeable. This indicates that low frequencies are strongly excited in the enclosure, if the casing is close to the corner, and such phenomenon is similar to that observed for subwoofers.

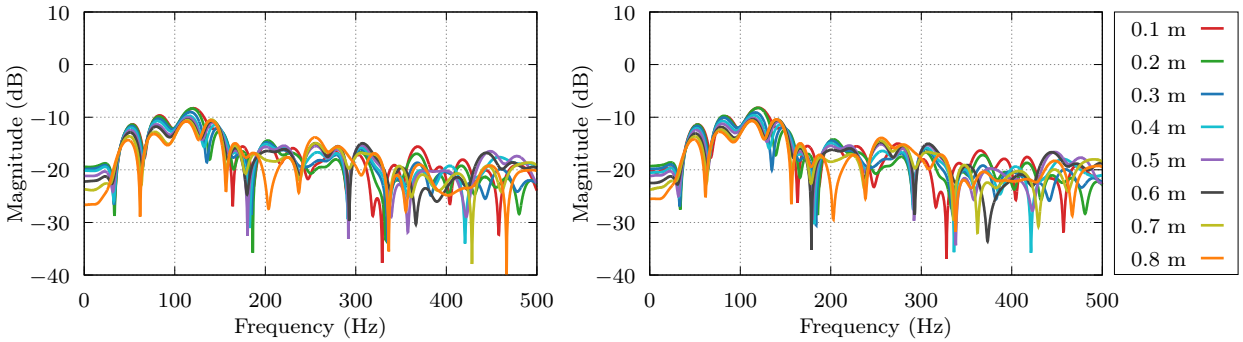


(a) Setup 1. (b) Setup 2.

Figure 25: The amplitude functions of the frequency functions of the impulse response estimates for the primary paths obtained for one of the room (monitoring) microphones in both setups of error microphones [36].

### 3.3.5. Secondary paths analysis

The research described in the following Chapter was also published in [36], and the following analysis applies to the same experiments, but presents also a novel and extended description of the results. In the following Chapter, selected amplitude responses of the secondary paths are shown. Figure 26 presents the amplitude functions of the frequency functions of the impulse response estimates for the secondary paths between five selected actuators (each one located on a different casing panel), and the right error microphone [36]. Plots for both setups of error microphones are included. The distance between the corner and the casing's back and right panels is 0.1 m per each of these panels (the smallest one considered). Magnitudes are in general higher for Setup 1, and such trend is observed for all of the selected actuators, even the ones mounted on the panels different than the right one. As expected, the magnitude obtained for the actuator mounted on the right panel is at most of the frequencies the highest one. It is noticeable especially below 300 Hz. In Setup 2, there are not significant differences between the magnitudes. As the right error microphone is moved from the narrow space between the casing and the corner to a location among the other error microphones, it does not acquire the resonances occurring in the gap [36].

Figure 27 presents the amplitude functions of the frequency functions of the impulse response estimates for the secondary paths between one of the actuators mounted on the right panel, and the right error microphone [36]. All distances are

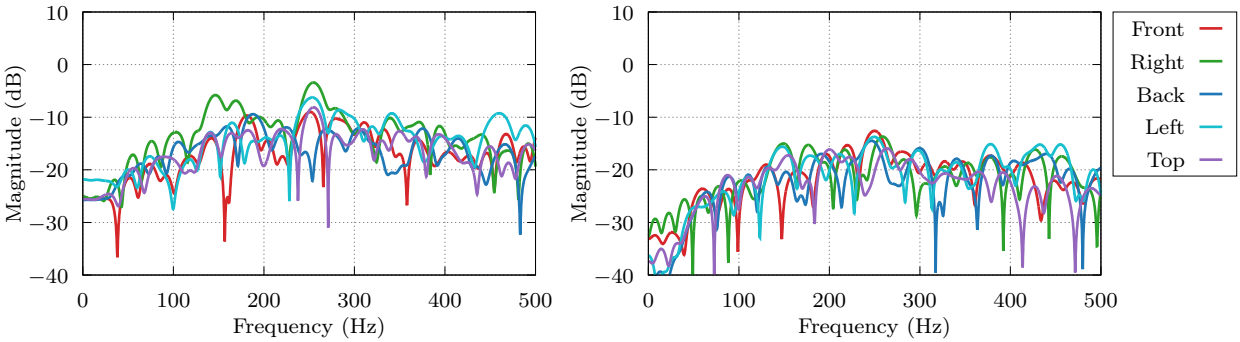


(a) Setup 1. (b) Setup 2.

Figure 26: The amplitude functions of the frequency functions of the impulse response estimates for the secondary paths between five actuators (each one located on a different casing panel), and the right error microphone. Distance is equal to 0.1 m [36].

taken into account. Magnitudes are higher for Setup 1 in comparison to Setup 2, but only for three smallest distance values, i.e. 0.1 m, 0.2 m and 0.3 m. As the distance increases, magnitudes decrease at most of the frequencies in the considered range [36].

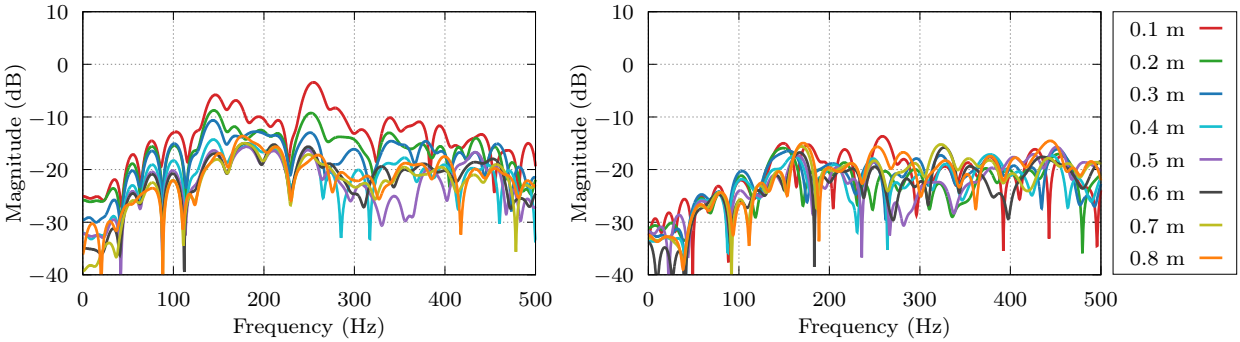


(a) Setup 1. (b) Setup 2.

Figure 27: The amplitude functions of the frequency functions of the impulse response estimates for the secondary paths between one actuator mounted on the right casing panel, and the right error microphone. All distance values are selected [36].

Figure 28 presents the amplitude functions of the frequency functions of the impulse response estimates for the secondary paths between one of the actuators mounted on the back panel, and the back error microphone [36]. All distance values are taken into account. In Setup 1, maximal magnitude levels are higher in comparison to Setup 2. At most of the frequencies, increasing distance implies decrease

of magnitude levels. The amplitude response obtained for distance value 0.1 m is characterized by a higher magnitude level than the other ones. In Setup 2, all magnitudes are similar, excluding the frequencies around 175–225 Hz, where the effect of increasing magnitude along with the decreasing distance is observed. This indicates that if the back error microphone is placed among other microphones, and not in the space between the casing and the corner, then a decrease of the distance may result in emission enhancement in the enclosure within a narrow frequency band only [36].

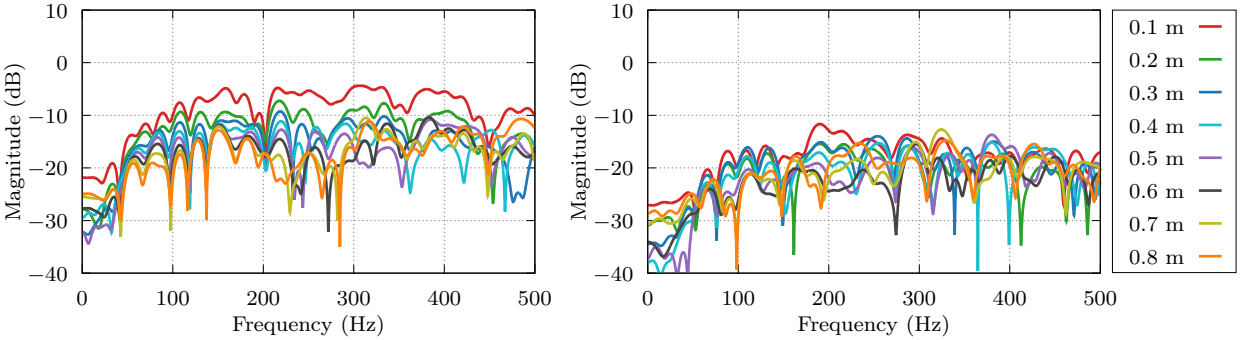


(a) Setup 1. (b) Setup 2.

Figure 28: The amplitude functions of the frequency functions of the impulse response estimates for the secondary paths between one actuator mounted on the back casing panel, and the back error microphone. All distance values are selected [36].

Figure 29 presents the amplitude functions of the frequency functions of the impulse response estimates for the secondary paths between one of the actuators mounted on the top panel, and the top error microphone [36]. All distance values are taken into account. Plots for both Setups of error microphones are similar, which indicates that changing the distance between the casing and the corner does not influence the signals acquired by the top microphone much. However, the emission is slightly enhanced for decreasing distance at the lower frequencies, up to 180 Hz [36].

Figures 30–31 present the amplitude functions of the frequency functions of the impulse response estimates for the secondary paths between selected actuators and room microphone, whose placement was not changed during the experiment to ensure a reliable representation of the work environment, where an exact position of the person, during exposure to noise, may not be changed [36]. Also, a global noise reduction should be observed in the enclosure regardless of user's location.

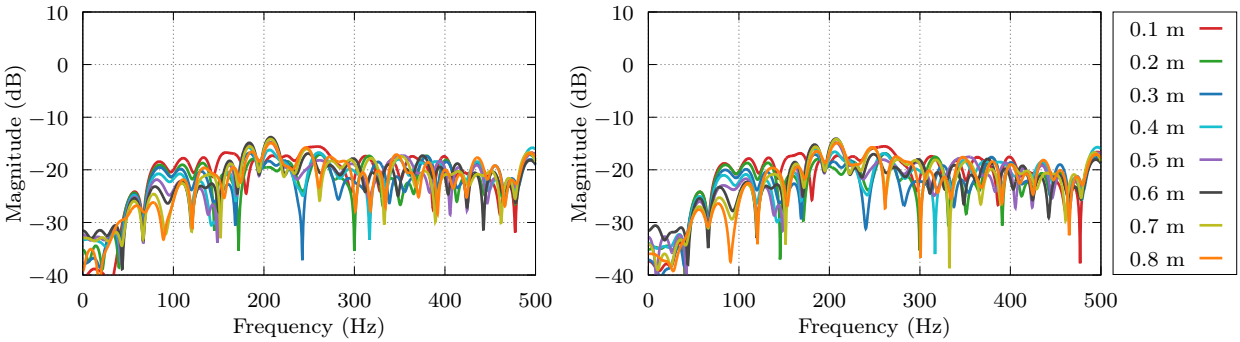


(a) Setup 1. (b) Setup 2.

Figure 29: The amplitude functions of the frequency functions of the impulse response estimates for the secondary paths between one actuator mounted on the top casing panel, and the top error microphone. All distance values are selected [36].

Figure 30 shows the amplitude responses obtained for an actuator mounted on the back casing panel, and Figure 31 presents the amplitude responses for selected actuator from the right casing panel. In both Setups, magnitude levels are low. There are not significant differences between the magnitudes obtained for varying distance values. In general, trends observed for the amplitude responses correspond to the observations made in Chapter 3.3.4. This indicates that the control algorithm's performance should not be negatively impacted, as both types of paths are balanced in the changing circumstances [36].

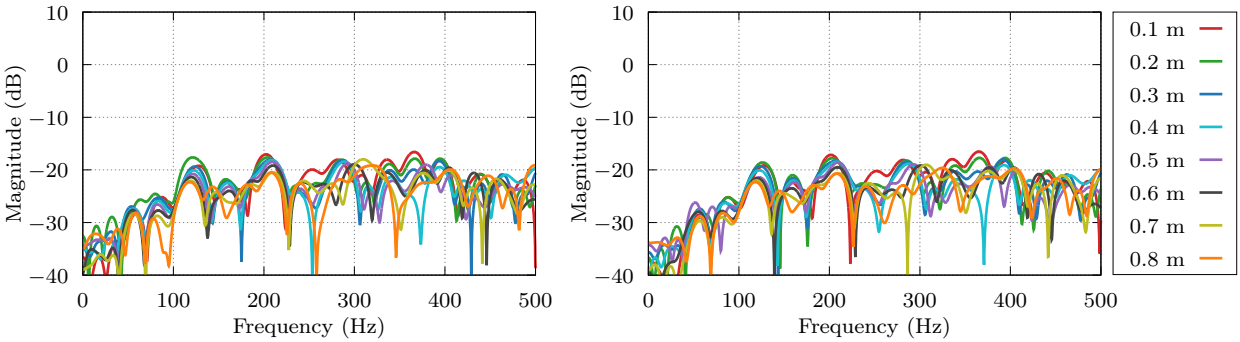


(a) Setup 1. (b) Setup 2.

Figure 30: The amplitude functions of the frequency functions of the impulse response estimates for the secondary paths between one actuator mounted on the back casing panel, and the room error microphone. All distance values are selected [36].

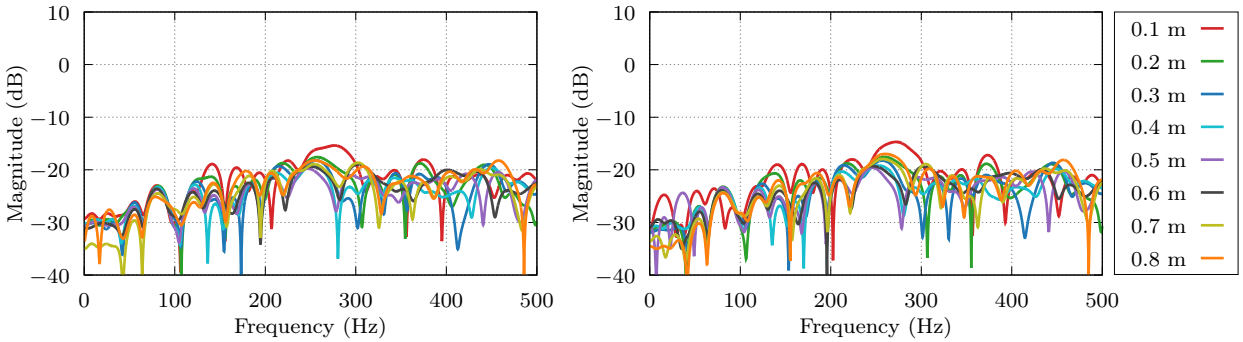


(a) Setup 1. (b) Setup 2.

Figure 31: The amplitude functions of the frequency functions of the impulse response estimates for the secondary paths between one actuator mounted on the right casing panel, and the room error microphone. All distance values are selected [36].

### 3.3.6. Active control system performance

The research described in the following Chapter was also published in [36], and the following analysis applies to the same experiments, but presents also a novel and extended description of the results. In this Chapter, an active control performance is investigated experimentally. As a noise source, a loudspeaker located inside the casing was used. To obtain the frequency characteristics, the loudspeaker was employed to generate primary tonal noise in range 1–350 Hz, with step = 5 Hz. A 1-minute-long experiment was performed for each of the considered frequencies. For the first 5 seconds of each measurement, the active control system was turned off, and the variance of signals acquired by the sensors was estimated as a reference. The active control system was then turned on, and once the algorithm converged, last 5 seconds of each measurement were used for estimation of the variance of signals acquired by the corresponding sensors [36]. Active control performance is evaluated as the global noise reduction level, based on the signals acquired by the room (monitoring) microphones. Both Setups (1 and 2) of error microphones were examined, as well as all distances $d$ between the casing and the corner as in Table 7.

Figures 32–33 present the frequency characteristics obtained during the active control experiments [36]. Fig. 32 shows the average variance of the room microphone signals versus frequency, at all examined distances. The results are plotted separately for each of the distance values (Table 7). Black lines represent the mean primary noise when control was off, in both Setups (1 and 2).

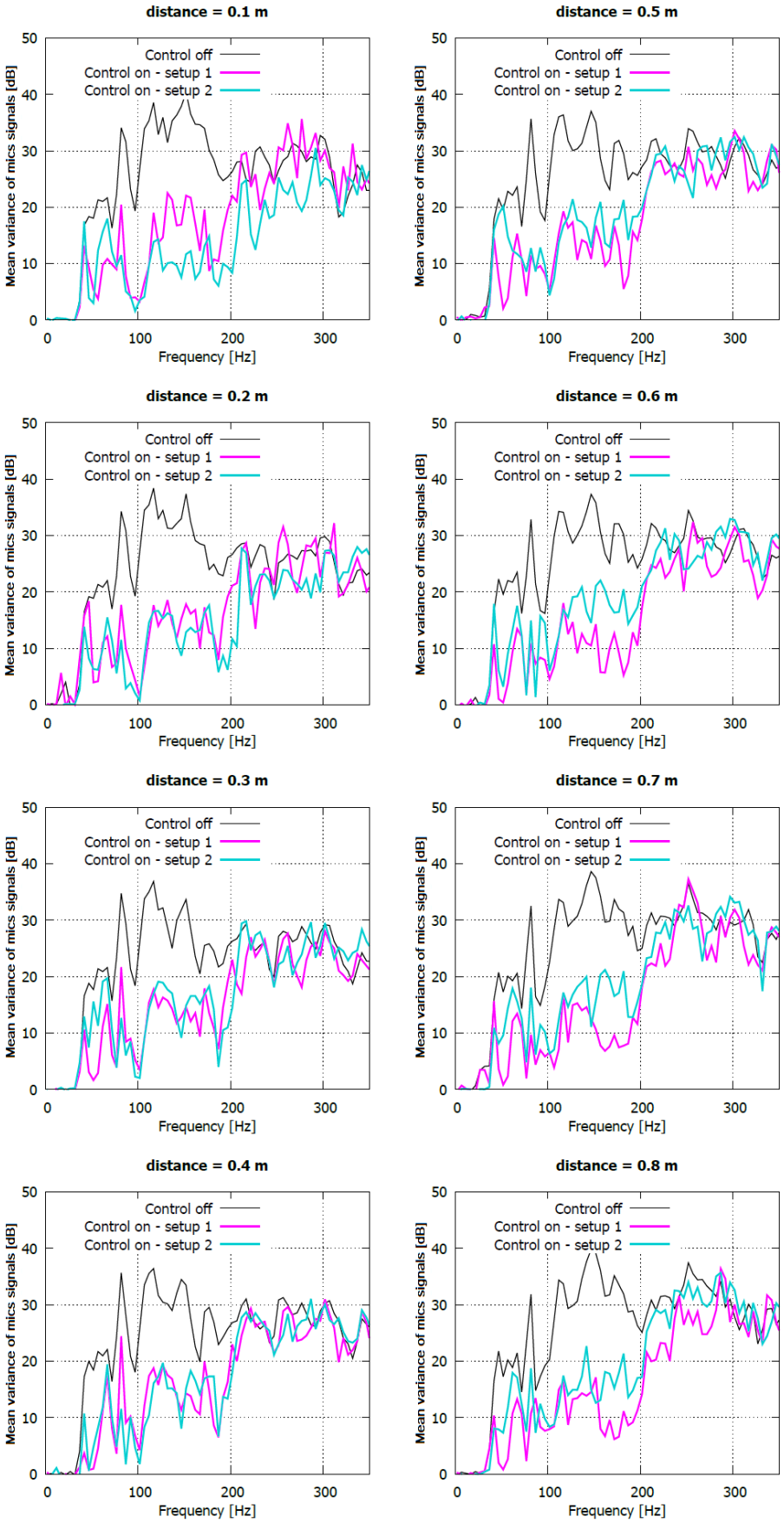


Figure 32: Active control performance for all distance $d$ values for both Setups (1 and 2). Y axis: mean variance of the room microphones' signals. Based on [36].

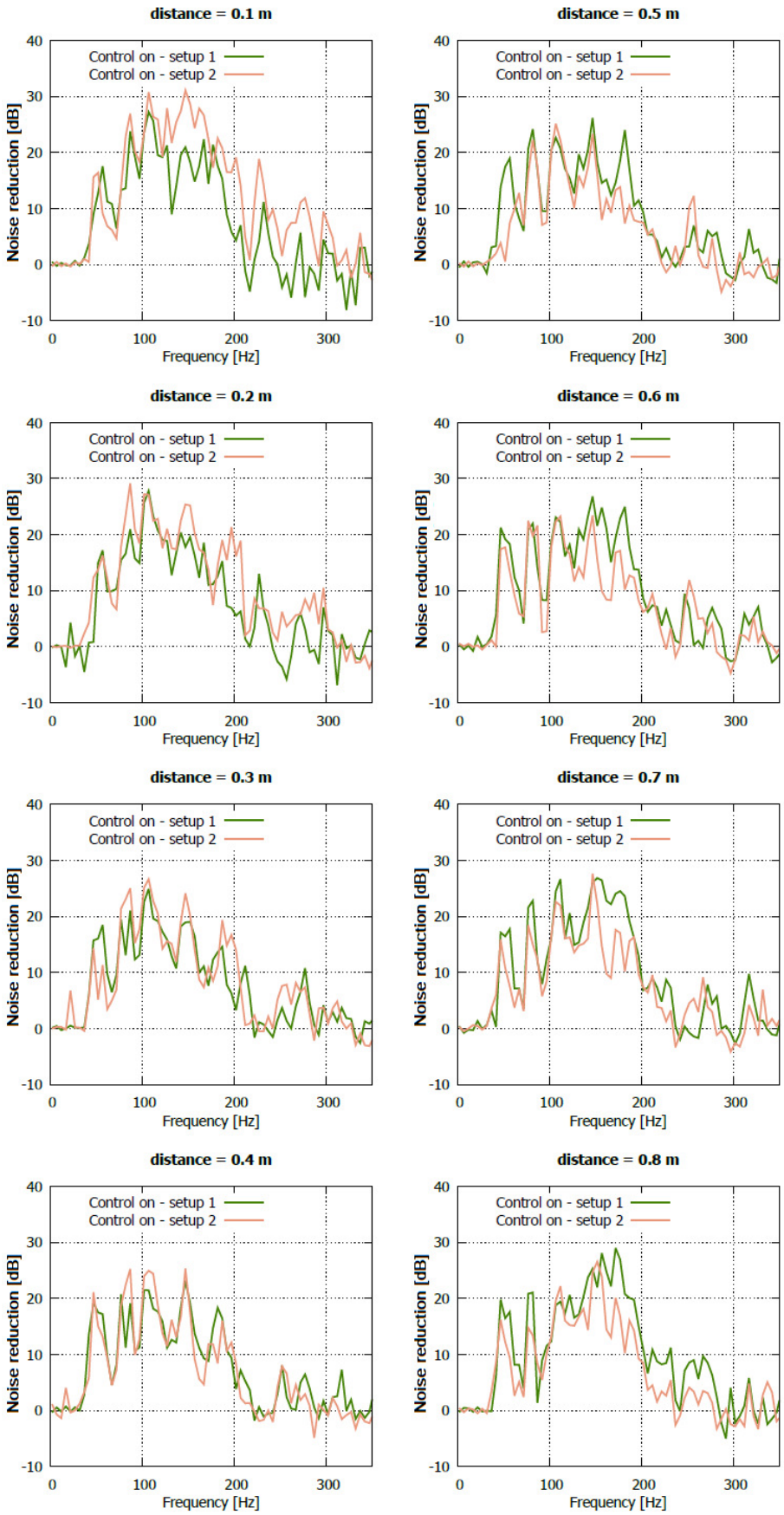


Figure 33: Active control performance for all distance $d$ values for both Setups (1 and 2). Y axis: mean noise reduction levels estimated based on the signals acquired by the room microphones. Based on [36].

Line in magenta color represents residual noise obtained when control was on and the error microphones' arrangement was Setup 1. Line in skyblue color represents residual noise obtained when control was on and the error microphones' arrangement was Setup 2. In Figure 33, Y axis refers to mean noise reduction levels estimated based on the signals acquired by the room microphones, calculated as a difference between noise levels when active control was turned off and on [36]. The results are plotted separately for each of the considered distances (Table 7).

Analysis of Figures 32–33 implies that the arrangement of error microphones affects the active control system's performance. For the distances between the casing and the corner equal to or greater than 0.5 m, Setup 1 is characterized by higher noise reduction levels than Setup 2. For smaller distance values (0.1–0.4 m), it is the opposite. Especially for the distance equal to 0.1 m, Setup 2 provides significantly better performance of the active control system. If the device casing is moved closer to the corner, it is more beneficial to move the error microphones from the narrow space between the casing and the corner to the other side of the casing. In this specific case, it should be done when the distance value decreases to 0.4 m [36].

At the distance 0.1 m, Setup 2 provides the best performance of an active control system, with up to 30 dB of a global mean noise reduction. Similar (but worse) results are achieved for the second setup (Setup 1) if the distance between the casing and the corner is set to 0.8 m. If the casing is placed close to the corner, the global noise reduction levels are higher and observed over a wider frequency range. Such observation indicates that the examined configuration performs well even though located near the reflective surfaces, and should at least provide results of the same quality compared to the configuration with the device casing located distant from the laboratory walls [36]. These results prove that introducing the interactions between the device casing and the rigid wall at least do not impact negatively the active control system's performance, and may even lead to its improvement. In the research conducted prior to this dissertation, in the laboratory enclosure without any reflective surfaces, maximal global noise reduction level exceeded 15 dB [91, 123]. The results presented in this dissertation are at least of similar quality. However, direct comparison of both configurations is unjustified, as the experimental setup evolved over time [36].

At the smallest distance $d = 0.1$ m between the casing and the corner, back and right error microphones (Chapter 3.3.3) impede the adaptation of the active control system if Setup 1 is selected, what is shown above 250 Hz in Fig. 34. Such behaviour of back and right microphones is not observed in Setup 2 at this particular distance $d$ value. Such observations do not apply to front, left and top microphones.

As Figure 35 shows, it is more beneficial to turn off back and right microphones and leave only three error sensors operating at the distance 0.1 m, than to use Setup 1 arrangement. Green color represents a third setup, when back and right microphones are disabled. For such setup, mean noise reduction levels are higher at most of the frequencies in the considered range than in Setup 1. However, the best performance is observed for Setup 2. Hence, if the device casing is placed close to the corner, operation of all error sensors should be examined, as some of them may impede the active control system operation [36].

As the configuration with the device casing placed in the corner was examined, another important aspect was the influence of back and right panels' actuators on the overall active control system performance. Two different experiments were performed: one with left and front panels' actuators disabled, and the other one with right and back panels' actuators disabled [36]. The distance value was $d = 0.1$ m. Setup 2 was selected as the error sensors did not impede the active control performance then. As stated in Chapter 3.2.3, back panel is vibrationally coupled to the front one, and left panel is vibrationally coupled to the right one [91]. Hence, it is expected that the results should be similar for both approaches. Figure 36 presents mean variances and mean noise reduction levels for the following scenarios: active control off, active control on (Setup 2), active control on but front and left panels' actuators disabled (Setup 2), active control on but back and right panels' actuators disabled (Setup 2). Results obtained when active control was on are similar for all three approaches, even though in two of them eight actuators were disabled. This confirms the important role of vibrational couplings between the casing's panels. The actuators excite the whole casing efficiently and it is equally beneficial to locate them at the panels near to the corner walls as at the opposite side [36]. However, at the low frequencies, it is visible that enabling all 21 actuators provides the best results because then they have enough power to control these frequencies.

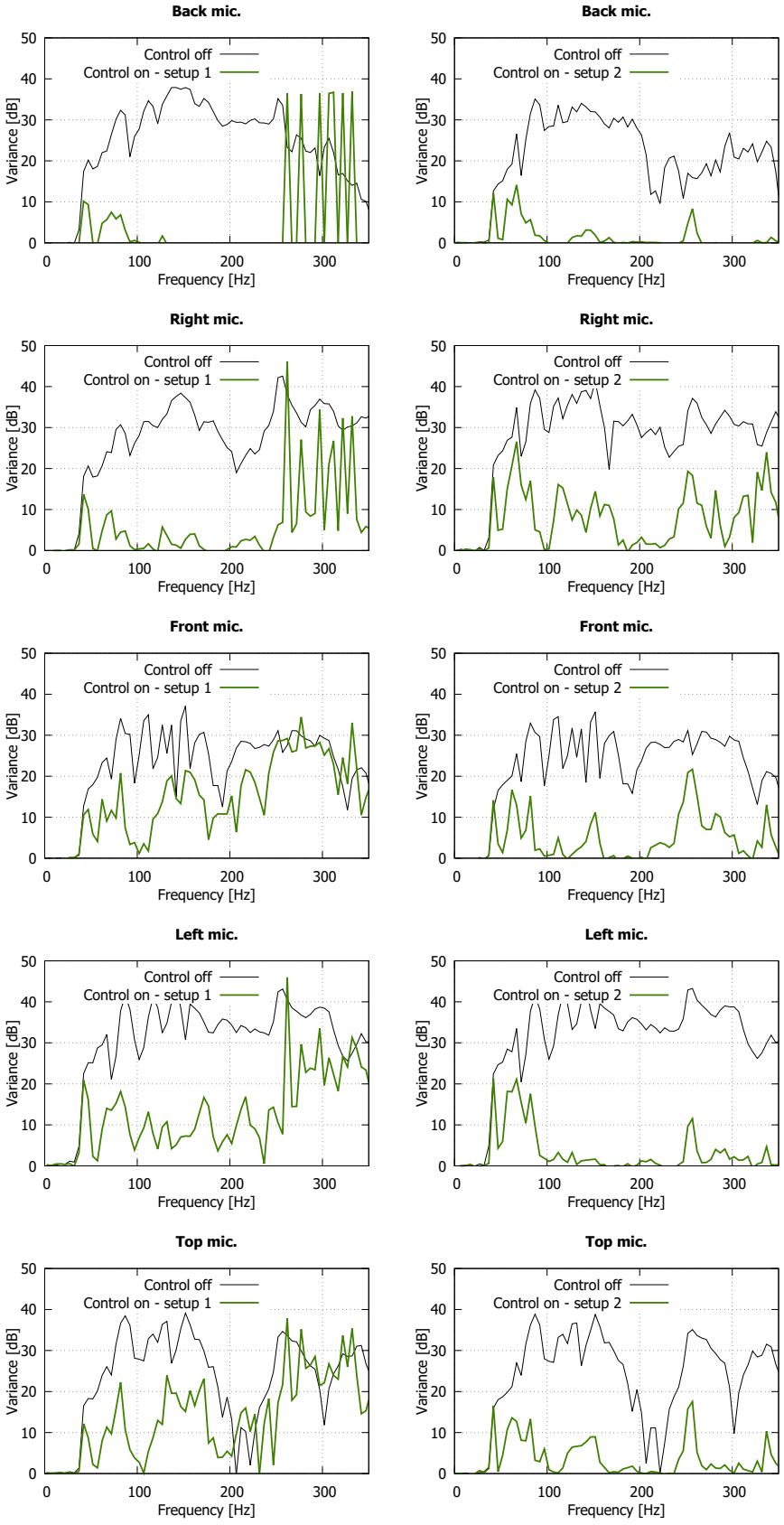


Figure 34: Variance of the error microphones signals versus frequency for both setups, distance $d = 0.1$ m.

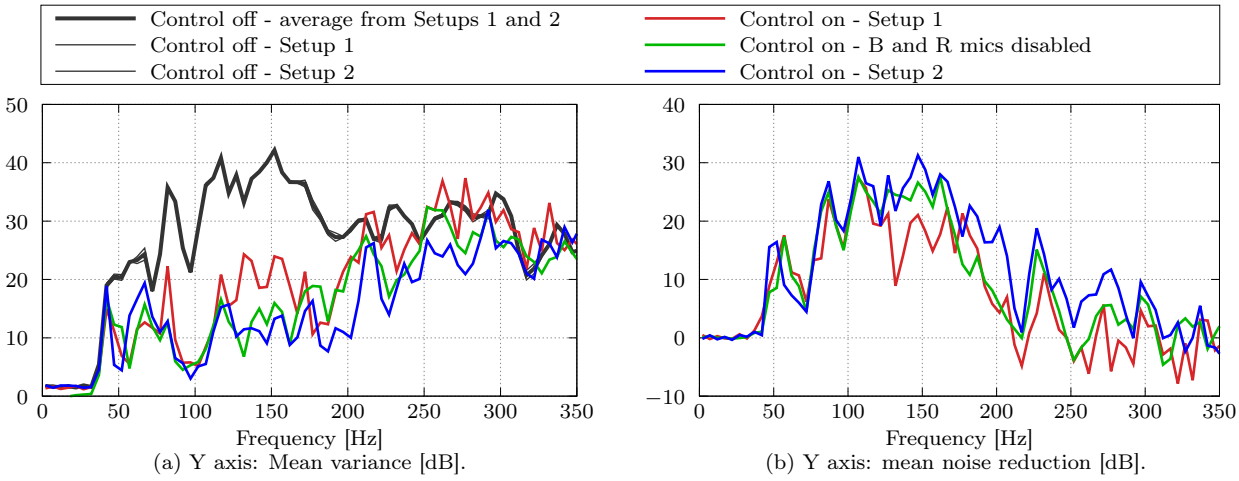


(a) Y axis: Mean variance [dB].

(b) Y axis: mean noise reduction [dB].

Figure 35: Active control performance at the distance $d = 0.1$ m. Both setups (1 and 2) as well as a third approach with back and right microphones disabled are examined [36].

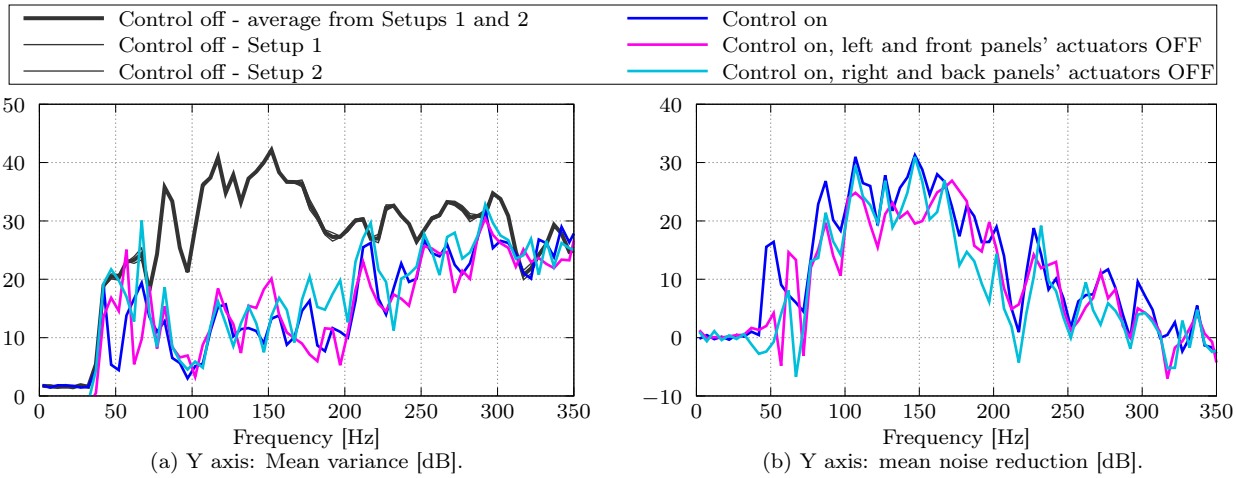


(a) Y axis: Mean variance [dB].

(b) Y axis: mean noise reduction [dB].

Figure 36: Active control performance at the distance $d = 0.1$ m, Setup 2. The following approaches are examined: active control off, active control on, active control on but front and left panels' actuators disabled, active control on but back and right panels' actuators disabled [36].

Around 100 Hz the results for all three approaches with control on become more similar. This indicates the robustness of the proposed system as well as provides a possibility to simplify the system in a particular configuration [36].

## 3.4. Conclusions

Prior to the research described in this dissertation, the lightweight device casing was employed in the active control system located in an enclosure whose walls were covered with acoustic foam. Device casing was then distant from the reflective walls. Efficiency of such setup in terms of a global noise reduction was confirmed. In Chapter 3, the novel approach to active structural acoustic control by means of lightweight device casing interacting with a reflective wall and a corner is described in details. The presented approach is closer to realistic, industrial and/or household, commonly encountered environments, than the laboratory enclosures whose walls are covered with acoustic foam. The goal of presented research was to analyze the behaviour of the active control system if the device casing was placed close to the reflective surfaces.

Chapter 3.2 presents a preliminary analysis of both primary and secondary paths, in case of the device casing placed at a rigid reflective wall. The experiment allowed to notice the consequences of placing the device casing at the wall in terms of the employed system operation, and provided information about the beneficial distances between the casing and the wall in terms of magnitude decrease at the specific frequencies.

Chapter 3.3 contains a thorough analysis of the primary and secondary paths, and the active control system performance, in case of the device casing placed in a corner. Rigid and reflective corner built of two walls was intentionally placed close to the casing to facilitate the active control system operation.

Noise source inside the casing may be visualized as surrounded by a sphere on which the error microphones are located. If the casing is distant from the laboratory walls, the sphere is limited to a hemisphere by a floor. If the reflective corner is introduced, then the hemisphere is further reduced to one-eighth of the sphere. Such resulting surface is smaller thus can be more densely covered with the error sensors if the number of them is maintained. Shorter distances between sensors mean that the active control system's operation is facilitated.

Results showed that an appropriate error microphones' arrangement and a proper corner-casing distance may lead to a global noise reduction level enhancement in a wide frequency range, and the results are of the same quality or better than the

ones achieved inside the acoustic foam-covered laboratory. It was noticed that at the specific distance between the casing and the corner it was more beneficial to use Setup 2 of the error microphones, i.e. to move back and right error microphones from the narrow space between the casing and the corner to the other side of the device casing. As back and right error microphones were then closer to the other ones, acoustic emission was observable in a wider frequency range, what implied a wider frequency range of a global noise reduction, and an increase of its levels.

Another conclusion from this research was that the error microphones placed in a narrow space between the casing and the corner may negatively impact the active control performance, and for the specific distance values it may be more beneficial to turn them off in terms of the active control system's performance.

The performed experiments and results' analysis provided a detailed insight into the employed active control system's operation, allowing to extend its applications to the realistic environments where the device casing may be placed close to the reflective surfaces. The results showed that such casing's placement does not negatively impact the active control system's performance in terms of a global noise reduction, and a proper setup of the error microphones and reflective surfaces may even lead to its levels' enhancement. Also, control system may be simplified if coupled to the reflective walls — number of both sensors and actuators may be reduced.

# 4. Interactions between panels in the double-panel structures

## 4.1. Introduction

As stated in Chapter 1.3, a casing enclosing noise-generating device may be employed for the purposes of noise and vibration reduction. Such casing may be built of single- or double panels, depending on the research scenario. In the following Chapter, research is focused on a double-panel structure, which forms a double wall of the rigid casing (which is described in Chapter 2.2). Panels of the structure interact with each other by means of solenoids. The influence of proposed modification on vibroacoustic properties of the double-panel structure is examined.

In Chapter 4.2, laboratory setups used for the research experiments are described. Chapter 4.3 presents a summary of different approaches to modeling of both single panels and double-panel structures, which were implemented to better understand the vibroacoustics of the examined panels. Chapter 4.4.1 contains the results from a research experiment with one (central) solenoid mounted between the panels of the double-panel structure. The influence of such modification on vibrations of the radiating panel is analyzed. In Chapter 4.4.2, five solenoids are introduced as the couplings between the panels. RMS levels of measured vibrations are determined for different scenarios with varying number of activated couplings and duty cycle of PWM signal. Then, Power Spectral Density (PSD) estimates are analyzed (Chapter 4.4.3), and Sound Transmission Loss is estimated based on the signals acquired by the microphones (Chapter 4.4.4). Hence, a thorough analysis of vibroacoustic properties of the examined double-panel structure is carried out.

## 4.2. Experimental setup

In the experiments with a modified double-panel structure, a rigid device casing (described in details in Chapter 2.2) was employed, as there was a possibility to build its walls of the double panels. The double-panel structure was modified by means of the electromagnetic couplings - solenoids (described in Chapter 2.3.4). Figure 37 presents a photograph of the laboratory setup with external microphone

and outer surroundings in the laboratory enclosure visible, and a scheme of the whole laboratory enclosure with surroundings.

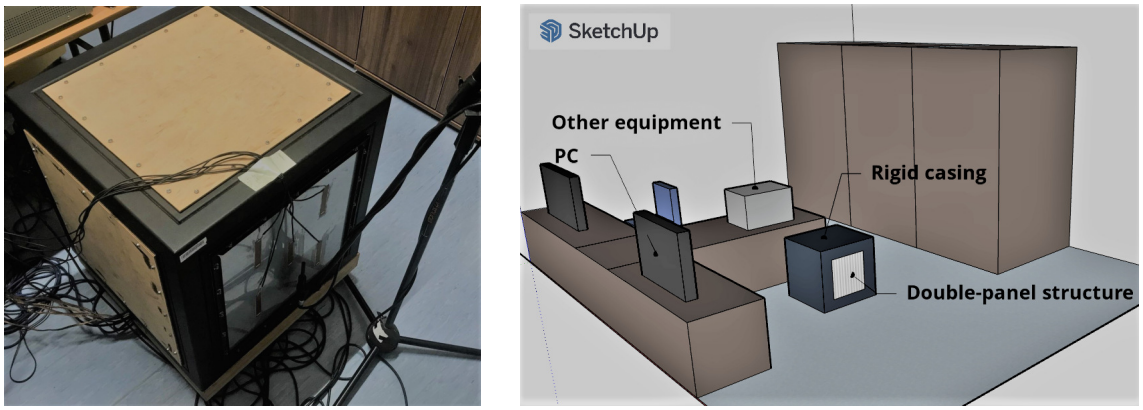


(a) (b)

Figure 37: (a) Photograph of the laboratory setup. (b) Scheme of the laboratory enclosure.

### 4.2.1. Experimental setup with one solenoid between the panels of the double-panel structure

The results from the experiments described in Chapters 4.2.1 and 4.4.1 were also published in [39], and the following analyses contain the novel description of these results as well as extend the topic.

In a preliminary experiment with the double-panel structure, panels of the structure were coupled by means of one solenoid. Depending on the research scenario, the solenoid was either turned on (if its coil was supplied with voltage) or off (if there was no voltage applied and the solenoid parts acted as the mass loadings only). Voltage signal was modulated with the use of Pulse Width Modulation (PWM) method. Its peak-to-peak value was 11 V [39].

The solenoid's coil was mounted at the incident panel's centre, on its outer side. The solenoid's core was mounted at the radiating panel's centre, on its inner side. Vibrations of the radiating panel were measured with the use of laser vibrometer Polytec PDV-100 for both scenarios (solenoid turned on or off). Hence, each measurement was acquired twice on a grid of 49 points ($7 \times 7$) marked on the radiating panel [39]. Figure 38 presents a scheme of the radiating panel with green diamond-shaped markers representing approximate areas of measurements at the intersections

of the grid lines and along the edges of the panel's vibrating surface. First measurement at each point was acquired when the solenoid was turned off, and the second one was acquired when the solenoid was turned on.

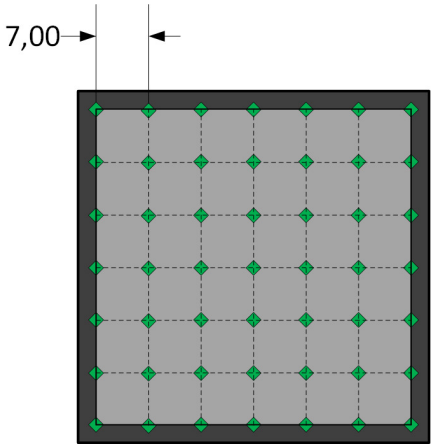


Figure 38: Grid marked on the radiating panel (dimensions in cm).

Low resolution of the grid marked on the radiating panel was justified by the solenoid's properties limiting the technical availabilities in the system. The temperature of the solenoid's coil raised quickly when the voltage was applied, and the temperature value was dependent on the level of voltage. After specific amount of time, a local increase of temperature value (up to c.a. 40 °C) around the electromagnetic coupling was observed if the element was turned on. Such effect may possibly lead to a shifting of resonant frequencies of the panels [131]. Hence, as vibration at each point of the grid had to be measured twice and only one point could be examined at once due to the use of laser vibrometer, a total amount of time needed to conduct the experiment increased. Thus, there was a greater risk of temperature increase around the coupling in case of a higher grid resolution, and this may impact reliability of the measurements [39].

### 4.2.2. Experimental setup with five solenoids between the panels of the double-panel structure

The results from the research described in the Chapters 4.2.2, 4.4.2 and 4.4.3 were also published in [81, 96], and the following analyses contain the novel description of these results as well as extend the topic.

After the preliminary experiment with one coupling, number of couplings be-

tween the panels was increased to 5, as the results from [39] were not satisfactory in terms of vibration reduction on the radiating panel. The experimental setup is presented in Figure 39. Besides of the rigid casing, the setup consisted of a loudspeaker (as a noise source placed inside the casing), solenoids between the panels, MFC elements (which were used to measure vibration of the radiating panel), and microphones.

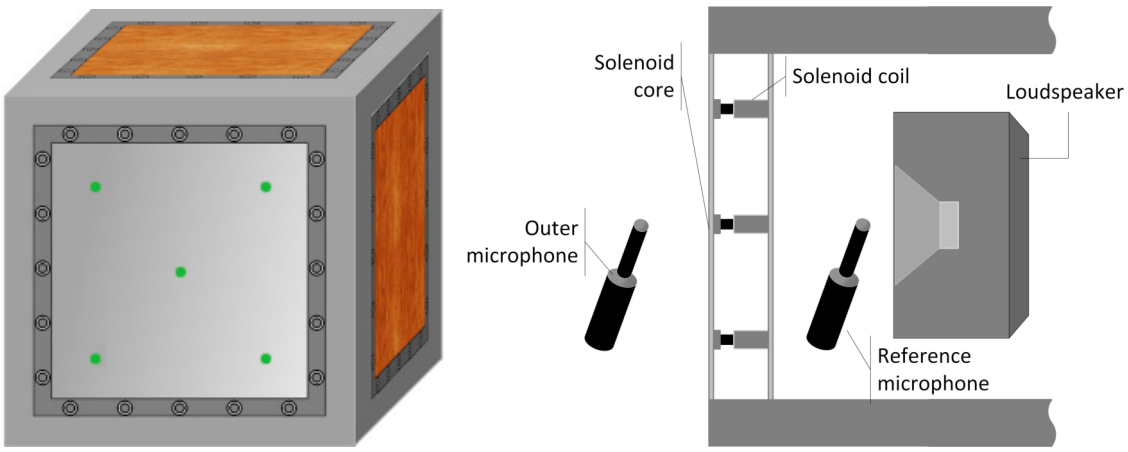


(a) (b)

Figure 39: Laboratory setup (based on [81]). (a) Scheme of the casing (front view). (b) Scheme of the double-panel structure modification (side view).

In the experiments with five electromagnetic couplings, a rigid casing was employed (described in details in Chapter 2.2). The noise source was placed inside the casing on a sound-insulated basis. Left, right, back and top casing walls were built of single plywood panels. Layer of acoustic foam (420 mm × 420 mm × 40 mm) was attached to each of these panels on their inner side to reinforce sound-insulating properties of the whole structure [81]. Such foam's properties are high density and high airflow resistivity [132]. Front casing wall was built of double thin steel panels, which are distant from each other by 50 mm. The inner panel, also called the incident panel [35], has a thickness of 0.6 mm, and the outer panel, also called the radiating panel [35], has a thickness of 0.5 mm [81]. The structure was designed to be asymmetrical to provide different resonant frequencies of the panels. Asymmetrical double-panel structure have an important advantage over the symmetrical ones, as in the case of active control system, the problem of lack of observability in the structure's air cavity can be easily avoided [133].

As the double-panel structure is a modified one, there are electromagnetic elements between the panels. The solenoids are described in details in Chapter 2.3.4. One of the mounted coils is presented in Fig. 40.

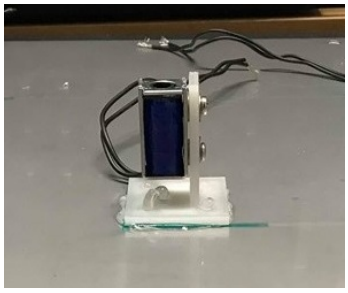

Figure 40: Mounting of the solenoid coils to the outer side of the incident panel ([96], [81]).

To measure vibration of the radiating panel, five MFC elements (M8514-P2) were glued to the outer side of the panel's surface with the use of epoxy glue [81]. The choice of epoxy glue was dictated by the rigidity of connection between the MFCs and the panel's surface that it may provide. It was assumed that the quality of MFCs mounting was high enough not to affect the experimental measurements significantly. To ensure the stability of experimental measurements, performance of all MFCs was checked with the use of reference input.

The positions of MFCs and solenoids were chosen based on the shape of mode (3, 3), which looks similar in case of both single panels and double-panel structures. The similarity of (3, 3) modeshapes between the single and double panels is presented in Fig. 41. Fig. 41a presents simulated mode (3, 3) shape of a single panel. Figs. 41b–41d present simulated mode (3, 3) shapes of the radiating panel of the double-panel wall for zero couplings between the panels, five mass loadings, and five activated couplings, respectively. Mode (3, 3) shape is characterized by regularly distributed nine areas of vibrations divided by the nodal lines. There are five highest amplitude peaks characterized by the same phase in five areas of the panel.

Mode (3, 3) shape of a single panel, shown in Fig. 41a, was calculated based on the equation for the mode shape functions being the product of two independent beam functions [35]:

$$\phi_{mn}(x, y) = X_m(x) \cdot Y_n(y). \tag{6}$$

Mode (3, 3) shapes of the radiating panel of the double-panel structure, shown in

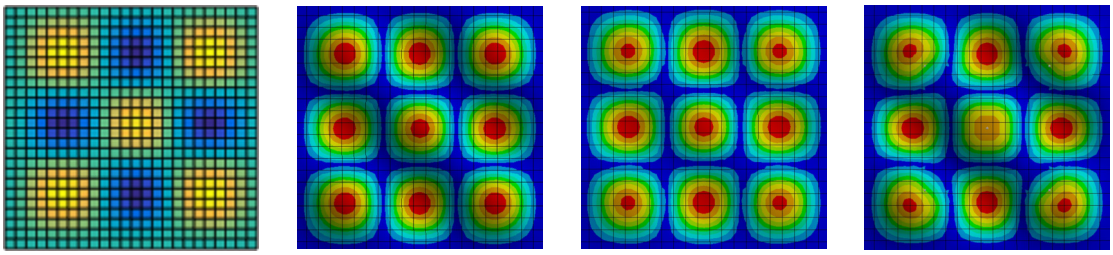

(a) (b) (c) (d)

Figure 41: (**a**) Simulated mode (3,3) shape of a single panel [81]. (**b**) Numerical model of the radiating panel's mode (3,3) shape without couplings [81]. (**c**) Numerical model of the radiating panel's mode (3,3) shape with 5 disabled solenoids [81]. (**d**) Numerical model of the radiating panel's mode (3,3) shape with five enabled solenoids [81].

Figs. 41b–41d, were obtained numerically with the use of ANSYS software. Fig. 41b presents scenario of an unmodified double-panel structure with enclosed air cavity and without the couplings. In the next scenario (Fig. 41c), five solenoids are introduced, but as the concentrated mass loadings only. In such scenario, voltage is not applied to the coils. If there is an electromotive force induced in the coils, then the cores are being held inside the coils' centres and another scenario has to be modelled. Fig. 41d presents how the mode (3, 3) differs from the previous ones if the couplings are activated. In the model, it is assumed that solenoids act like the concentrated masses connected with the springs of an assumed stiffness [81]. The areas of vibration on the radiating panel's surface become irregular if masses and springs are added to the system, but the differences between the highest amplitude peaks' positions are negligible. Hence, shape of (3, 3) mode was used as a reference when choosing the positions of the elements.

MFC elements glued to the surface of the radiating panel were numbered as MFC1, MFC2, MFC3, MFC4 and MFC5. Solenoids were numbered as C1, C2, C3, C4 and C5. Fig. 42 presents distribution of both MFCs and solenoids as a scheme. Green diamond-shaped markers with corresponding numbers represent the elements' positions. The MFCs are mounted on the surface of the radiating panel, and the solenoids are located between the panels.

It has to be emphasized that a regular placement of both MFC elements and

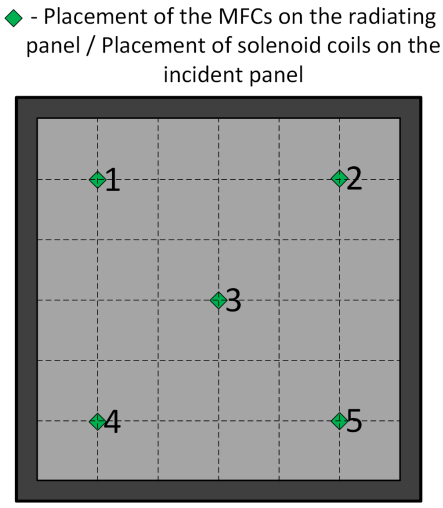


Figure 42: The schematic representation of the MFCs and solenoids placements, based on [81].

solenoids may not be optimal in terms of controllability and observability measures in the noise frequency band under consideration [81]. The goal of these experiments was to identify benefits of double-panel structure modifications in terms of noise and vibration reduction.

## 4.3. Modeling of single panels and double-panel structures

### 4.3.1. Sound source localization

In the analytically derived models of different phenomena encountered in the field of acoustics, like Sound Transmission Loss models, terms such as azimuth angle or elevation angle may appear. They refer to a sound source localization, which may be described in 3 dimensions by two angles and a distance [134].

Figure 43 presents three components of sound source localization description. Azimuth angle $\varphi$ is in the horizontal plane $(0 \pm 180°)$. Elevation angle $\theta$ is in the vertical plane $(0 \pm 90°)$. Distance $\Delta$ is in depth $(0–\infty)$ [134].

### 4.3.2. Single isotropic panels with or without mass loading

To compare the behaviour of single panels and double-panel structures, the single panels were modeled first. Kirchoff-Love model represents the single isotropic panel's

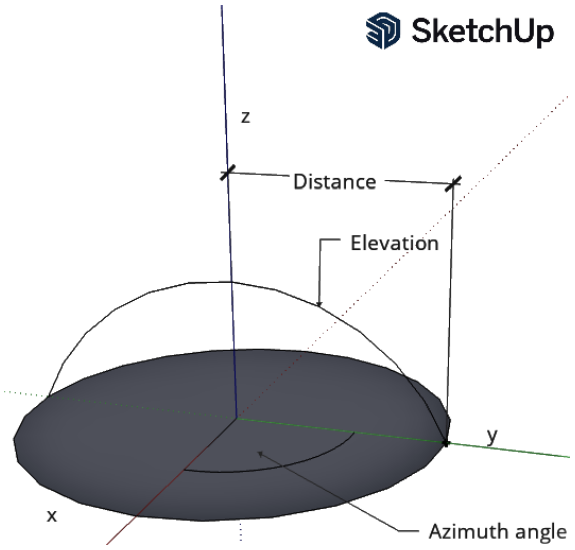


Figure 43: Sound source localization (based on [134]).

vibration subjected to a lateral static loading $q(x, y)$ ([135]):

$$D\left(\frac{\partial^4 W(x,y)}{\partial x^4} + 2\frac{\partial^4 W(x,y)}{\partial x^2 \partial y^2} + \frac{\partial^4 W(x,y)}{\partial y^4}\right) = q(x,y); \tag{7}$$

where: $W(x, y)$ — a panel lateral displacement's amplitude, $D$ - flexural rigidity of a panel.

If a scenario of the panel's free vibration is considered, then the lateral loading is replaced with an inertial force ([136]):

$$D\left(\frac{\partial^4 W(x,y,t)}{\partial x^4} + 2\frac{\partial^4 W(x,y,t)}{\partial x^2 \partial y^2} + \frac{\partial^4 W(x,y,t)}{\partial y^4}\right) + \rho\frac{\partial^2 W(x,y,t)}{\partial t^2} = 0; \tag{8}$$

where: $W(x, y, t)$ — a function of the space coordinates $x$, $y$ and time $t$ [39].

In a simplified modeling approach, solenoid's core and coil may be treated as the mass loadings attached to both panels. The influence of a mass loading on a single panel was examined based on a model proposed by Chai [137], in which a Rayleigh method is proposed due to its simplicity.

In such model, a mass loading may be located at any point of the panel's surface, at $(k, h)$ coordinates and its mass is equal to $M$. Resonant frequencies $f_{mn}$ of a panel can be calculated by means of the following equation [137]:

$$f_{mn} = \frac{1}{2\pi}\sqrt{\frac{D_{mn}}{T_{mn}}}\ [\text{Hz}]. \tag{9}$$

As a scenario with fully clamped boundary conditions is considered, $D_{mn}$ and

$T_{mn}$ from Eq. (9) are defined as [137]:

For $m = 1$ and $n = 1$ :

$$D_{mn} = \frac{\pi^4 D}{4a^3b^3}(3b^4 + 3a^4 + 2a^2b^2); \tag{10}$$

$$T_{mn} = \frac{9ab\gamma}{64} + M\sin^4\left(\frac{\pi k}{a}\right)\sin^4\left(\frac{\pi h}{b}\right). \tag{11}$$

For $m = 1$ and $n = 2, 3, 4, ...$ :

$$D_{mn} = \frac{\pi^4 D}{32a^3b^3}[16b^4 + 3a^4(1 + 6n^2 + n^4) + 8a^2b^2(1 + n^2)]; \tag{12}$$

$$T_{mn} = \frac{3ab\gamma}{32} + M\sin^4\left(\frac{\pi k}{a}\right)\sin^2\left(\frac{n\pi h}{b}\right)\sin^4\left(\frac{\pi h}{b}\right). \tag{13}$$

For $m = 2, 3, 4, ...$ and $n = 1$ :

$$D_{mn} = \frac{\pi^4 D}{32a^3b^3}[3b^4(1 + 6m^2 + m^4) + 16a^4 + 8a^2b^2(1 + m^2)]; \tag{14}$$

$$T_{mn} = \frac{3ab\gamma}{32} + M\sin^2\left(\frac{\pi k}{a}\right)\sin^2\left(\frac{m\pi k}{a}\right)\sin^4\left(\frac{\pi h}{b}\right). \tag{15}$$

For $m = 2, 3, 4, ...$ and $n = 2, 3, 4, ...$ :

$$D_{mn} = \frac{\pi^4 D}{16a^3b^3}[b^4(1 + 6m^2 + m^4) + a^4(1 + 6n^2 + n^4) + \\ + 2a^2b^2(1 + m^2)(1 + n^2)]; \tag{16}$$

$$T_{mn} = \frac{ab\gamma}{16} + M\sin^2\left(\frac{\pi k}{a}\right)\sin^2\left(\frac{m\pi k}{a}\right)\sin^2\left(\frac{\pi h}{b}\right)\sin^2\left(\frac{n\pi h}{b}\right). \tag{17}$$

$\gamma$ in Eqs. 10–17 is a symbol for panel's mass per unit area. In a simulation, a steel panel of dimensions $a \times b = 0.42$ m $\times$ 0.42 m $\times$ 0.0006 m is considered. Young modulus $E$ was 200 GPa, Poisson's ratio $\nu$ was 0.3, and steel density $\rho = 7850\frac{\text{kg}}{\text{m}^3}$ [39]. An influence of a mass loading placed at the different points of the panel on its resonant frequencies is examined to check how single mass loading affects the isotropic single panel's vibroacoustic properties. It is assumed that $m = 1, 2, 3$ and $n = 1, 2, 3$. In a reference case, mass loading $M$ is 0 g, hence, the resonant frequencies as of an unloaded steel panel are calculated (Table 8).

In the first case, mass loading $M = 9$ g is placed at the panel's centre, i.e. $k = 0.5a$ and $h = 0.5b$. Resonant frequencies are shown in Table 9.

In the second case, mass loading $M = 9$ g is placed at $k = \frac{1}{6}a$ and $h = \frac{1}{6}b$. Resonant frequencies are shown in Table 10.

Table 8: Natural frequencies $f_{mn}$ (Hz), $M$=0 g, based on [137], [39].

| m \ n | 1 | 2 | 3 |
|---|---|---|---|
| 1 | 30.78 | 63.04 | 105.78 |
| 2 | 63.04 | 93.76 | 135.83 |
| 3 | 105.78 | 135.83 | 177.3 |

Table 9: Natural frequencies $f_{mn}$ (Hz), $M$=9 g located at the panel's centre, based on [137], [39].

| m \ n | 1 | 2 | 3 |
|---|---|---|---|
| 1 | 29.66 | 63.04 | 100.15 |
| 2 | 63.04 | 93.76 | 135.83 |
| 3 | 100.15 | 135.83 | 163.68 |

Table 10: Natural frequencies $f_{mn}$ (Hz), $M$=9 g located at $k = \frac{1}{6}a$ and $h = \frac{1}{6}b$, based on [137].

| m \ n | 1 | 2 | 3 |
|---|---|---|---|
| 1 | 30.77 | 63.03 | 105.75 |
| 2 | 63 | 93.48 | 135.28 |
| 3 | 105.68 | 135.28 | 176.35 |

If the mass is located at the panel's centre, it influences resonant frequencies $f_{11}$, $f_{13}$, $f_{31}$ and $f_{33}$, causing them to decrease. At the same time, resonant frequencies $f_{12}$, $f_{21}$, $f_{22}$, $f_{23}$ and $f_{32}$ remain the same. It is observed that, as expected in case of an isotropic square panel, resonant frequencies $f_{mn}$ and $f_{nm}$ are equal for each $m \neq n$ [39].

Change of the mass loading's location to $k = \frac{1}{6}a$ and $h = \frac{1}{6}b$ does not impact the panel's properties. The differences between frequencies in Tables 8 and 10 are negligible. Similar effect was observed for the cases of $(k, h) = \left\{(\frac{1}{6}a, \frac{5}{6}b), (\frac{5}{6}a, \frac{1}{6}b), (\frac{5}{6}a, \frac{5}{6}b)\right\}$. Hence, in this particular case, mass was increased tenfold and the simulation was performed once again. The results are shown in Table 11.

Even after an increase of mass from 9 g to 90 g, a significant decrease of resonant

Table 11: Natural frequencies $f_{mn}$ (Hz), $M$=90 g located at $k = \frac{1}{6}a$ and $h = \frac{1}{6}b$, based on [137].

| m \ n | 1 | 2 | 3 |
|---|---|---|---|
| 1 | 30.73 | 62.93 | 105.54 |
| 2 | 62.61 | 91.03 | 130.62 |
| 3 | 104.84 | 130.62 | 168.41 |

frequency values is observed only for $f_{23}$, $f_{32}$ and $f_{33}$. Hence, such mass loading may decrease resonant frequency of mode (3, 3), but in the laboratory setup it would be undesired to load the panels with five masses summing up to 0.5 kg. Is it noteworthy that one mass loading of a mass equal to 9 g, located at the panel's centre, causes a higher decrease of a mode (3, 3) resonant frequency than a mass loading of 90 g located at ($k = \frac{1}{6}a$, $h = \frac{1}{6}b$).

### 4.3.3. Single orthotropic panels

Besides of isotropic single panels, the more complex orthotropic panels were also modelled. Free vibration of a thin, elastic orthotropic panel may be expressed as [138]:

$$D_x \frac{\partial^4 w}{\partial x^4} + 2B \frac{\partial^4 w}{\partial x^2 \partial y^2} + D_y \frac{\partial^4 w}{\partial y^4} + \rho h \frac{\partial^2 w}{\partial t^2} + \gamma h \frac{\partial w}{\partial t} = 0; \tag{18}$$

where:

$$D_x = \frac{E_x h^3}{12(1 - \nu_x \nu_y)};$$
$$D_y = \frac{E_y h^3}{12(1 - \nu_x \nu_y)}. \tag{19}$$

Symbols meaning is: $w$ — a panel lateral displacement's amplitude, $D_x$, $D_y$ — flexural rigidities, $B = D_x \nu_y + \frac{Gh^3}{6}$, $G$ — rigidity modulus, $\nu_x$, $\nu_y$ — Poisson ratios for the panel's material ($E_x \nu_y = E_y \nu_x$), $\rho$ — mass density per unit volume of the panel, $h$ — panel's thickness, $t$ — continuous time, $\gamma$ — damping ratio.

Undamped form of Eq. (18) is:

$$D_x \frac{\partial^4 w}{\partial x^4} + 2B \frac{\partial^4 w}{\partial x^2 \partial y^2} + D_y \frac{\partial^4 w}{\partial y^4} - \rho h \omega^2 W = 0. \tag{20}$$

For the fully clamped panel, its natural frequencies may be calculated from [138]:

$$\omega_{mn} = \sqrt{\frac{B}{\rho h}}\left[\frac{D_x}{B}\left(\frac{p\pi}{a}\right)^4 + 2\left(\frac{p\pi}{a}\right)^2\left(\frac{q\pi}{b}\right)^2 + \frac{D_y}{B}\left(\frac{q\pi}{b}\right)^4\right]^{1/2}; \tag{21}$$

where $p$ and $q$ can be determined by considering two auxiliary problems of Levy's type [139]. Their integer parts stand for the eigenfrequency number ($p$, $q$), e.g. if the integer parts of $p$ and $q$ equal 1 and 1, they are used to calculate natural frequency of (1, 1) mode.

First auxiliary problem is defined as [139]:

$$\begin{aligned} c_2 &= \cos(q\pi); \\ s_2 &= \sin(q\pi); \\ \kappa &= \sqrt{2p^2\frac{B}{D_y} + q^2}; \\ C_2 &= \cosh(\kappa\pi); \\ S_2 &= \sinh(\kappa\pi); \\ 1 - c_2C_2 + \frac{B}{D_y}\left(2\frac{B}{D_y}\frac{q^2}{p^2} + \frac{q^4}{p^4}\right)^{-0.5} s_2S_2 &= 0. \end{aligned} \tag{22}$$

Second auxiliary problem is defined as [139]:

$$\begin{aligned} c_1 &= \cos(p\pi); \\ s_1 &= \sin(p\pi); \\ \theta &= \sqrt{2q^2\frac{B}{D_x} + p^2}; \\ C_1 &= \cosh(\theta\pi); \\ S_1 &= \sinh(\theta\pi); \\ 1 - c_1C_1 + \frac{B}{D_x}\left(2\frac{B}{D_x}\frac{p^2}{q^2} + \frac{p^4}{q^4}\right)^{-0.5} s_1S_1 &= 0. \end{aligned} \tag{23}$$

Functions $f_1(p, q)$ and $f_2(p, q)$ may be obtained from both problems. Eqs. (22)–(23) are transcendental, which means they have an infinite number of roots. Thus the problem can be solved by specifying values of both these functions within a specified range of both $p$ and $q$, and determining their contours for $f_1(p, q) = f_2(p, q) = 0$ (Fig. 44). Each intersection of the obtained functions' contours is considered as one solution (a $(p, q)$ pair).

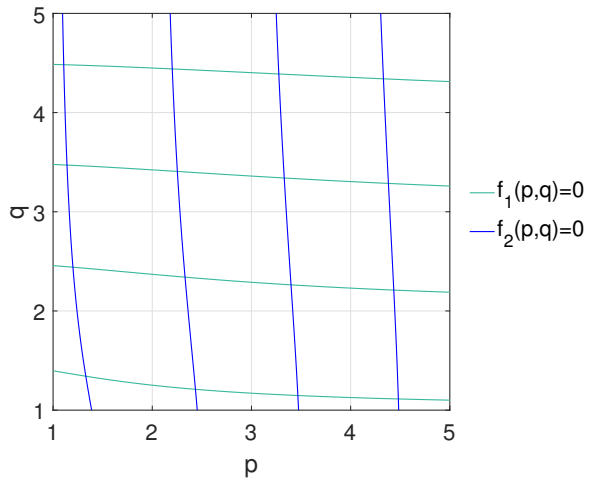


Figure 44: Contours of $f_1(p,q) = 0$ and $f_2(p,q) = 0$.

For modes $f_{mn}$, where $m = 1, 2, 3$ and $n = 1, 2, 3$, values of $p$ and $q$ calculated as described above are listed in Table 12. In the fifth column, natural radian frequencies $\omega_{ij}/\sqrt{D_x/\rho h a^4}$ for these modes are calculated based on Eq. (21). In the sixth column, obtained natural radian frequencies are validated using the results published by Sakata & Takahashi [140]. The assumptions are that all edges of the orthotropic panel are fully clamped and $B = D_x$ and $D_x = D_y$. While the percentage difference for the first mode is around 3%, other ones are below 1%. Such small differences are expected as there are errors in every method of approximate calculation of the panel's natural frequencies.

Table 12: Values of $p$ and $q$ and natural radian frequencies $\omega_{ij}/\sqrt{D_x/\rho h a^4}$ for modes $(m, n)$, where $m = 1, 2, 3$ and $n = 1, 2, 3$.

| $(m, n)$ | $p$ | $q$ | $b = a$, proposed model | $b = a$, Sakata & Takahashi [140] | Percentage diff. [%] |
|---|---|---|---|---|---|
| (1, 1) | 1.33 | 1.33 | 34.917 | 35.999 | 3.05 |
| (1, 2) | 1.2 | 2.44 | 72.972 | 73.405 | 0.59 |
| (1, 3) | 1.14 | 3.47 | 131.666 | 131.902 | 0.18 |
| (2, 1) | 2.44 | 1.21 | 73.21 | 73.405 | 0.27 |
| (2, 2) | 2.33 | 2.34 | 107.623 | 108.236 | 0.57 |
| (2, 3) | 2.25 | 3.41 | 164.73 | 165.023 | 0.18 |
| (3, 1) | 3.47 | 1.15 | 131.892 | 131.902 | 0.01 |
| (3, 2) | 3.4 | 2.26 | 164.502 | 165.023 | 0.32 |
| (3, 3) | 3.33 | 3.34 | 219.544 | 220.059 | 0.23 |

### 4.3.4. Unbounded double-panel structure

Acoustic performance of a double-panel structure may be evaluated by means of Sound Transmission Loss (STL) indicator. As an unbounded (infinite) double-panel structure is under consideration, $\tau$ (transmitted to incident pressure power ratio coefficient) [60] can be calculated as [141]:

$$\tau = -\frac{2j\rho_0^2 c^2 \sec^2\theta \sin(kd\cos\theta)}{AB[\sin^2(kd\cos\theta)] + [\rho_0^2 c^2 \sec\theta]}; \tag{24}$$

knowing that $A$ and $B$:

$$A = [j\omega m_1 + a_1 + \rho_0 c \sec\theta(1 - j\cot(kd\cos\theta))]; \tag{25}$$

$$B = [j\omega m_2 + a_2 + \rho_0 c \sec\theta(1 - j\cot(kd\cos\theta))]. \tag{26}$$

The following symbols are used: $j = \sqrt{-1}$, $d$ - depth of double-panel structure cavity, $\omega$ - angular frequency, $\rho_0$ - air density, $c$ - speed of sound in the air, $\theta$ - angle of acoustic wave incidence, $k$ - wave number, $m_i$ - area mass of $i$-th panel, $a_i$ - damping coefficient of $i$-th panel.

As $\tau$ is defined, Sound Transmission Loss can be calculated from the following equation [71]:

$$\text{STL} = 10\log_{10}\left(\frac{1}{\tau}\right) \text{ dB}. \tag{27}$$

Theory for single panels may be applied in the double-panel structures only at the low frequencies [142], where it is observed that double panels move with the same velocity and in the same phase. However, along with the increase of sound frequency, double panels start moving in the opposite phase. Such phenomenon is called mass-air-mass resonance [143]. At its frequency, air in the hermetic cavity acts like a spring of a specific stiffness [144] and influences the panels' vibrations. Mass-air-mass resonance is undesired, as it is observed that double-panel structure's performance significantly deteriorates around its frequency [145].

The case of infinite (unbounded) double-panel structure is the only one where a frequency of mass-air-mass resonance can be calculated as [146]:

$$f_{\text{mass-air-mass}} = \frac{1}{2\pi}\sqrt{\frac{\rho_0 c^2}{d}\frac{m_1 + m_2}{m_1 m_2}}; \tag{28}$$

where $m_1$ and $m_2$ are defined as follows (if material density is the same for both panels):

$$m_1 = h_1\rho; \tag{29}$$

$$m_2 = h_2\rho. \tag{30}$$

Such equation cannot be applied in the finite double-panel structures for an accurate estimation of a mass-air-mass resonant frequency. It gives only a rough approximation of $f_{\text{mass-air-mass}}$ [145] then. The real Sound Transmission Loss, as described in this dissertation, is much more complex and requires a detailed analytical or numerical modeling approach.

An estimation of Sound Transmission Loss for an examined steel double-panel structure was calculated based on Eqs. (24)–(30), assuming that: cavity depth $d = 0.05$ m, incident panel thickness $h_1 = 0.0006$ m, radiating panel thickness $h_2 = 0.0005$ m, steel density $\rho = 7850\frac{\text{kg}}{\text{m}^3}$, air density $\rho_0 = 1.21\frac{\text{kg}}{\text{m}^3}$ and speed of sound in air $c = 343\frac{\text{m}}{\text{s}}$. The results are shown in Fig. 45 in the frequency range 0–500 Hz.

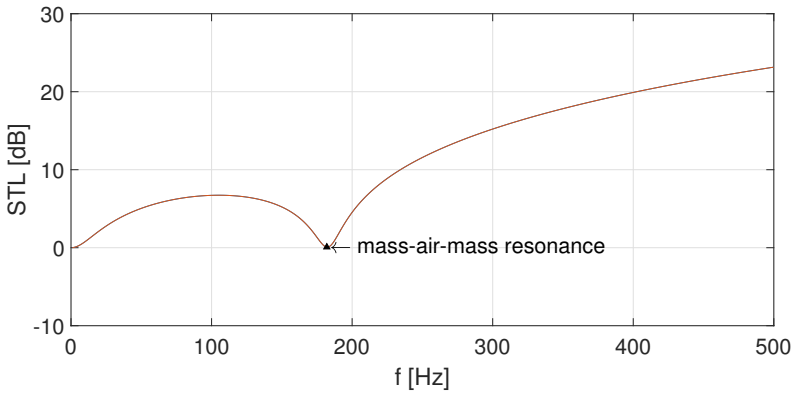


Figure 45: Estimate of Sound Transmission Loss for an unbounded double-panel structure.

In Fig. 45, the frequency of mass-air-mass resonance is 184 Hz, due to the frequency resolution equal to 1 Hz. Based on Eq. (28), this frequency equals 183.54 Hz. Hence, the model is implemented correctly. However, it cannot be used to estimate STL of a finite double-panel structure, as there is only one dip observed in STL curve in Fig. 45, and the acoustic performance of the real finite structures may be much more complex. The model described by Eq. (24) does not take into account enough number of parameters and phenomena during model derivation, to reliably reflect the behaviour of a finite double-panel structure.

Jakob and Möser stated in their article [147], that the real mass-air-mass resonant frequency is usually lower than the theoretical one calculated for an infinite double-panel structure. This is in contrast to the behaviour of the resonant frequencies of the double panels, as they decrease along with the growing dimensions of the structure.

### 4.3.5. Double-panel structure fully clamped on an infinite acoustic rigid baffle

Sound Transmission Loss of a double-panel structure with fully clamped boundary conditions may be modelled analytically or numerically. To check how an analytical model of STL for a double-panel structure fully clamped on an infinite acoustic rigid baffle differs from an analytical one developed for an unbounded structure, an approach of Xin et al. [99, 43] was implemented, and validated based on the data from [99]. As STL is defined as in Eq. (27), the power transmission coefficient $\tau$ being an element of the mentioned equation can be calculated as follows [99, 43]:

$$\tau(\varphi,\theta) = \frac{\Pi_r}{\Pi_{in}}; \tag{31}$$

where $\Pi_{in}$ (incident sound power) and $\Pi_r$ (transmitted sound power), respectively, can be calculated as follows [99, 43]:

$$\begin{aligned}\Pi_{in} = \frac{\rho_0\omega^2}{2c_0}\Bigg|4I^2\int\int_A e^{-2j(k_x x+k_y y)}dA \\ -4I\frac{\omega}{k_z}\sum_{m,n}\alpha_{1,mn}\int\int_A e^{-j(k_x x+k_y y)}\left(1-\cos\frac{2m\pi x}{a}\right)\times\left(1-\cos\frac{2n\pi y}{b}\right)dA \\ +\left(\frac{\omega}{k_z}\right)^2\sum_{mn,kl}\alpha_{1,mn}\alpha_{1,kl}\int\int_A\left(1-\cos\frac{2m\pi x}{a}\right)\left(1-\cos\frac{2n\pi y}{b}\right) \\ \times\left(1-\cos\frac{2k\pi x}{a}\right)\left(1-\cos\frac{2l\pi y}{b}\right)dA\Bigg|;\end{aligned} \tag{32}$$

$$\begin{aligned}\Pi_r = \frac{\rho_0\omega^2}{2c_0}\Bigg|\left(\frac{\omega}{k_z}\right)^2\sum_{mn,kl}\alpha_{2,mn}\alpha_{2,kl}\int\int_A\left(1-\cos\frac{2m\pi x}{a}\right) \\ \times\left(1-\cos\frac{2n\pi y}{b}\right)\left(1-\cos\frac{2k\pi x}{a}\right)\times\left(1-\cos\frac{2l\pi y}{b}\right)dA\Bigg|.\end{aligned} \tag{33}$$

$k_x$, $k_y$ and $k_z$ are the components of the wave vector $\mathbf{k} = k_x\hat{\mathbf{e}}_x + k_y\hat{\mathbf{e}}_y + k_z\hat{\mathbf{e}}_z$. Knowing the elevation angle $\varphi$ and azimuth angle $\theta$ of the incidence sound wave,

they can be calculated as follows [99, 43]:

$$\begin{aligned} k_x &= k_0 \sin\varphi \cos\theta; \\ k_y &= k_0 \sin\varphi \sin\theta; \\ k_z &= k_0 \cos\varphi; \end{aligned} \tag{34}$$

where $k_0 = \frac{\omega}{c_0}$.

The integrals in Eqs. (32)–(33) can be calculated as follows [99, 43]:

$$\begin{aligned} &\int\int_A e^{-2j(k_x x + k_y y)} dA = \\ &= \begin{cases} ab & \text{for } k_x = 0 \wedge k_y = 0 \\ \frac{ja(-1+e^{-2jk_y b})}{2k_y} & \text{for } k_x = 0 \wedge k_y \neq 0 \\ \frac{jb(-1+e^{-2jk_x a})}{2k_x} & \text{for } k_x \neq 0 \wedge k_y = 0 \\ -\frac{1}{4}\frac{(1-e^{-2jk_x a}-e^{-2jk_y b}+e^{-2j(k_x a+k_y b)})}{k_x k_y} & \text{for } k_x \neq 0 \wedge k_y \neq 0, \end{cases} \end{aligned} \tag{35}$$

$$\begin{aligned} &\int\int_A e^{-j(k_x x + k_y y)} \left(1 - \cos\frac{2m\pi x}{a}\right)\left(1 - \cos\frac{2n\pi y}{b}\right) dA = \\ &= \begin{cases} ab & \text{for } k_x = 0 \text{ and } k_y = 0 \\ \frac{4jn^2\pi^2 a(1-e^{-jk_y b})}{k_y(k_y^2 b^2 - 4n^2\pi^2)} & \text{for } k_x = 0 \text{ and } k_y \neq 0 \\ \frac{4jm^2\pi^2 b(1-e^{-jk_x a})}{k_x(k_x^2 a^2 - 4m^2\pi^2)} & \text{for } k_x \neq 0 \text{ and } k_y = 0 \\ -\frac{16m^2n^2\pi^4(1-e^{-jk_x a})(1-e^{-jk_y b})}{k_x k_y(k_x^2 a^2 - 4m^2\pi^2)(k_y^2 b^2 - 4n^2\pi^2)} & \text{for } k_x \neq 0 \text{ and } k_y \neq 0, \end{cases} \end{aligned} \tag{36}$$

$$\begin{aligned} &\int\int_A \left(1 - \cos\frac{2m\pi x}{a}\right)\left(1 - \cos\frac{2n\pi y}{b}\right) \\ &\times \left(1 - \cos\frac{2k\pi x}{a}\right)\left(1 - \cos\frac{2l\pi y}{b}\right) dA = \\ &= \begin{cases} \frac{9}{4}ab & \text{for } m = k \text{ and } n = l \\ \frac{3}{2}ab & \text{for } m = k \text{ and } n \neq l \\ \frac{3}{2}ab & \text{for } m \neq k \text{ and } n = l \\ ab & \text{for } m \neq k \text{ and } n \neq l. \end{cases} \end{aligned} \tag{37}$$

The coefficients $\alpha_{1,mn}$ and $\alpha_{2,mn}$ in Eqs. (32)–(33) are determined from the matrix equation [99, 43]:

$$\begin{bmatrix} T_{11,kl} & T_{12,kl} \\ T_{21,kl} & T_{22,kl} \end{bmatrix}_{2MN \times 2MN} \begin{Bmatrix} \alpha_{1,kl} \\ \alpha_{2,kl} \end{Bmatrix}_{2MN \times 1} = \begin{Bmatrix} F_{kl} \\ 0 \end{Bmatrix}_{2MN \times 1}; \tag{38}$$

where $\{\alpha_{1,kl}\}$, $\{\alpha_{2,kl}\}$ and $\{F_{kl}\}$, respectively, are defined as follows [99, 43]:

$$\{\alpha_{1,kl}\} = [\alpha_{1,11}\ \alpha_{1,21}\ ...\ \alpha_{1,M1}\ \alpha_{1,12}\ \alpha_{1,22}\ ...\ \alpha_{1,M2}\ ...\ \alpha_{1,MN}]^T_{MN\times 1}; \tag{39}$$

$$\{\alpha_{2,kl}\} = [\alpha_{2,11}\ \alpha_{2,21}\ ...\ \alpha_{2,M1}\ \alpha_{2,12}\ \alpha_{2,22}\ ...\ \alpha_{2,M2}\ ...\ \alpha_{2,MN}]^T_{MN\times 1}; \tag{40}$$

$$\{F_{kl}\} = 2j\omega\rho_0 I[f_{11}\ f_{21}\ ...\ f_{M1}\ f_{12}\ f_{22}\ ...\ f_{M2}\ ...\ f_{MN}]^T_{MN\times 1}; \tag{41}$$

and $f_{mn}$ from Eq. (41) is calculated as follows [99, 43]:

$$f_{mn}(k_x,k_y) = \begin{cases} ab & \text{for } k_x = 0 \text{ and } k_y = 0 \\ \frac{4jn^2\pi^2 a(1-e^{-jk_y b})}{k_y(k_y^2 b^2 - 4n^2\pi^2)} & \text{for } k_x = 0 \text{ and } k_y \neq 0 \\ \frac{4jm^2\pi^2 b(1-e^{-jk_x a})}{k_x(k_x^2 a^2 - 4m^2\pi^2)} & \text{for } k_x \neq 0 \text{ and } k_y = 0 \\ -\frac{16m^2n^2\pi^4(1-e^{-jk_x a})(1-e^{-jk_y b})}{k_x k_y(k_x^2 a^2 - 4m^2\pi^2)(k_y^2 b^2 - 4n^2\pi^2)} & \text{for } k_x \neq 0 \text{ and } k_y \neq 0. \end{cases} \tag{42}$$

Elements from the first array on the left in Eq. (38) ($T_{11,kl}$, $T_{12,kl}$, $T_{21,kl}$ and $T_{22,kl}$, respectively) are defined as follows [99, 43]:

$$[T_{11,kl}]_{MN\times MN} = 4D_1\pi^4 ab(\Delta_1^{*1} + \Delta_1^{*2} + \Delta_1^{*3}) - (m_1\omega^2 + j\omega\rho_0 \frac{2\omega e^{2jk_z H}}{k_z(1-e^{2jk_z H})})(\Delta_2^{*1} + \Delta_2^{*2} + \Delta_2^{*3} + \Delta_2^{*4}); \tag{43}$$

$$[T_{12,kl}]_{MN\times MN} = j\omega\rho_0 \frac{2\omega e^{2jk_z H}}{k_z(1-e^{2jk_z H})} \times (\Delta_2^{*1} + \Delta_2^{*2} + \Delta_2^{*3} + \Delta_2^{*4}); \tag{44}$$

$$[T_{21,kl}]_{MN\times MN} = [T_{12,kl}]_{MN\times MN}; \tag{45}$$

$$[T_{22,kl}]_{MN\times MN} = 4D_2\pi^4 ab(\Delta_1^{*1} + \Delta_1^{*2} + \Delta_1^{*3}) - (m_2\omega^2 + j\omega\rho_0 \frac{2\omega e^{2jk_z H}}{k_z(1-e^{2jk_z H})})(\Delta_2^{*1} + \Delta_2^{*2} + \Delta_2^{*3} + \Delta_2^{*4}). \tag{46}$$

$D_1$ and $D_2$ are described by the following equation [99, 43]:

$$D_i = \frac{E_i h_i^3(1+j\eta_i)}{12(1-\nu_i^2)}. \tag{47}$$

The elements $\Delta_1^{*1}$, $\Delta_1^{*2}$, $\Delta_1^{*3}$, $\Delta_2^{*1}$, $\Delta_2^{*2}$, $\Delta_2^{*3}$, $\Delta_2^{*4}$ from Eqs. (43)–(46) can be calculated based on the following equations (Eqs. (48)–(60)) [99, 43]:

$$\lambda_{1,mn}^{*1} = 3\left(\frac{m}{a}\right)^4 + 3\left(\frac{n}{b}\right)^4 + 2\left(\frac{m}{a}\right)^2\left(\frac{n}{b}\right)^2; \tag{48}$$

$$\Delta_1^{*1} = \begin{bmatrix} \lambda_{1,11}^{*1} & & & & & & & & & & & \\ & \lambda_{1,21}^{*1} & & & & & & & & & & \\ & & ... & & & & & & & & & \\ & & & \lambda_{1,M1}^{*1} & & & & & & & & \\ & & & & \lambda_{1,12}^{*1} & & & & & & & \\ & & & & & \lambda_{1,22}^{*1} & & & & & & \\ & & & & & & ... & & & & & \\ & & & & & & & \lambda_{1,M2}^{*1} & & & & \\ & & & & & & & & ... & & & \\ & & & & & & & & & \lambda_{1,MN}^{*1} \end{bmatrix}_{MN \times MN} ; \quad (49)$$

$$\lambda_{1,n}^{*2} = \frac{2n^4}{b^4} \begin{bmatrix} 0 & 1 & 1 & ... & 1 \\ 1 & 0 & 1 & ... & 1 \\ 1 & 1 & 0 & ... & ... \\ ... & ... & ... & ... & 1 \\ 1 & 1 & ... & 1 & 0 \end{bmatrix}_{M \times N} ; \quad (50)$$

$$\Delta_1^{*2} = \begin{bmatrix} \lambda_{1,1}^{*2} & & & \\ & \lambda_{1,2}^{*2} & & \\ & & ... & \\ & & & \lambda_{1,n}^{*2} \end{bmatrix}_{MN \times MN} ; \quad (51)$$

$$\lambda_1^{*3} = \frac{2}{a^4} \begin{bmatrix} 1^4 & & & \\ & 2^4 & & \\ & & ... & \\ & & & M^4 \end{bmatrix}_{M \times N} ; \quad (52)$$

$$\Delta_1^{*3} = \begin{bmatrix} 0 & \lambda_1^{*3} & \lambda_1^{*3} & ... & \lambda_1^{*3} \\ \lambda_1^{*3} & 0 & \lambda_1^{*3} & ... & \lambda_1^{*3} \\ \lambda_1^{*3} & \lambda_1^{*3} & 0 & ... & ... \\ ... & ... & ... & ... & \lambda_1^{*3} \\ \lambda_1^{*3} & \lambda_1^{*3} & ... & \lambda_1^{*3} & 0 \end{bmatrix}_{MN \times MN} ; \quad (53)$$

$$\Delta_2^{*1} = \frac{9ab}{4} \begin{bmatrix} 1 & & & \\ & 1 & & \\ & & ... & \\ & & & 1 \end{bmatrix}_{MN \times MN} ; \tag{54}$$

$$\lambda_2^{*2} = \frac{3ab}{2} \begin{bmatrix} 0 & 1 & 1 & ... & 1 \\ 1 & 0 & 1 & ... & 1 \\ 1 & 1 & 0 & ... & ... \\ ... & ... & ... & ... & 1 \\ 1 & 1 & ... & 1 & 0 \end{bmatrix}_{M \times N} ; \tag{55}$$

$$\Delta_2^{*2} = \begin{bmatrix} \lambda_2^{*2} & & & \\ & \lambda_2^{*2} & & \\ & & ... & \\ & & & \lambda_2^{*2} \end{bmatrix}_{MN \times MN} ; \tag{56}$$

$$\lambda_2^{*3} = \frac{3ab}{2} \begin{bmatrix} 1 & & & \\ & 1 & & \\ & & ... & \\ & & & 1 \end{bmatrix}_{M \times N} ; \tag{57}$$

$$\Delta_2^{*3} = \begin{bmatrix} 0 & \lambda_2^{*3} & \lambda_2^{*3} & ... & \lambda_2^{*3} \\ \lambda_2^{*3} & 0 & \lambda_2^{*3} & ... & \lambda_2^{*3} \\ \lambda_2^{*3} & \lambda_2^{*3} & 0 & ... & ... \\ ... & ... & ... & ... & \lambda_2^{*3} \\ \lambda_2^{*3} & \lambda_2^{*3} & ... & \lambda_2^{*3} & 0 \end{bmatrix}_{MN \times MN} ; \tag{58}$$

$$\lambda_2^{*4} = ab \begin{bmatrix} 0 & 1 & 1 & ... & 1 \\ 1 & 0 & 1 & ... & 1 \\ 1 & 1 & 0 & ... & ... \\ ... & ... & ... & ... & 1 \\ 1 & 1 & ... & 1 & 0 \end{bmatrix}_{M \times N} ; \tag{59}$$

$$\Delta_2^{*4} = \begin{bmatrix} 0 & \lambda_2^{*4} & \lambda_2^{*4} & ... & \lambda_2^{*4} \\ \lambda_2^{*4} & 0 & \lambda_2^{*4} & ... & \lambda_2^{*4} \\ \lambda_2^{*4} & \lambda_2^{*4} & 0 & ... & ... \\ ... & ... & ... & ... & \lambda_2^{*4} \\ \lambda_2^{*4} & \lambda_2^{*4} & ... & \lambda_2^{*4} & 0 \end{bmatrix}_{MN \times MN} . \tag{60}$$

The presented model is much more complex than the one described in Chapter 4.3.4. Hence, more resonances are visible in the simulation outcome. The structure is modelled with the following parameters: Young's modulus $E = 200$ GPa, Poisson ratio $\nu = 0.33$, loss factor $\eta = 0.01$, steel density $\rho = 7850$ kg/m$^3$, cavity depth $H = 0.05$ m, thicknesses of the incident and radiating panel: $h_1 = 0.0006$ m and $h_2 = 0.0005$ m, respectively, and dimensions of each panel $a \times b = 0.42$ m $\times$ 0.42 m.

Figure 46 presents obtained simulation outcome along with the STL estimate from the experimental data obtained for zero activated couplings. Frequency range is 20–500 Hz (according to the properties of the microphones used — Chapter 2.3.2). There are three different curves in Fig. 46, each one for Young's modulus of a different type of steel at $T = 21$ °C. Such comparison is included to present the influence of $E$ value on STL model. As the manufacturers have different production processes and the exact parameters of a material may not always be known, slight adjustment of the parameters may be needed. As it is presented in Figure 46, model for $E = 200$ GPa reflects the real data in the best way when compared to other curves. However, the model is still too simplified to reflect the reality, as in the experimental data many additional dips and peaks are observed, and the levels of STL estimate based on the experimental data are different from the model outcome at most of the frequencies.

### 4.3.6. Sound Transmission Loss modeling by means of supervised machine learning techniques

Sound Transmission Loss analytical model for a finite double-panel structure presented in Chapter 4.3.5 differs from the STL estimate obtained experimentally, which is expected as there are many factors which influence acoustic performance of the structure in a real, complex laboratory environment. To better reflect STL

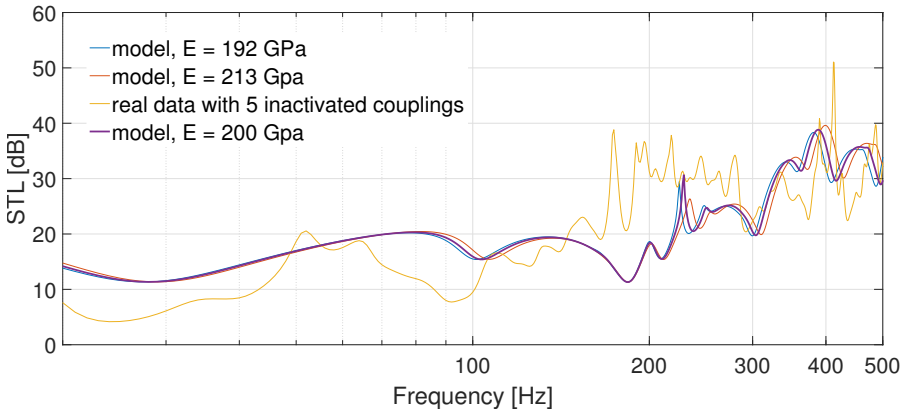


Figure 46: Estimate of Sound Transmission Loss for a finite clamped double-panel structure model compared to the estimate obtained for experimental data.

of a real structure, machine learning techniques may be applied to build a model and predict STL for a given frequency. The approach proposed below may be extended in the future research as the concept presented in this Chapter is a basic one, proposing a different approach to STL modeling by means of modern numerical libraries. Machine learning tasks can be divided into two main groups of regression and classification [148]. In this Chapter, regression models are discussed and applied.

For this task, a dataset was prepared with all STL estimates obtained from the experimental data included. Then, the prepared dataset was used to apply supervised machine learning to predict STL. Firstly, Ordinary Least Squares (OLS) model was selected. OLS model is used to predict values of a continuous response variable using one or more explanatory variables [149]. As there are strong linear relationships between the data in experimentally obtained dataset with STL model data appended, there is a need to identify independent variables properly before applying OLS model. Variance Inflation Factor (VIF) was calculated for independent variables to remove redundant features from further analysis.

All metrics' values given below are presented in the same way as the outputs from the numerical libraries used to implement the proposed models.

For OLS model applied, R-squared value equals 0.763. However, it has to be emphasized that R-squared value is not a good measure of model fit as it tends to increase along with adding another (possibly redundant) independent variables [149]. The comparison of real and predicted values of STL shows that a general trend of STL can be predicted based on two independent variables (Figure 47).

Akaike Information Criterion (AIC) value is high (equals 5572), what indicates that the proposed model should be improved.

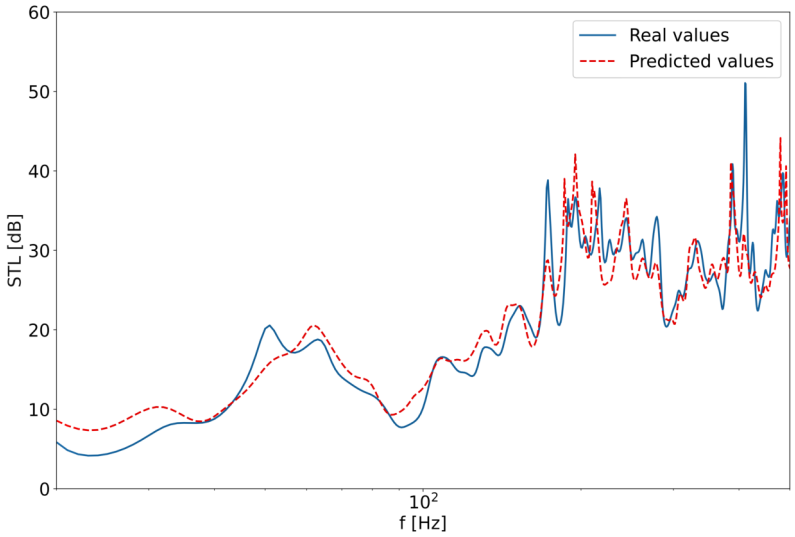


Figure 47: Comparison between OLS model prediction and experimental data.

Then, the decision tree model [150] was trained based on the whole dataset to compare the outcome with the previously presented model. The dataset was split into training set (70%) and testing set (30%). Cross-validation for different tree depth values in range 0–9 was done. It turned out that the error is the smallest for tree depth equal to 8. In such case, for training set R-Squared value was 0.9999999769220214, and for testing set R-squared value was 0.8968982424862689. In general, tree depth values equal to or greater than 4 resulted in similar accuracy, which means the model becomes robust for tree depth $\geq 4$.

As the tree depth was set to 8, the following metrics for the testing set were obtained:

- R-squared value: 0.8890371755320925,
- Mean Absolute Error (MAE): 1.5197663117528004,
- Mean Squared Error (MSE): 6.601427356857323,
- Root Mean Squared Error (RMSE): 2.5693242996666115.

These metrics' values indicate a good fit of the model. Figure 48a presents the comparison between decision tree regression model prediction and real data. The

differences are significantly lower than in case of OLS model. Hence, such approach would be applied to predict STL values based on large dataset of experimental data.

Then, to check robustness of the proposed model, dataset was split into training set (30%) and testing set (70%). The model was still able to predict STL values with good R-squared values (training set R-squared = 0.9868598802786707, testing set R-squared = 0.780075720519078) and low error values for testing set (MAE: 2.2341591378386223, MSE: 14.46936667060425, RMSE: 3.803862073025815). Figure 48b presents the comparison between decision tree regression model prediction and real data.

Another approach to model STL based on experimental data may be the Random Forest regression which is less vulnerable to overfitting problem than the previously described decision tree regression [151]. Hyperparameter tuning was done to optimize the obtained random forest model, e.g. optimized number of trees in the forest was 400, and the whole dataset was used to build each tree.

Dataset was divided into 70% training set and 30% testing set in the first approach. The following metrics for the testing set were obtained:

- R-squared value: 0.966973948057074,
- Mean Absolute Error (MAE): 0.7804733335227008,
- Mean Squared Error (MSE): 2.0254687807622265,
- Root Mean Squared Error (RMSE): 1.423189650314471.

Figure 49a presents the comparison between random forest model prediction and real data from 30% testing set. Overall good fit of the model is visible.

Dataset was divided into 30% training set and 70% testing set in the second approach. The following metrics for the testing set were obtained:

- R-squared value: 0.9286112075033099,
- Mean Absolute Error (MAE): 1.3644592694610869,
- Mean Squared Error (MSE): 4.569454700762005,
- Root Mean Squared Error (RMSE): 2.137628288726084.

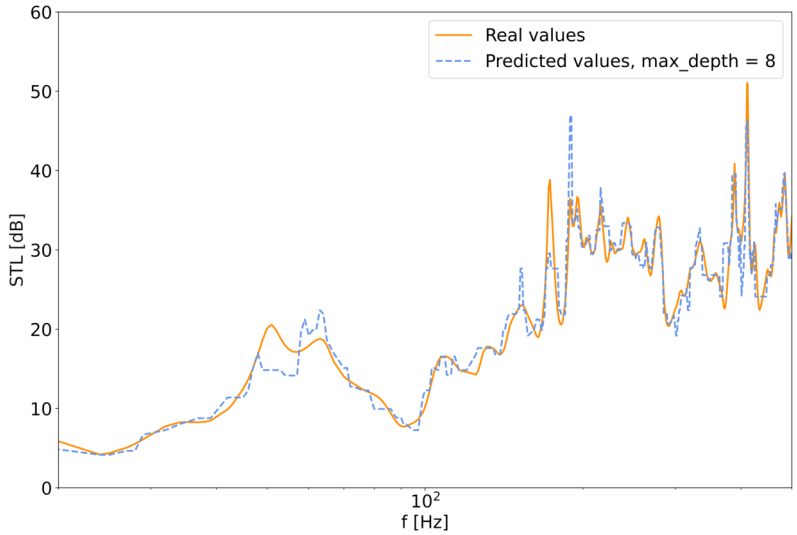


(a)

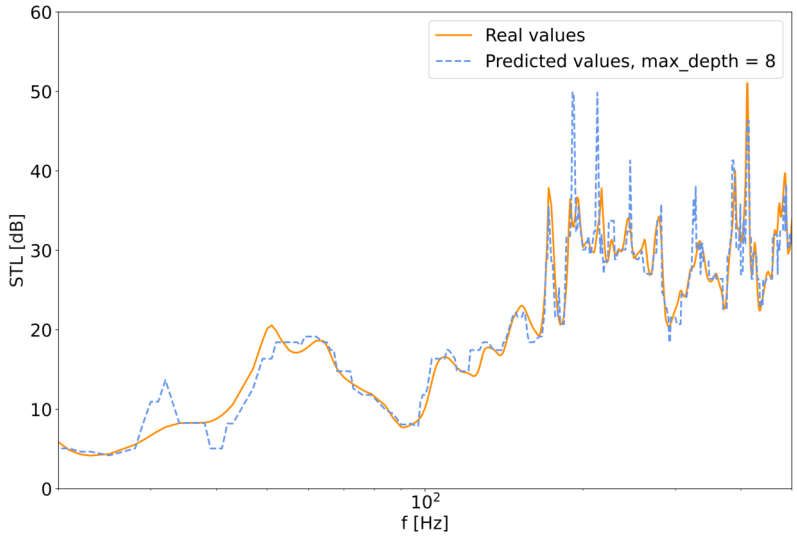


(b)

Figure 48: (a) Comparison between decision tree regression model prediction and real data for 70% training set and 30% testing set. (b) Comparison between decision tree regression model prediction and real data for 30% training set and 70% testing set.

Figure 49b presents the comparison between random forest model prediction and real data from 70% testing set. Overall fit of the model is worse than in Figure 49a, but still better than in cases of linear regression and decision tree regression, because it is able to predict not only most of the dips and peaks in STL curve, but also STL levels in the whole frequency band.

The presented metrics indicate that random forest approach is better than de-

cision tree regression and may result in a good fit between real data and model predictions.

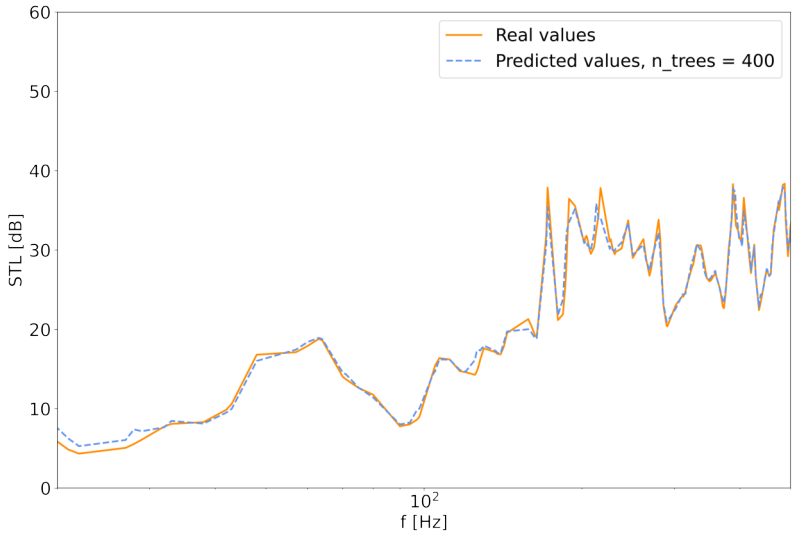


(a)

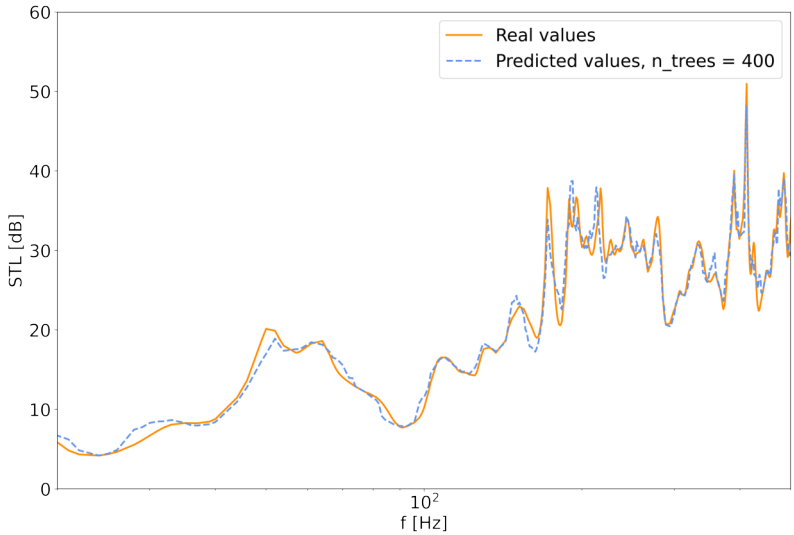


(b)

Figure 49: (a) Comparison between random forest model prediction and real data for 30% training set and 70% testing set. (b) Comparison between random forest model prediction and real data for 30% training set and 70% testing set.

## 4.4. Vibroacoustic properties of a modified double-panel structure

### 4.4.1. Vibroacoustic analysis for setup with one solenoid between the panels of the double-panel structure

By means of the experimental setup described in Chapter 4.2, a vibroacoustic analysis of a modified double-panel structure was performed [39]. The research described in the following Chapter was also published in [39] and the following analysis contains the novel description of the results as well as extends the topic.

Grid of measurements used in this research included 49 points on the radiating panel, where vibration were measured. Low grid resolution did not allow to observe modes higher than (3, 3) due to technical limitations of the system [39]. Figure 50 presents a comparison of magnitude spectra obtained for a central solenoid turned off and on, in the central point of the radiating panel [39]. The frequency range is 0–500 Hz. Green line represents a scenario of solenoid turned off, and blue line represents a scenario of solenoid turned on, with voltage equal to 11 V applied to the coil.

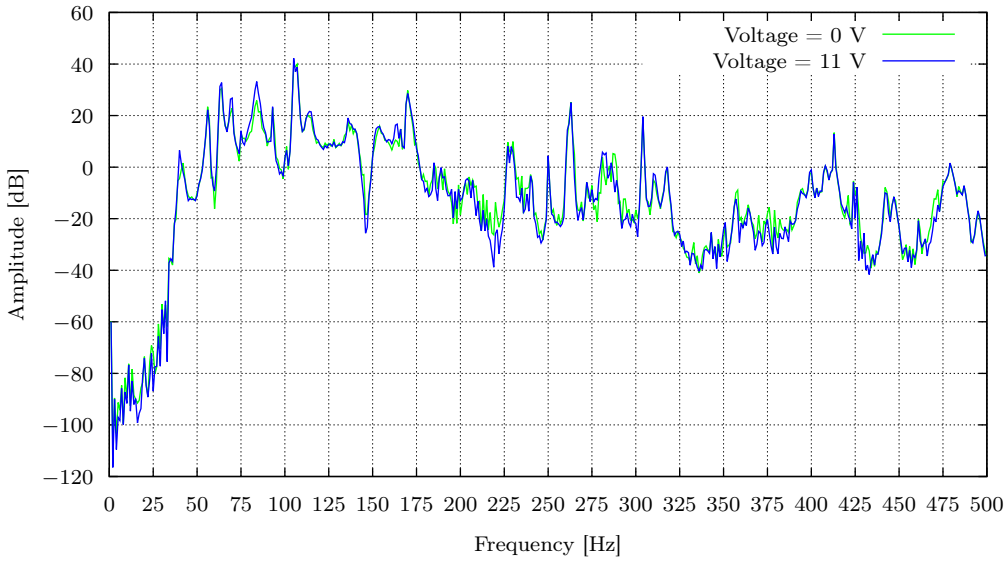


Figure 50: Comparison of magnitude spectra obtained for a central solenoid turned off and on, in the central point of the radiating panel, based on [39].

If the solenoid is unpowered, the magnitude spectrum curve is of higher levels at some of the frequencies, e.g. 200–225 Hz and 365–390 Hz. Turning the solenoid on

does not force the resonant frequencies to shift. Below 175 Hz, the curves are similar to each other and the influence of solenoid activation is weaker than for the higher frequencies. There are many resonances in the graph, hence additional graphical analysis of the modeshapes was included to ensure which of the peaks are related to modes (1, 1), (2, 2) and (3, 3). Based on the comparison, it turned out that frequencies of modes (2, 2) and (3, 3) were observed at about 93 Hz and 163 Hz, respectively, and shape of (1, 1) mode was observed at 30 Hz [39]. Figure 51 presents vibration patterns of these three modes. However, the peak at 30 Hz is not observed in Figure 50, which may be explained by the loudspeaker's ability to transmit noise above specific threshold. The first peak appears above 40 Hz. Slight irregularities of the modeshapes presented in Figure 51 may be explained by the fact that each of the point's vibrations were measured one by one, and not all at once — which may result in slight inaccuracy of the measurements if any conditions of the experiments slightly changed over time.

There are many other resonances observed in Figure 50, but their shapes are irregular and difficult to analyze. Modes (1, 1), (2, 2) and (3, 3) are characterized by regular shapes in case of both single panels and double-panel structures. As the grid dimensions is 7×7, which are the odd numbers, the antinodes of these modes are expected to appear around the grid points [39]. To support these observations, Figure 52 presents shapes obtained for first six peaks observed in Figure 50, i.e. 42 Hz, 56 Hz, 64 Hz, 70 Hz, 83 Hz and 93 Hz. In Figure 52c, shape similar to that of (2, 1) mode is observed. However, in case of isotropic square panel such mode cannot be distinguished from (1, 2) mode. In Figure 52f, shape of (2, 2) mode is observed.

Figure 53a presents a comparison of vibration amplitude for the radiating panel, averaged over its surface, in the scenarios of solenoid turned off, and solenoid supplied with voltage [39]. Green line represents the scenario with solenoid turned off, and blue line represents the scenario with solenoid turned on. Below 175 Hz and above 390 Hz, there are only small differences between both curves, which indicates that turning on the solenoid impacts the middle frequencies in the considered range if there is only one coupling between the panels of the double-panel structure. Figure 53b presents the difference between lines from Figure 53a (green one minus blue

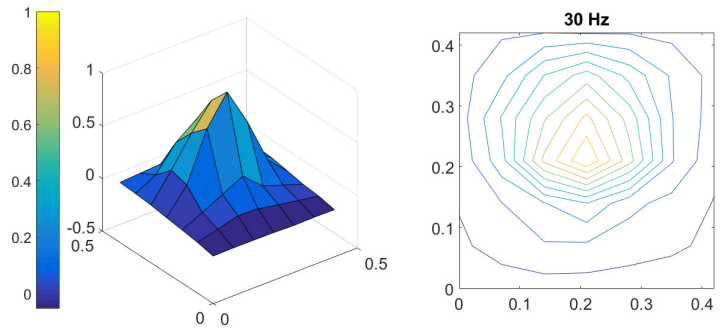


(a) 30 Hz.

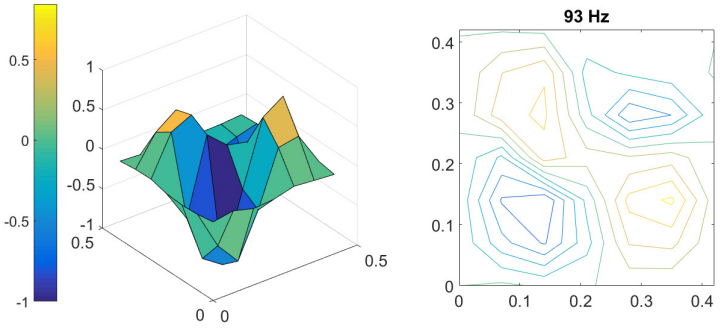


(b) 93 Hz.

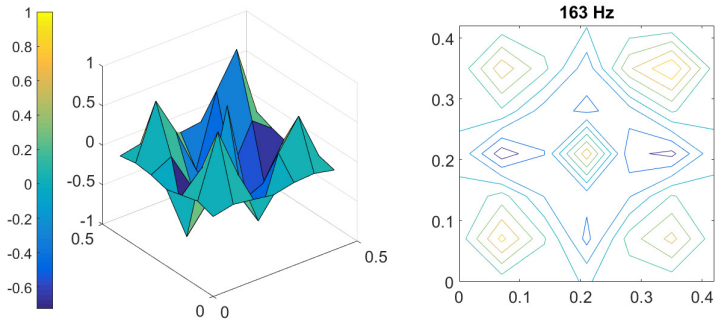


(c) 163 Hz.

Figure 51: Modes (1, 1), (2, 2) and (3, 3).

one) [39]. Values $\geq 0$ represent frequencies where vibration reduction on the radiating panel is observed, and its exact value is presented. Vibrations are reduced on the whole surface of the radiating panel mostly by up to 5 dB. At several frequencies, the difference exceeds 5 dB. Two biggest positive values are observed at 25 Hz and 427 Hz [39], where vibration are reduced by more than 5 dB. However, bands where the difference is a positive value are more relevant, as they indicate that vibrations on the radiating panel are reduced over a frequency band, and not only at the par-

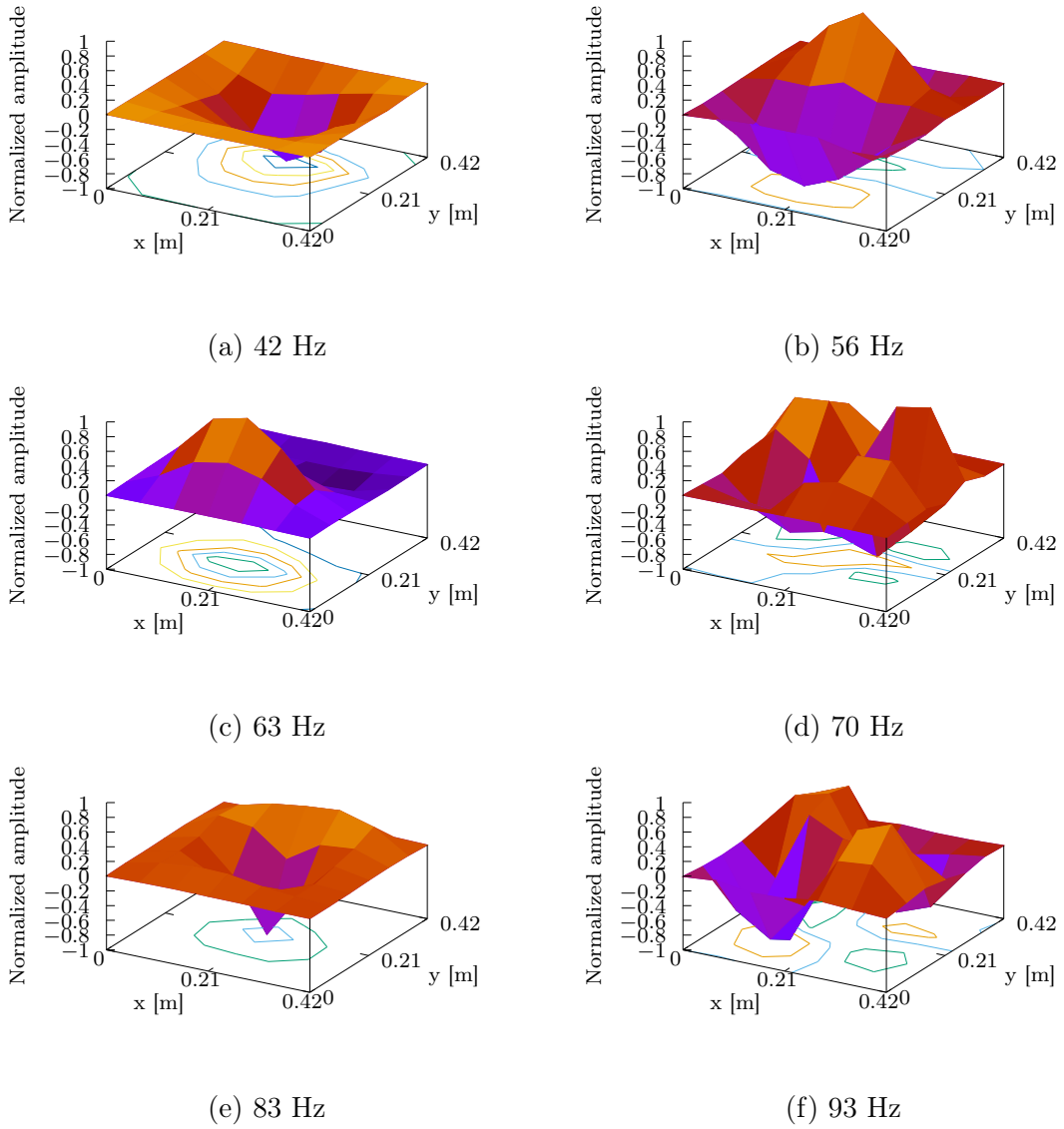


(a) 42 Hz

(b) 56 Hz

(c) 63 Hz

(d) 70 Hz

(e) 83 Hz

(f) 93 Hz

Figure 52: Shapes obtained for first six peaks, i.e. (a) 42 Hz, (b) 56 Hz, (c) 64 Hz, (d) 70 Hz, (e) 83 Hz and (f) 93 Hz. Partially based on [39].

ticular frequencies. Such frequency band is observed e.g. around 210–230 Hz. This is the widest one observed.

Figure 54 presents mode (1, 1) shapes obtained differently [39]. Figure 54a shows a simulated modeshape of an ideal isotropic thin steel panel. Figure 54b is a modeshape measured with the use of laser vibrometer, in case of voltage equal to 0 V (unpowered solenoid). Figure 54c is a modeshape measured with the use of laser vibrometer, in case of voltage equal to 11 V (solenoid turned on). There are no significant differences between the obtained vibration patterns and the impact of

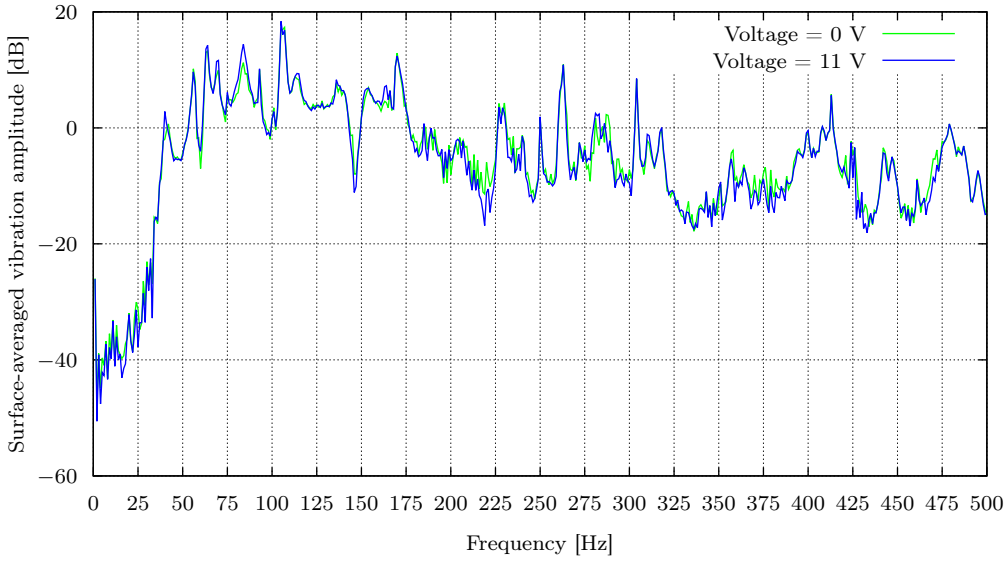


(a)

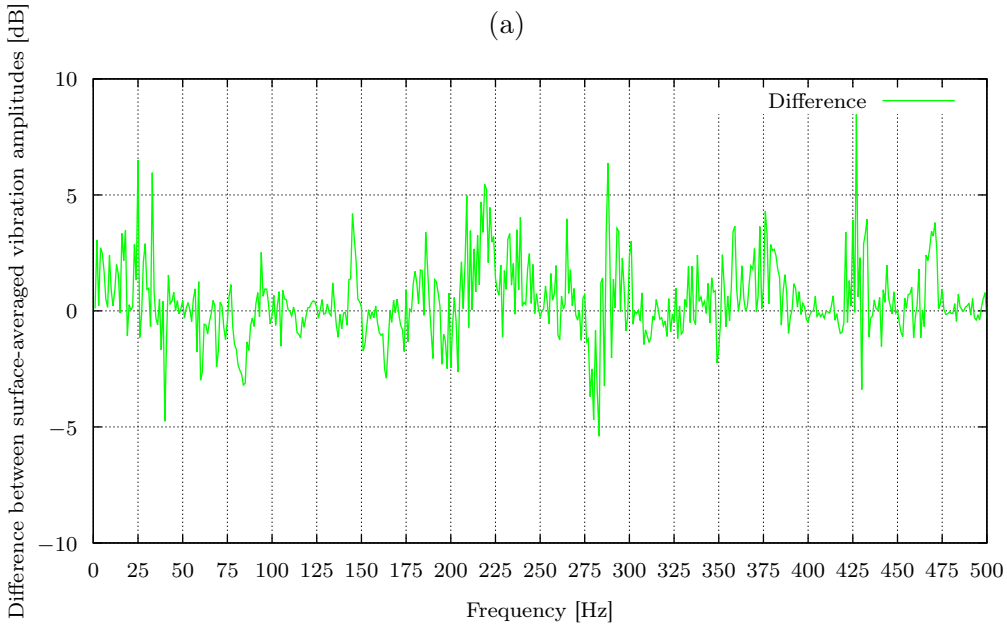


(b)

Figure 53: Figure based on [39]. (a) Comparison of surface-averaged vibration amplitude for the radiating panel in the scenarios of unpowered solenoid, and solenoid supplied with a voltage equal to 11 V. (b) Difference between surface-averaged vibration amplitude lines presented in (a).

turning on the solenoid is not visible.

Figure 55 presents mode (2, 2) shapes obtained differently [39]. Figure 55a shows a simulated modeshape of an ideal isotropic thin steel panel. Figure 55b is a modeshape measured with the use of laser vibrometer, in case of voltage equal

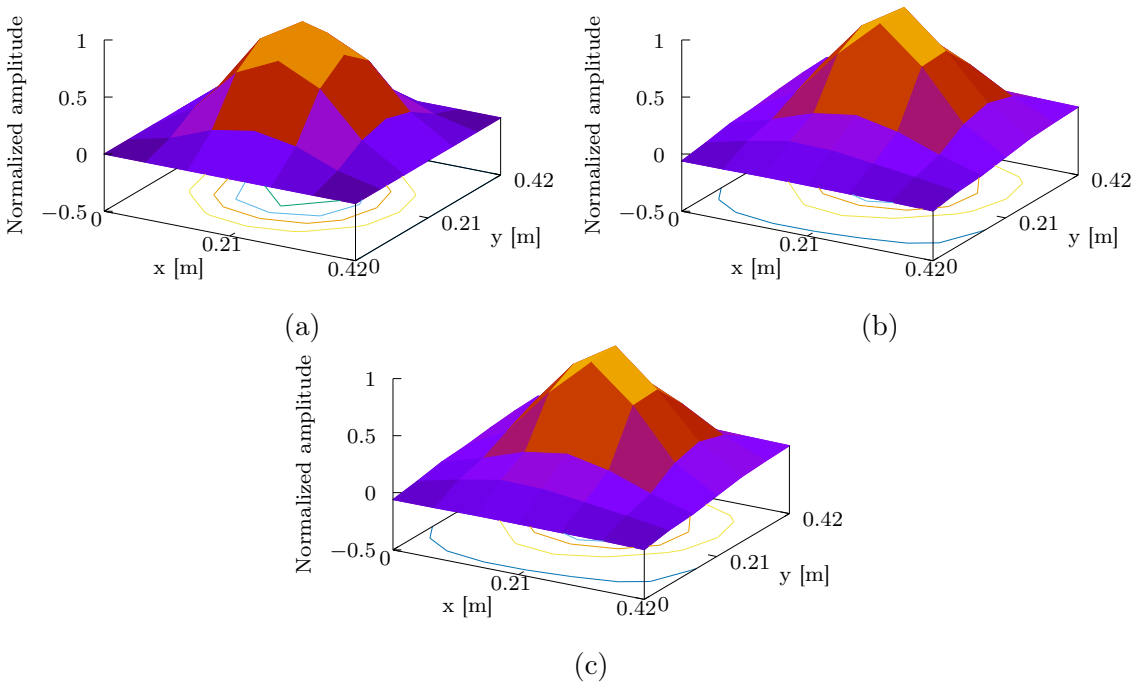


Figure 54: Comparison of mode (1, 1) shapes. (a) Simulated isotropic thin steel panel. (b) Modeshape measured at the voltage 0 V. (c) Modeshape measured at the voltage 11 V. Figure from [39]

to 0 V (unpowered solenoid). Figure 55c is a modeshape measured with the use of laser vibrometer, in case of voltage equal to 11 V (solenoid turned on). There are no significant differences between the obtained vibration patterns and the impact of turning on the solenoid is not visible.

Figure 56 presents mode (3, 3) shapes obtained differently [39]. Figure 56a shows a simulated modeshape of an ideal isotropic thin steel panel. Figure 56b is a modeshape measured with the use of laser vibrometer, in case of voltage equal to 0 V (unpowered solenoid). For this scenario, surface-averaged vibration amplitude for the radiating panel is equal to 4.56 dB [39]. Figure 56c is a modeshape measured with the use of laser vibrometer, in case of voltage equal to 11 V (solenoid turned on). For this scenario, surface-averaged vibration amplitude for the radiating panel is equal to 7.07 dB [39]. Although in Figure 56c the amplitude of the central peak on the radiating panel is slightly lower than in Figure 56b, the overall effect of turning on the solenoid (measured by surface-averaged vibration amplitude) is negative, as the vibrations of the radiating panel generally increase after turning the solenoid

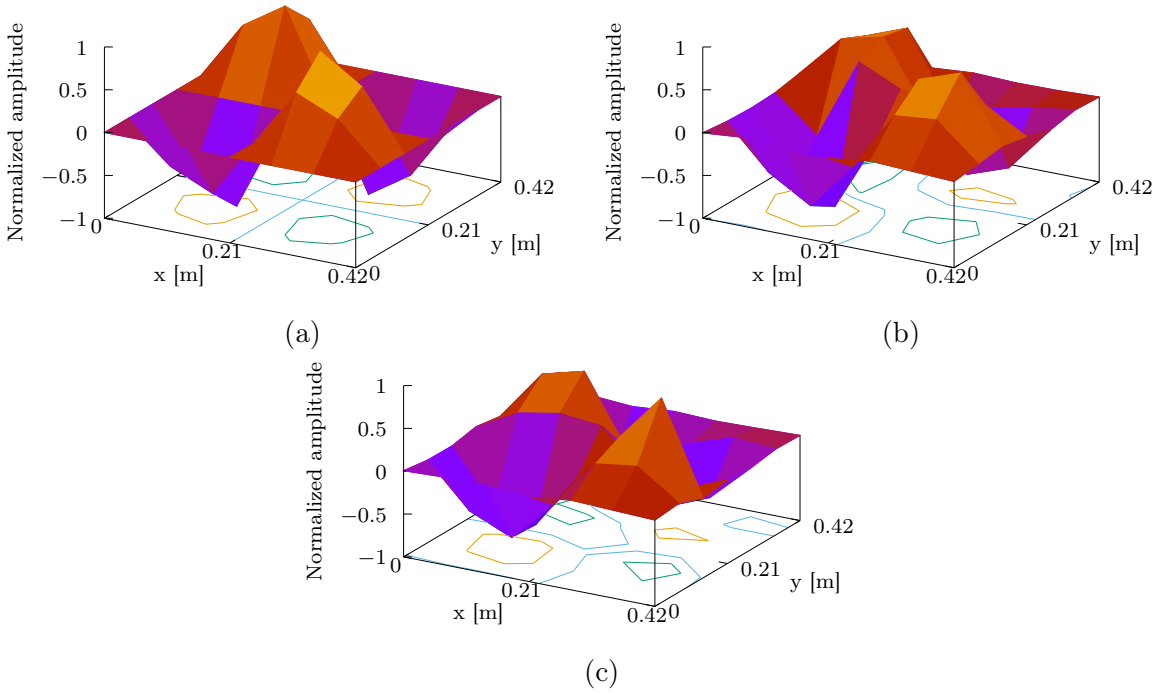


Figure 55: Comparison of mode (2, 2) shapes. (a) Simulated isotropic thin steel panel. (b) Modeshape measured at the voltage 0 V. (c) Modeshape measured at the voltage 11 V. Figure from [39].

on. Probably, one solenoid is not enough to prevent vibration energy transmission to different areas of the radiating panel, when the solenoid is on.

It is noteworthy that the use of solenoid caused the noticeable change of the radiating panel's vibroacoustic properties in general, having both positive and negative impact depending on the frequency. As it is shown in Figure 53b, for most of the frequencies in range 0–500 Hz the beneficial effect of turning the solenoid on is noticeable. However, these effects are not observed for the modes analyzed above, and such effect is not satisfactory, as the central peaks observed in modes (1, 1) and (3, 3) are not significantly reduced, and the vibrations are enhanced elsewhere on the radiating panel. Table 13 presents percentages of the frequency range 0–500 Hz, where the difference from Figure 53b is within a specified range.

For more than 57% of the considered frequencies, vibration reduction is observed in the range $(0, 5]$ dB. Only for 1.2% of the frequencies, reduction is higher than 5 dB. The surface-averaged vibration amplitude of the radiating panel increases for 41.4% of the frequencies if the solenoid is turned on. Such effect may be expected as

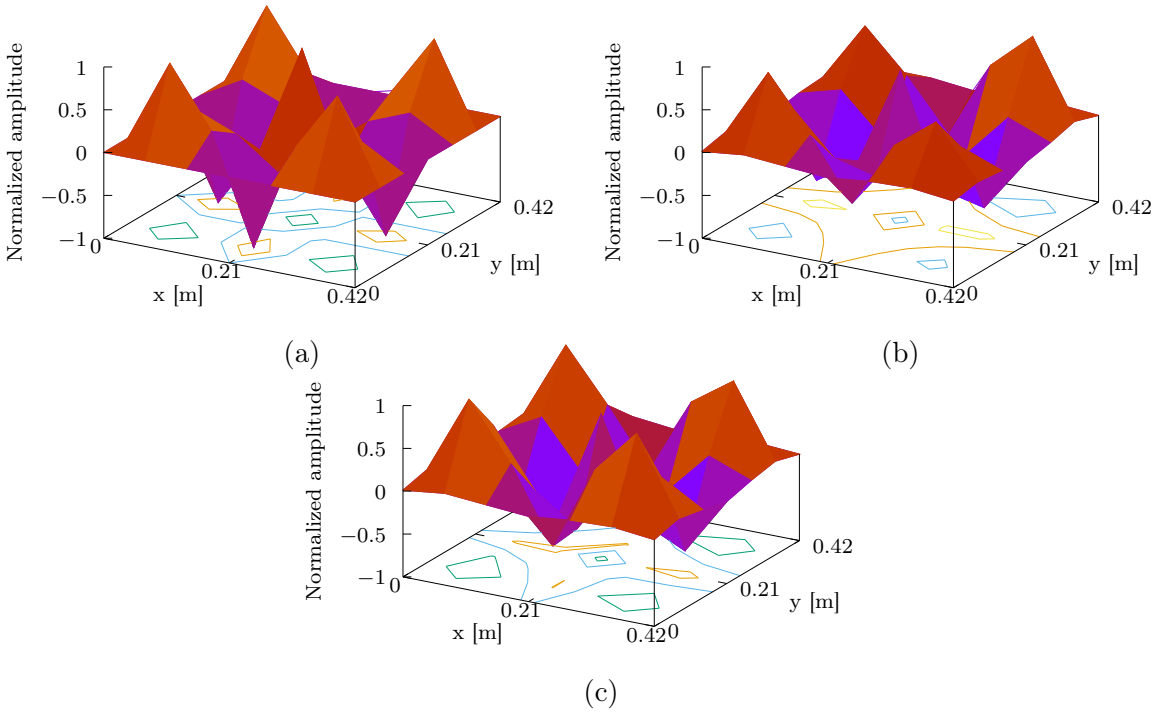


Figure 56: Comparison of mode (3, 3) shapes. (a) Simulated isotropic thin steel panel. (b) Modeshape measured at the voltage 0 V. (c) Modeshape measured at the voltage 11 V. Figure from [39].

Table 13: Percentages of the frequency range 0–500 Hz, where the difference from Figure 53b is within a specific range.

| % of frequencies | Difference value range [dB] |
|---|---|
| 1.2 | $> 5$ |
| 57.4 | $(0, 5]$ |
| 0 | $= 0$ |
| 41.4 | $< 0$ |

one coupling located between the panels' centres may cause vibration transfer to different areas of the radiating panel at the specific resonances, leading to a local increase of vibration.

### 4.4.2. Vibroacoustic analysis for setup with five solenoids between the panels of the double-panel structure: RMS

The research described in the following Chapter was also published in [96], and the following analysis applies to the same experiments, but presents also a novel

and extended description of the results. The research experiment was performed to examine an influence of the couplings on the radiating panel vibrations. The loudspeaker placed inside the rigid casing emitted broadband noise up to 500 Hz. MFC elements glued to the radiating panel were used to measure vibration. Couplings were supplied with voltage signal modulated by means of PWM method, with varying duty cycle values.

Vibrations were measured with sampling frequency of 20 kHz, and data acquired from MFC elements were collected as 20k-samples-long vectors, averaged from all series of measurements [96]. Root Mean Square (RMS) levels were computed from all vectors based on the following equation [96]:

$$x_{\mathrm{RMS}} = \sqrt{\frac{1}{N}\sum_{n=1}^{N} x_n^2}. \tag{61}$$

The duty cycle values varied from 0% to 99%. Table 14 presents calculated RMS levels of MFC signals if only one (central) coupling was activated [96]. If a central coupling is activated, RMS level is increased around each MFC element, and if duty cycle is further increased to 50%, a slight decrease of RMS level is observed around three of the MFCs, no. 1, 2 and 5 [96]. Activation of the coupling has a stronger impact on panel vibrations if duty cycle increases from zero to non-zero value, then if it is further increased [96]. If the duty cycle is equal to 99%, only the RMS level calculated for central MFC element decreases significantly in comparison to the other ones. Vibrations of the central panel area may be reduced if duty cycle is set to 99%. Setup with lower values of duty cycle does not provide such effect.

Table 14: RMS levels calculated for MFC signals. 1 (central) coupling activated [96].

| no. of activated couplings, duty cycle | MFC1: RMS [V] | MFC2: RMS [V] | MFC3: RMS [V] | MFC4: RMS [V] | MFC5: RMS [V] |
|---|---|---|---|---|---|
| 0C, 0% | 0.1024 | 0.0975 | 0.1671 | 0.1038 | 0.1136 |
| 1C, 25% | 0.1052 | 0.0979 | 0.1698 | 0.1076 | 0.1150 |
| 1C, 50% | 0.1047 | 0.0973 | 0.1743 | 0.1103 | 0.1079 |
| 1C, 75% | 0.1102 | 0.1014 | 0.1708 | 0.1085 | 0.1142 |
| 1C, 99% | 0.1107 | 0.0884 | 0.1124 | 0.0901 | 0.1097 |

Table 15 presents RMS levels calculated for MFC signals in case of four couplings

(no. 1, 2, 4 and 5) activated [96]. As only the corner couplings are activated, the central solenoid is not supplied with voltage. As previously stated, an increase of duty cycle to 99% leads to vibration reduction in the central area of the panel (Table 14). However, in case of four couplings activated, an opposite effect is observed, and panel vibrations increase in the central area. Such behaviour may be explained by vibration energy transfer to the panel's centre while the other areas are stiffened due to the activation of corner couplings [96]. Boundary conditions of the panels are assumed to be fully clamped, hence the central area of the panel vibrates the most. Thus, it may be more beneficial to stiffen this area instead of activating the solenoids around the panel corners [96]. The vibration energy is then transmitted towards the panel edges, whose vibrations are limited due to the provided boundary conditions.

Table 15: RMS levels calculated for MFC signals. 4 couplings activated (no. 1, 2, 4, 5) [96].

| no. of activated couplings, duty cycle | MFC1: RMS [V] | MFC2: RMS [V] | MFC3: RMS [V] | MFC4: RMS [V] | MFC5: RMS [V] |
|---|---|---|---|---|---|
| 0C, 0% | 0.1024 | 0.0975 | 0.1671 | 0.1038 | 0.1136 |
| 4C, 25% | 0.1088 | 0.1003 | 0.1954 | 0.1017 | 0.1058 |
| 4C, 50% | 0.1099 | 0.0925 | 0.1717 | 0.0934 | 0.0996 |
| 4C, 75% | 0.1033 | 0.0982 | 0.1783 | 0.0993 | 0.0957 |
| 4C, 99% | 0.1098 | 0.0910 | 0.2047 | 0.0910 | 0.0991 |

Table 16 presents RMS levels calculated for MFC signals in case of five couplings (no. 1, 2, 3, 4 and 5) activated [96]. If duty cycle is increased from 25% to 50%, vibration in all five areas increase. This indicates a phenomenon of transferring vibration from the incident panel to the radiating panel through indirectly stiffened solenoids [96]. Duty cycle has to be set to 99% to observe a decrease of vibration on the whole radiating panel. The highest reduction of vibrations is observed in the central area of the panel. Vibration reduction around the MFC elements no. 2, 4 and 5 is smaller in comparison to the central element, and at the element no. 1 it is negligible. Such effect would not be observed if the solenoids would be mounted in an ideally regular manner and the boundary conditions would be perfect fully clamped. However, it is not possible to achieve an ideal accuracy of the solenoids'

assembly in the experimental setup, as all of the solenoid cores would have to be positioned inside the corresponding coils with the same accuracy. As the accuracy of solenoids' assembly slightly differs along the double-panel structure, vibration reduction is not regular due to the differences in the induced electromotive forces [96]. There is also a risk of the panels' asymmetry resulting from the manufacturing process, which may influence the structure's vibroacoustic properties [96].

Table 16: RMS levels calculated for MFC signals. 5 couplings activated [96].

| no. of activated couplings, duty cycle | MFC1: RMS [V] | MFC2: RMS [V] | MFC3: RMS [V] | MFC4: RMS [V] | MFC5: RMS [V] |
|---|---|---|---|---|---|
| 0C, 0% | 0.1024 | 0.0975 | 0.1671 | 0.1038 | 0.1136 |
| 5C, 25% | 0.1273 | 0.1129 | 0.1704 | 0.1203 | 0.1351 |
| 5C, 50% | 0.1293 | 0.1431 | 0.1981 | 0.1544 | 0.1368 |
| 5C, 75% | 0.1222 | 0.1092 | 0.1630 | 0.1238 | 0.1233 |
| 5C, 99% | 0.1287 | 0.1087 | 0.1353 | 0.1052 | 0.1115 |

Figure 57 presents signals acquired by (central) MFC element no. 3 in cases of 0, 1, 4 and 5 couplings activated, respectively [96]. Duty cycle was set to 99% in all cases. RMS level was calculated for each signal and plotted as a horizontal line on each graph.

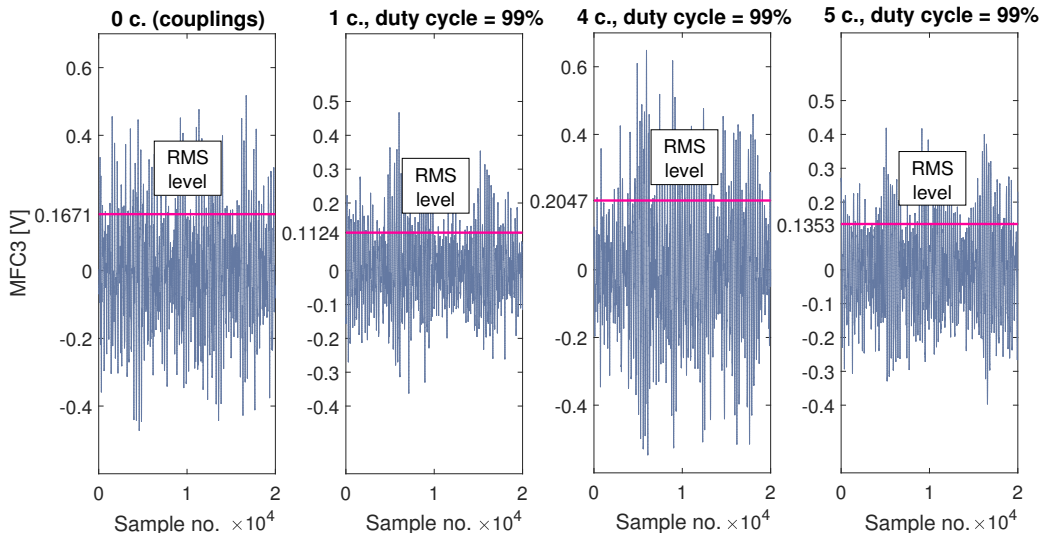


Figure 57: MFC signals acquired by central MFC element in cases of 0, 1, 4 and 5 couplings activated, respectively. Duty cycle = 99%. Adapted from [96].

If the duty cycle of a PWM signal is set to 99%, differences between RMS levels

obtained for the selected cases are observed. The lowest RMS level is observed if only the central coupling is activated, and if the other couplings are also activated, then RMS level increases, which implies an increase of vibration as well [96]. If the solenoids act as the mass loadings only (case of 0 activated couplings), it is a more beneficial setup in terms of RMS level reduction than to activate the solenoids in the corners [96].

### 4.4.3. Spectral analysis for setup with five solenoids between the panels of the double-panel structure

The results from the experiments described in the following Chapter were also published in [81], and the following analyses contain the novel description of these results as well as extend the topic. In the experiment dedicated to spectral analysis of MFC-measured vibration of the double-panel structure coupled with solenoids, data were acquired as the 560000-samples-long vectors [81]. Each vector contained 28 series of measurements. Then, 20000 samples were deleted from each vector's beginning and then vectors were averaged [81]. Finally, after all preliminary data processing operations, each vector had 20000 samples [81]. As the spectral analysis was conducted, processed data were transformed into frequency domain [81]. MFCs are numbered from 1 to 5, as in Fig. 42.

Data are presented as Power Spectral Density (PSD) estimates of MFC input signals. Welch method with sampling rate equal to 20 kHz was applied. The other parameters were: Hanning window length = 5000, number of overlapped samples = 0, and expected spectral resolution = 1 Hz [81]. In the analysis provided below, Figures 58–62 [81] present PSD estimates obtained for different numbers of activated couplings, including the reference scenario, where none of the solenoids were supplied with voltage, and they acted as the mass loadings only. The frequency range is up to 500 Hz. In each of these Figures, influence of varying duty cycle value on PDS estimates is shown.

Tables 17–21 [81] show the most efficient values of duty cycle for each considered scenario. In these Tables, efficiency factor is defined as a percentage of frequencies in range 0:1:500 Hz, where a selected duty cycle value corresponds to the lowest level of PSD estimate [81]. Efficiency factor is determined separately for different

numbers of activated couplings, taking into account duty cycle value varying from 25% to 99%. Reference scenario (0 activated couplings) is included, because at some of the frequencies it may be more beneficial not to supply the solenoids with voltage in terms of vibration reduction. Hence, five different scenarios are analyzed, and efficiency factor values calculated for them should sum up to 100%. The maximal value of efficiency factor in each of the Tables is in boldface.

Figures 58–62 correspond to Tables 17–21. Light-green areas below PSD estimates' curves in each Figure emphasize where the maximal efficiency factor value was obtained, and for which scenario. Figure 58 presents PSD estimates of MFC1 input signals [81]. Figure 58a shows a scenario of 1 (central) coupling activated. Figure 58b shows a scenario of 4 couplings activated. Figure 58c shows a scenario of 5 couplings activated. Duty cycle values are: 25%, 50%, 75%, and 99%. The reference scenario is included in all of the Figures. Figures 58a–58b present slightly lower PSD estimates' levels than Figure 58c, but in the latter case, the widest frequency band of vibration reduction is observed, e.g. around 100 Hz and over 150 Hz, for duty cycle equal to 99%. Similar effect is observed in Figure 58b. It has to be emphasized that still at many frequencies setting duty cycle to 99% does not imply vibration reduction, which leads to a conclusion that performance of coupling point no. 1 depends on: noise frequency, other couplings, and varying duty cycle of PWM signal [81]. Coupling's weak performance, measured by MFC1, may also indicate wrong solenoid placement between the panels [81].

Table 17 presents efficiency factors calculated for the case of MFC1 measured vibration [81]. The values in boldface indicate that the most efficient duty cycle value is 99%. The efficiency factor increases for the cases of 4 or 5 couplings activated. For the reference scenario, efficiency factor value is always more than 20%, which confirms the previous observation that coupling no. 1 may not be placed in optimal position [81].

Figure 59 presents PSD estimates of MFC2 input signals [81]. Figure 59a shows a scenario of 1 (central) coupling activated. Figure 59b shows a scenario of 4 couplings activated. Figure 59c shows a scenario of 5 couplings activated. Duty cycle values are: 25%, 50%, 75%, and 99%. The reference scenario is included in all of the Figures. The frequency ranges where vibration reduction is observed are wider

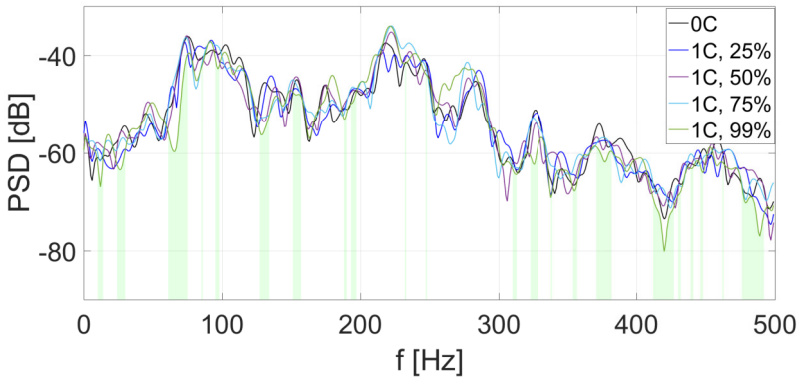


(a) 1 coupling activated.

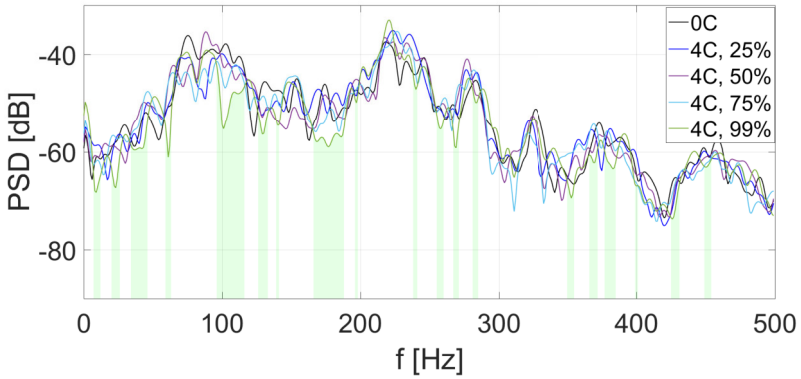


(b) 4 couplings activated.

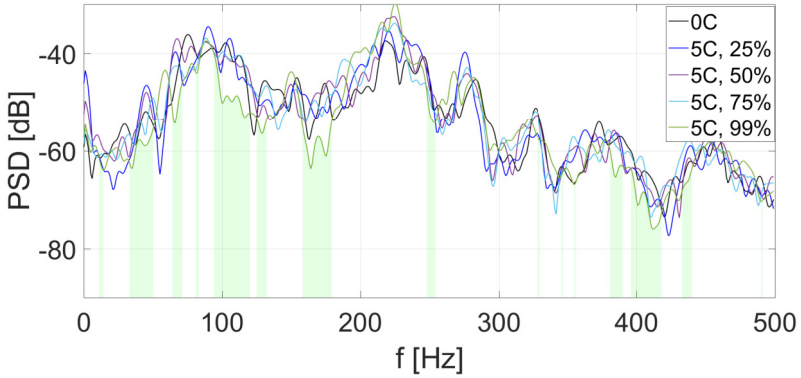


(c) 5 couplings activated.

Figure 58: Power Spectral Density estimates of MFC1 input signals [81].

and more frequent than in Figure 58. In Figures 59b–59c, the common range of 100–225 Hz is characterized by worse performance for duty cycle value set to 99%. In such case, lower duty cycle of the coupling gives better results [81].

Table 18 presents efficiency factors calculated for the case of MFC2 measured vibration [81]. Efficiency factor values in boldface are higher than in Table 17. For 4 or 5 activated couplings, the difference exceeds 10%. This indicates more efficient

Table 17: Efficiency factors calculated for the case of MFC1-measured vibration [81].

| **Number of activated couplings, duty cycle [%]** | **Efficiency factor [%]** |
|---|---|
| 0C | 22.2 |
| 1C, 25% | 19.4 |
| 1C, 50% | 16.0 |
| 1C, 75% | 15.0 |
| 1C, 99% | **27.4** |
| sum | 100 |
| 0C | 22.8 |
| 4C, 25% | 11.4 |
| 4C, 50% | 15.4 |
| 4C, 75% | 20.6 |
| 4C, 99% | **29.8** |
| sum | 100 |
| 0C | 25.8 |
| 5C, 25% | 19.4 |
| 5C, 50% | 9.4 |
| 5C, 75% | 15.6 |
| 5C, 99% | **29.8** |
| sum | 100 |

placement of coupling no. 2 in terms of vibration reduction. For one activated coupling, maximal efficiency factor value decreases. Hence, a presence of other stiffened couplings around coupling no. 2 increases its performance [81].

Figure 60 presents PSD estimates of MFC3 input signals [81]. Figure 60a shows a scenario of 1 (central) coupling activated. Figure 60b shows a scenario of 4 couplings activated. Figure 60c shows a scenario of 5 couplings activated. Duty cycle values are: 25%, 50%, 75%, and 99%. The reference scenario is included in all of the Figures. In all three Figures, a subrange 250–300 Hz of worse performance is observed if duty cycle is set to 99%. For duty cycle equal to 99%, it is better to activate only one couplings instead of 4 or 5 ones, because it leads to a higher vibration reduction in a wider frequency band. Stiffened couplings around the central one lower the overall performance of the structure, if the central coupling is also activated [81].

Table 19 presents efficiency factors calculated for the case of MFC3-measured

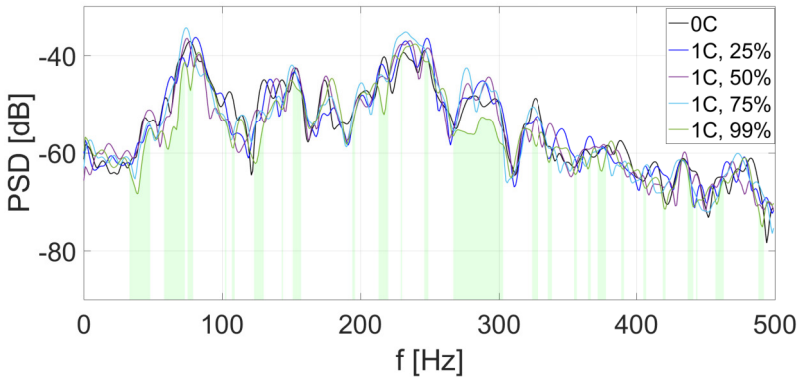


(a) 1 coupling activated.

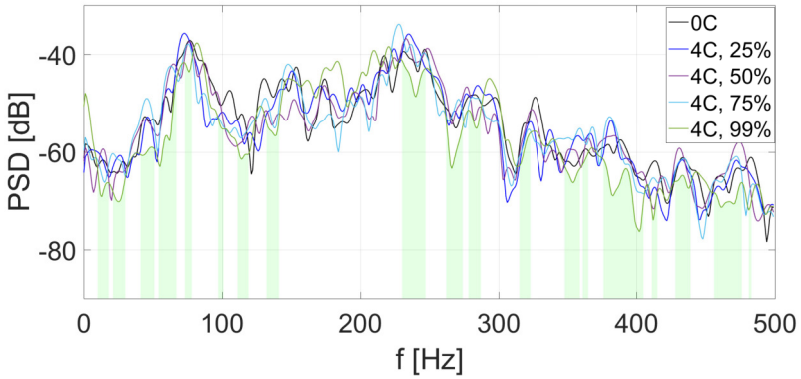


(b) 4 couplings activated.

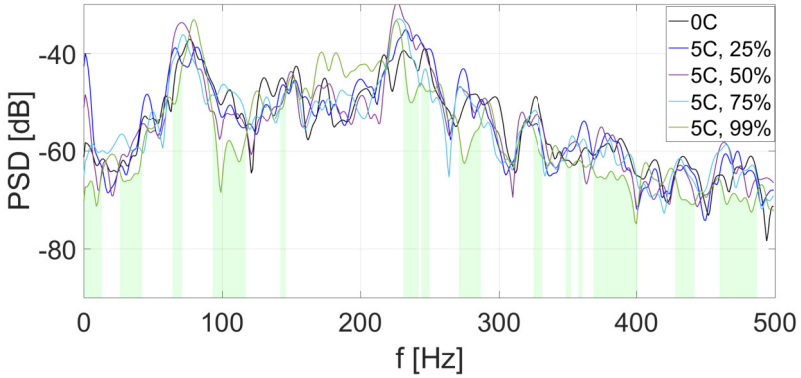


(c) 5 couplings activated.

Figure 59: Power Spectral Density estimates of MFC2 input signals [81].

vibration [81]. As it is observed based on Figure 60, the most efficient setup is to activate central coupling only, with duty cycle set to 99%. Then, for over 43% of the frequencies in the considered range, maximal vibration reduction is observed. If the central coupling is not activated in contrary to the other ones, overall performance of the structure deteriorates [81].

Figure 61 presents PSD estimates of MFC4 input signals [81]. Figure 61a shows

Table 18: Efficiency factors calculated for the case of MFC2-measured vibration [81].

| **Number of activated couplings, duty cycle [%]** | **Efficiency factor [%]** |
|---|---|
| 0C | 17.4 |
| 1C, 25% | 14.2 |
| 1C, 50% | 18.4 |
| 1C, 75% | 16.6 |
| 1C, 99% | **33.4** |
| sum | 100 |
| 0C | 11.0 |
| 4C, 25% | 14.4 |
| 4C, 50% | 16.2 |
| 4C, 75% | 16.0 |
| 4C, 99% | **42.4** |
| sum | 100 |
| 0C | 13.0 |
| 5C, 25% | 13.0 |
| 5C, 50% | 14.2 |
| 5C, 75% | 19.2 |
| 5C, 99% | **40.6** |
| sum | 100 |

a scenario of 1 (central) coupling activated. Figure 61b shows a scenario of 4 couplings activated. Figure 61c shows a scenario of 5 couplings activated. Duty cycle values are: 25%, 50%, 75%, and 99%. The reference scenario is included in all of the Figures. Figure 61a presents many narrow frequency bands of the best performance for duty cycle set to 99%. In this case, coupling no. 4 plays only a role of mass loading, and different coupling is stiffened. If coupling no. 4 is supplied with voltage of duty cycle equal to 99%, the overall performance of the structure deteriorates [81].

Table 20 presents efficiency factors calculated for the case of MFC4 measured vibration [81]. The Table confirms the observation that activating central coupling only with duty cycle set to 99% provided the best overall performance and vibration reduction at almost 45% of the frequencies in the considered range. If 4 or 5 couplings are activated, the performance is lower. However, efficiency factor values are above 30% [81].

Figure 62 presents PSD estimates of MFC5 input signals [81]. Figure 62a shows

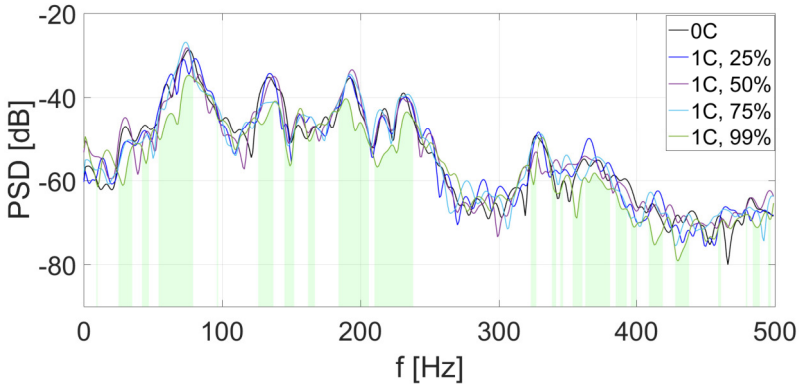


(a) 1 coupling activated.

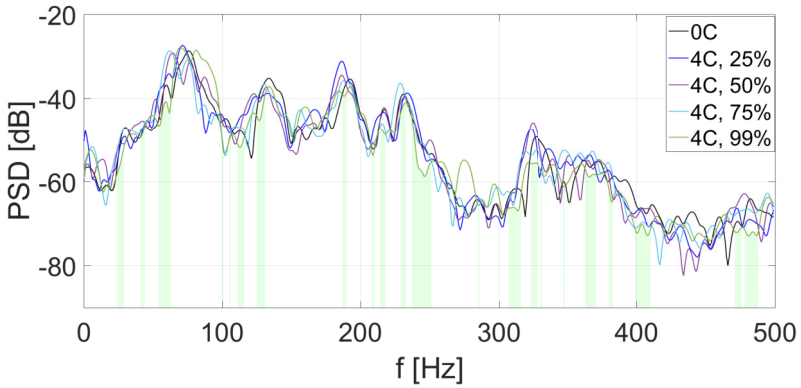


(b) 4 couplings activated.

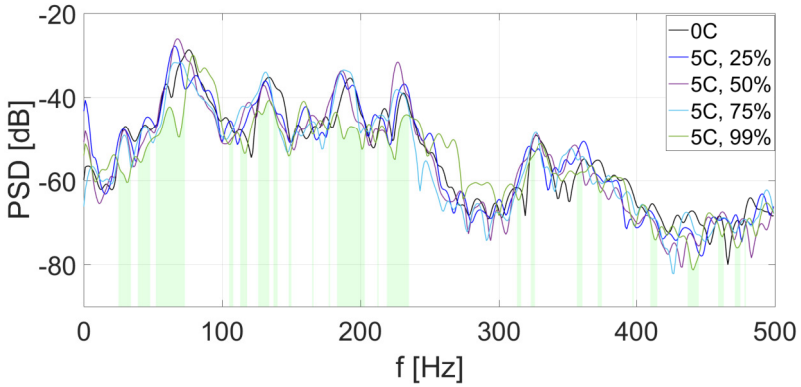


(c) 5 couplings activated.

Figure 60: Power Spectral Density estimates of MFC3 input signals [81].

a scenario of 1 (central) coupling activated. Figure 62b shows a scenario of 4 couplings activated. Figure 62c shows a scenario of 5 couplings activated. Duty cycle values are: 25%, 50%, 75%, and 99%. The reference scenario is included in all of the Figures. If duty cycle is set to 99%, the overall performance is lower than in the previously analyzed Figures. If 4 couplings are activated, the widest frequency bands of vibration reduction for a best scenario are observed. It is noteworthy that

Table 19: Efficiency factors calculated for the case of MFC3-measured vibration [81].

| **Number of activated couplings, duty cycle [%]** | **Efficiency factor [%]** |
|---|---|
| 0C | 19.2 |
| 1C, 25% | 13.6 |
| 1C, 50% | 12.6 |
| 1C, 75% | 11.4 |
| 1C, 99% | **43.2** |
| sum | 100 |
| 0C | 17.2 |
| 4C, 25% | 15.4 |
| 4C, 50% | 23.0 |
| 4C, 75% | 17.8 |
| 4C, 99% | **26.6** |
| sum | 100 |
| 0C | 12.4 |
| 5C, 25% | 12.0 |
| 5C, 50% | 22.6 |
| 5C, 75% | 21.0 |
| 5C, 99% | **32.0** |
| sum | 100 |

a lower duty cycle of PWM signal supplying the couplings may also be beneficial in selected setups. For 5 activated couplings, the best scenario is observed with duty cycle set to 75%, which is the only case where duty cycle $< 99\%$ provides the best result [81].

Table 21 presents efficiency factors calculated for the case of MFC5-measured vibration [81]. Maximal efficiency factor values are below 30%. If 4 couplings are activated, efficiency factor value increases if duty cycle value increases as well [81].

As for 14 of a total of 15 scenarios the best performance is achieved if duty cycle is set to 99%, additional comparison of efficiency factor values obtained for each coupling point with duty cycle equal to 99% is provided in Table 22 [81]. 2 of 3 efficiency factor values in boldface are obtained for coupling point no. 2, and one is related to coupling point no. 4. All efficiency factor values for these couplings are above 30%. These couplings are located on the same diagonal. The efficiency factor value for 1 activated coupling and duty cycle = 99% is also high, compared to

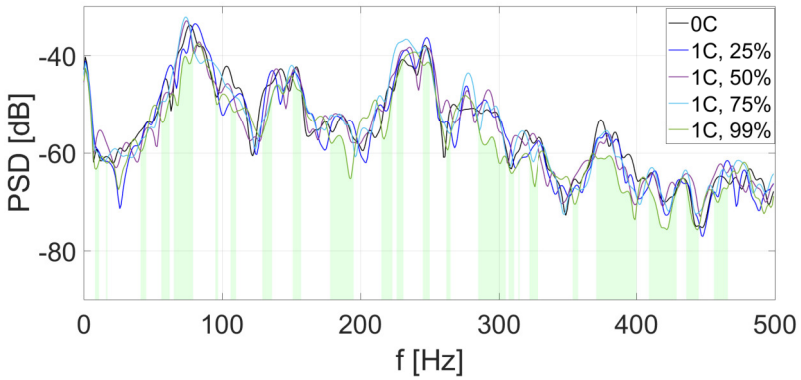


(a) 1 coupling activated.

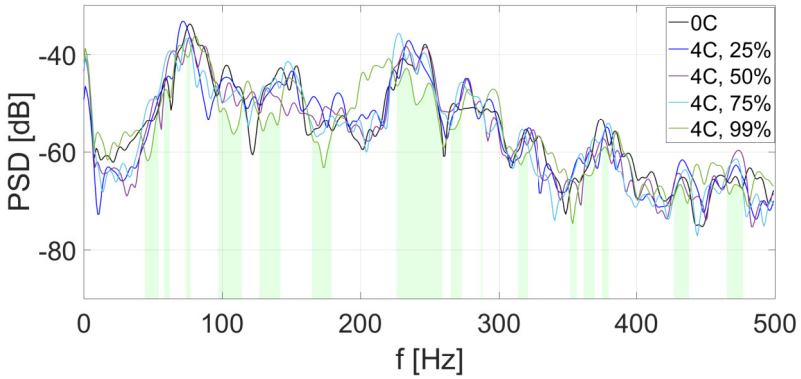


(b) 4 couplings activated.

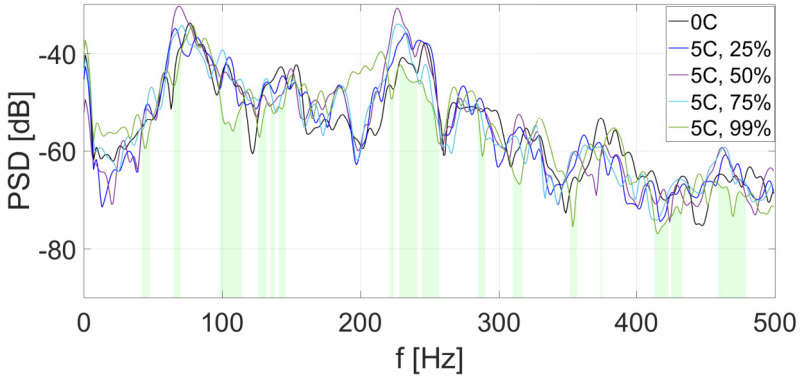


(c) 5 couplings activated.

Figure 61: Power Spectral Density estimates of MFC4 input signals [81].

other efficiency factor values in the Table. Column of average values indicates that such setup is the best in comparison to the others. For five activated couplings, the average value of efficiency factors is the lowest, which may be caused by suboptimal placements of some of the couplings and by the fact that one of efficiency factor values in this case is not a maximal one. Row of average values indicates that the overall performance for coupling points no. 2, 3 and 4 is better than for coupling

Table 20: Efficiency factors calculated for the case of MFC4-measured vibration [81].

| **Number of activated couplings, duty cycle [%]** | **Efficiency factor [%]** |
|---|---|
| 0C | 11.6 |
| 1C, 25% | 21.6 |
| 1C, 50% | 14.4 |
| 1C, 75% | 7.8 |
| 1C, 99% | **44.6** |
| sum | 100 |
| 0C | 14.2 |
| 4C, 25% | 12.6 |
| 4C, 50% | 17.6 |
| 4C, 75% | 21.8 |
| 4C, 99% | **33.8** |
| sum | 100 |
| 0C | 21.2 |
| 5C, 25% | 18.8 |
| 5C, 50% | 13.4 |
| 5C, 75% | 15.6 |
| 5C, 99% | **31.0** |
| sum | 100 |

points no. 1 and 5 [81].

### 4.4.4. Sound Transmission Loss analysis for setup with five solenoids between the panels of the double-panel structure

In the research described below, Sound Transmission Loss was estimated as a transfer function, with signal acquired by a reference microphone as an input, and signal acquired by room microphone as an output. Signals were demeaned [152]. Sound Transmission Loss is presented in spectral domain to show sound insulation mechanism of the examined structure [99].

As the microphones sense sound in frequency range 20–20000 Hz, all Figures are presented in 20–500 Hz range. If the solenoid coil is supplied with voltage, the coupling is activated. Duty cycle values are the fractions of one period when a voltage signal is active, presented as percentages.

Figures 63a–63c present comparisons of STL estimates obtained for different sce-

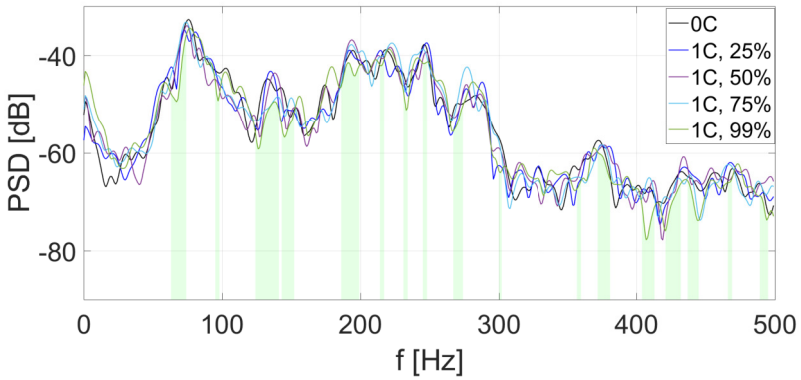


(a) 1 coupling activated.

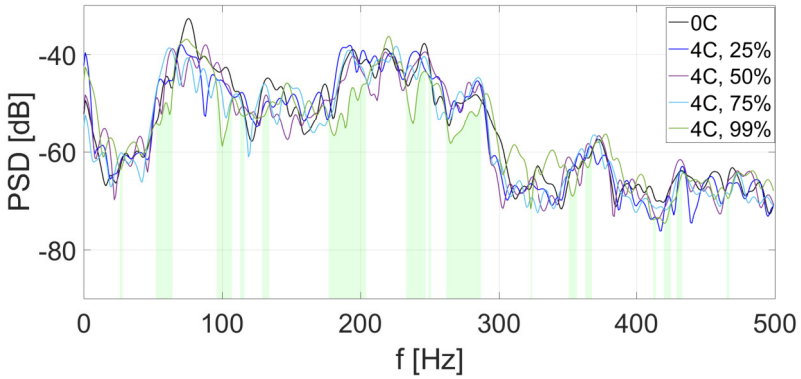


(b) 4 couplings activated.

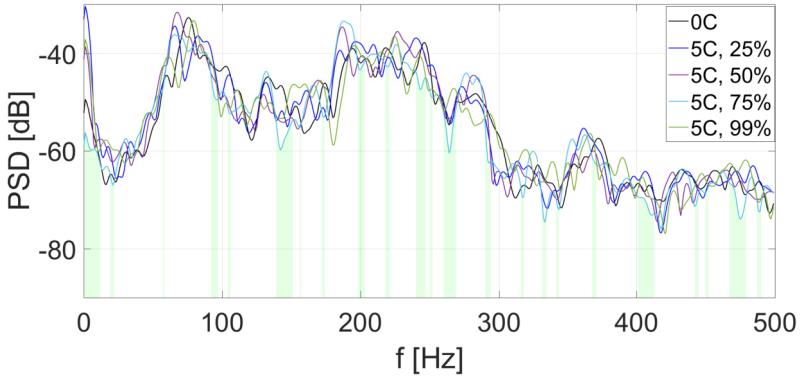


(c) 5 couplings activated.

Figure 62: Power Spectral Density estimates of MFC5 input signals [81].

narios. Fig. 63a presents STL estimates for different values of duty cycle if 1 coupling is activated. As the reference scenario, '0 couplings' scenario is included. Below 186 Hz, all curves are similar. Such effect is not desirable, as the mass-air-mass resonance is located in the low frequencies range. As the frequency increases, the influence of 1 activated coupling on STL level is observed in the narrow frequency ranges. For instance, STL is significantly improved around 186–205 Hz, if duty cycle

Table 21: Efficiency factors calculated for the case of MFC5-measured vibration [81].

| **Number of activated couplings, duty cycle [%]** | **Efficiency factor [%]** |
|---|---|
| 0C | 16.6 |
| 1C, 25% | 19.0 |
| 1C, 50% | 18.6 |
| 1C, 75% | 17.6 |
| 1C, 99% | **28.2** |
| sum | 100 |
| 0C | 9.8 |
| 4C, 25% | 15.0 |
| 4C, 50% | 20.0 |
| 4C, 75% | 26.6 |
| 4C, 99% | **28.6** |
| sum | 100 |
| 0C | 20.0 |
| 5C, 25% | 14.0 |
| 5C, 50% | 18.2 |
| 5C, 75% | **26.6** |
| 5C, 99% | 21.2 |
| sum | 100 |

Table 22: Efficiency factors (EF) obtained for all coupling points, for duty cycle equal to 99%, based on [81].

| **Scenario** | **C1 EF [%]** | **C2 EF [%]** | **C3 EF [%]** | **C4 EF [%]** | **C5 EF [%]** | **Avg [%]** |
|---|---|---|---|---|---|---|
| 1C, 99% | 27.4 | 33.4 | 43.2 | **44.6** | 28.2 | **35.4** |
| 4C, 99% | 29.8 | **42.4** | 26.6 | 33.8 | 28.6 | 32.2 |
| 5C, 99% | 29.8 | **40.6** | 32.0 | 31.0 | 21.2 | 30.9 |
| **Avg [%]** | 29.0 | **38.8** | 33.9 | 36.5 | 26.0 | |

is set to 99%. Similar effect is observed around 246 Hz and 477 Hz for duty cycle set to 75%. If duty cycle is set to 25% and 50%, influence on STL is small, which may indicate that increasing duty cycle value impacts structure's acoustic performance only if it reaches specific level, which in this case is 75%.

Fig. 63b presents STL estimates for different values of duty cycle if 4 couplings are activated, which means that the central solenoid is not supplied with voltage.

The differences between the curves grow above 175 Hz, hence, the STL around mass-air-mass resonance is not significantly improved. In case of 4 activated couplings, there are four most significant peaks of increased STL. By setting duty cycle to 99% all four peaks are suppressed significantly, which is an undesired behaviour. Setting too high duty cycle of PWM signal for the four solenoids located near to the panels' corners leads to a transfer of vibration energy on the panel surface towards its centre what may worsen the acoustic performance of the structure. At 212 Hz and 391 Hz, the improvement of STL is caused by setting duty cycle to 75%. If duty cycle is set to 50%, STL improvement is observed at 410 Hz. Similar effect is observed at 242 Hz for duty cycle equal to 25%.

Fig. 63c presents STL estimates for different values of duty cycle if 5 couplings are activated. Significant differences between curves (more than 10 dB) in form of peaks are observed above 389 Hz. At 391 Hz and 482–491 Hz, STL improvement is caused by setting duty cycle to 99%. Around 413 Hz, STL peak is similar for '0 couplings' scenario and for duty cycle set to 50%. Similarly to two previously discussed diagrams, an improvement of STL around mass-air-mass resonance is not observed. However, in case of 5 activated couplings, peaks of STL are not suppressed if duty cycle equals 99%, which was the issue for 4 couplings activated. It means that it is better to activate all couplings in terms of the structure's acoustic performance hence all areas around the solenoids are stiffened on the same level. At frequencies above 400 Hz such approach allows to reduce the amount of transmitted sound.

For the three discussed scenarios (Figs. 63a–63c), STL enhancement is observed in middle and high frequencies. As each examined setup of the solenoids provides STL improvement for different frequencies, it leads to a conclusion that a combination of different strategies applied at different frequencies may give the best results in terms of the structure's acoustic performance.

Fig. 64a presents the best scenario where maximal STL estimate is created based on all experimental data. The best scenario presented in the diagram is a sequence of thirteen scenarios versus frequency, which allows to obtain the best possible acoustic performance of the structure. In many narrow frequency ranges different scenarios should be selected. All of the scenarios are used, including the '0 couplings' reference scenario.

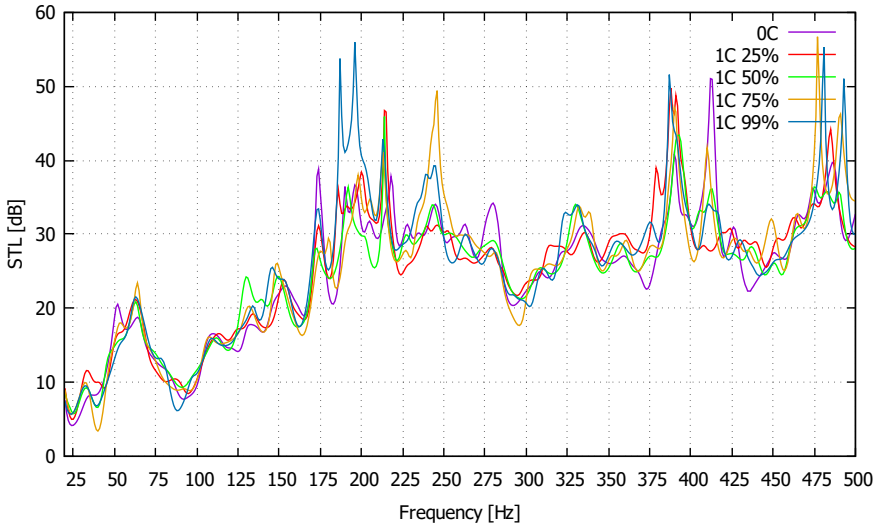


(a)

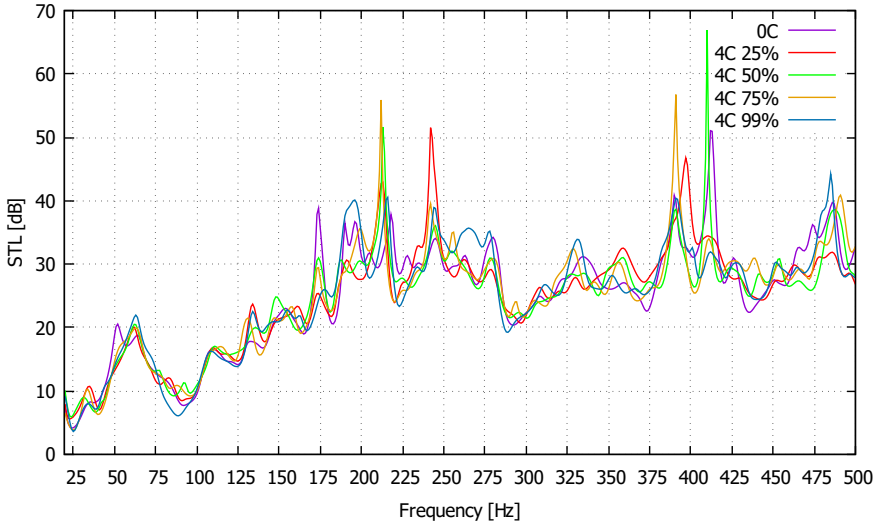


(b)

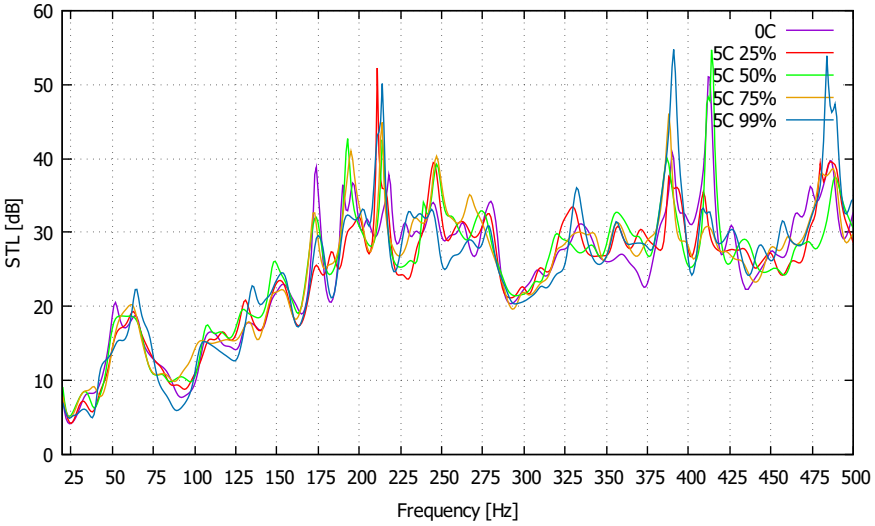


(c)

Figure 63: STL estimates for different values of duty cycle if: (a) 1, (b) 4, (c) 5 couplings are activated.

Table 23 presents percentages of frequencies in range 20–500 Hz where selected scenario is the best one. All examined scenarios have an impact on STL as the percentages are greater than zero. For most of the frequencies, i.e. 12.3%, the best scenario is: 1 activated coupling, duty cycle = 99%. At 9.2% of the frequencies, '0 couplings' scenario is required for the best acoustic performance of the structure. Such result indicates that for almost one tenth of the frequencies different double-panel structure modification may be necessary, for instance different placements and/or number of the couplings.

Table 23: Percentages of frequencies in range 20–500 Hz where selected scenario is the best one.

| **Scenario** | **Percentage of frequencies [%]** |
|---|---|
| 0C | 9.2 |
| 1C, duty cycle = 25% | 10.2 |
| 1C, duty cycle = 50% | 5.6 |
| 1C, duty cycle = 75% | 8.9 |
| 1C, duty cycle = 99% | 12.3 |
| 4C, duty cycle = 25% | 9.6 |
| 4C, duty cycle = 50% | 4.6 |
| 4C, duty cycle = 75% | 6.6 |
| 4C, duty cycle = 99% | 5.8 |
| 5C, duty cycle = 25% | 2.5 |
| 5C, duty cycle = 50% | 8.5 |
| 5C, duty cycle = 75% | 6 |
| 5C, duty cycle = 99% | 10.2 |

In Fig. 64b, the comparison of STL estimate between 0 activated couplings and the best scenario is presented. For most of the frequencies in the considered range, STL enhancement is observed if the MAX_ALL scenario is selected. The highest difference between the best scenario and the scenario of 0 activated couplings is observed at 187 Hz and equals 28.2 dB. The next two biggest differences are: 25.6 dB at 410 Hz and 25.5 dB at 212 Hz. The differences between the reference scenario and the best scenario increase at the middle and high frequencies. The improvement of STL is smaller at the low frequencies, however, it is still observed at most of them.

In Table 24, percentages of frequencies in range 20–500 Hz, where STL estimate

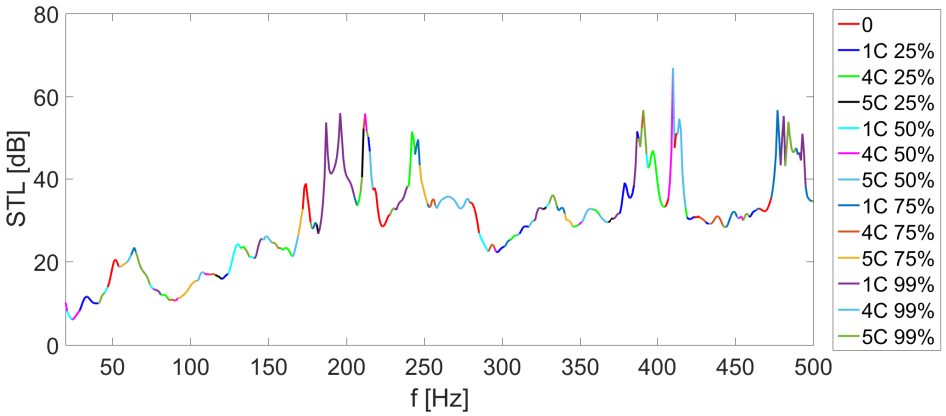


(a)

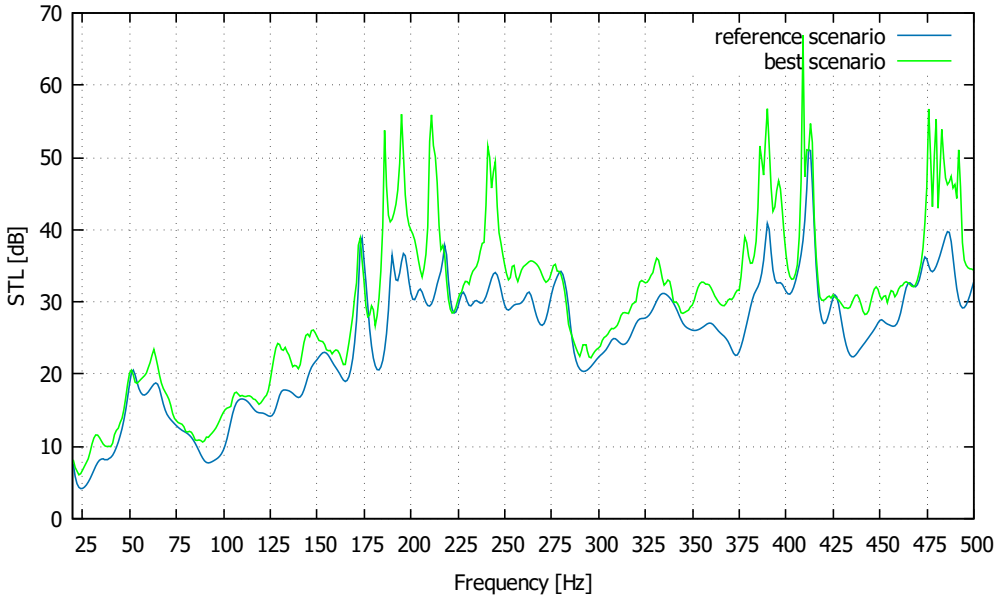


(b)

Figure 64: (a) STL estimate - the best scenario. (b) Comparison of STL estimate between 0 activated couplings and the best scenario.

difference values are in a specified range, are presented. All difference values in the considered frequency range are $\geq 0$ dB. It is observed that for 11.2% of the considered frequency values, STL improvement of more than 10 dB is observed. For more than one fifth of the frequencies in the considered range, STL is improved by more than 5 dB but less than or equal to 10 dB. If the best scenario is selected, STL is improved for 90.8% of all considered frequencies. For most of the frequencies (58.6%) the improvement is less than 5 dB. However, at many frequencies the noise insulation is much better if the couplings are activated, and there is a significant potential of the structure modification in terms of the acoustic performance increase.

Fig. 65a presents the worst scenario where minimal STL estimate is created

Table 24: Percentages of frequencies in range 20–500 Hz where STL estimate difference values are in a specified range.

| **Difference value range [dB]** | **Percentage of frequencies [%]** |
|---|---|
| $> 20$ | 1.4 |
| (15,20] | 2.9 |
| (10,15] | 6.9 |
| (5,10] | 21 |
| (0,5] | 58.6 |
| 0 | 9.2 |

based on all experimental data. The diagram shows that not always the reference scenario is the worst one and that the improper control of the couplings may lead to worse sound insulation of the structure. If a particular frequency or a narrow frequency band is of interest, then such knowledge may help while designing the control system, to avoid decrease of sound insulation. In Fig. 65b, the comparison of STL estimate between 0 activated couplings and the worst scenario is presented. The biggest difference is observed at 412 Hz, where selection of the worst scenario causes decrease of STL equal to 23.3 dB. The graph shows how the improper use of double-panel structure modification may lead to worse noise insulation. It is necessary to control the couplings in a proper manner to provide the best possible STL enhancement.

In Table 25, mean, median, maximal and minimal values of STL estimate for different scenarios are presented. If the best scenario is selected, the mean STL improvement equals 4.9 dB in comparison to the '0 couplings' scenario, and median STL improvement equals 3.6 dB. The minimal value of STL in the considered range is almost 2 dB higher than in '0 couplings' scenario, and the maximal value increases by almost 16 dB. However, it has to be emphasized that such beneficial effects are observed only for the proper selection of scenarios based on the frequency. If the structure couplings are employed in the wrong manner, the mean STL can be as much as 3.2 dB worse than in '0 couplings' scenario, median value drops by 2.4 dB, and the maximal STL value drops by 14.9 dB. Hence, scenarios have to be selected carefully in the considered frequency range, based on the goal of structure modification, i.e. improvement of acoustic performance, vibration reduction, etc.

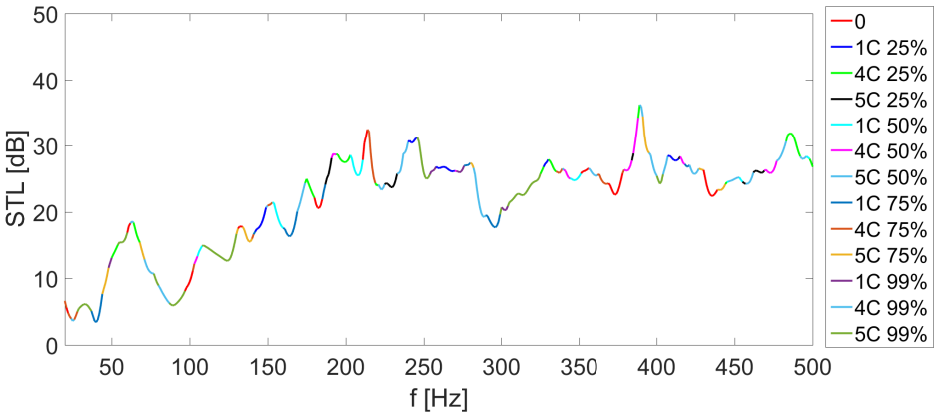


(a)

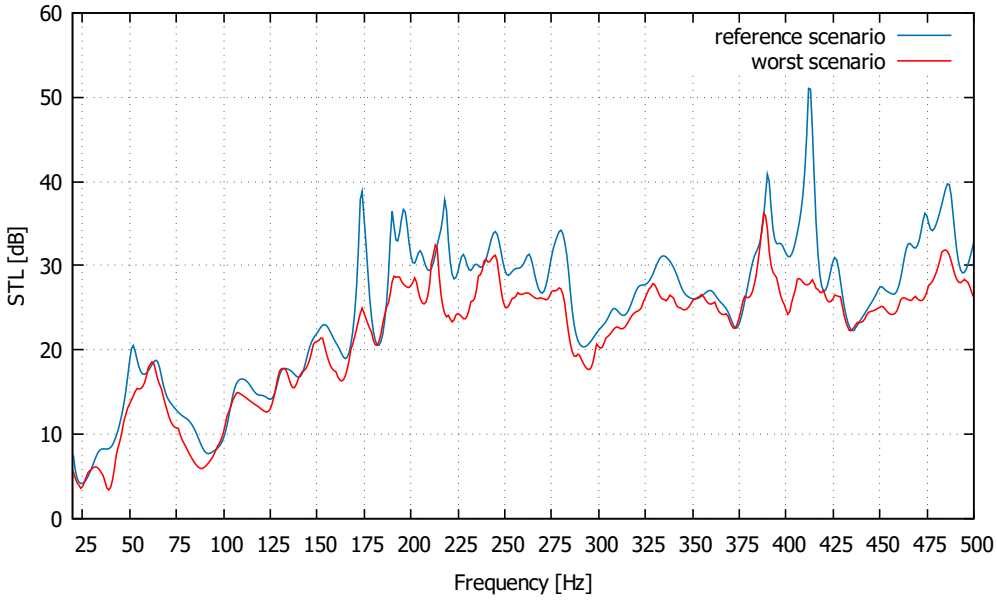


(b)

Figure 65: (a) STL estimate - the worst scenario. (b) Comparison of STL estimate between 0 activated couplings and the worst scenario.

However, in general, if the best scenario is selected, the impact on STL in comparison to the reference scenario is higher than if the worst scenario is compared with the reference one. This indicates the potential of proposed setup in the field of noise reduction.

Table 25: Mean, median, maximal and minimal values of STL estimate for different scenarios.

| **Scenario** | **Mean val. [dB]** | **Median val. [dB]** | **Min val. [dB]** | **Max val. [dB]** |
|---|---|---|---|---|
| Reference | 24.9 | 26.6 | 4.2 | 51.1 |
| Best | 29.8 | 30.2 | 6.1 | 66.9 |
| Worst | 21.7 | 24.2 | 3.4 | 36.2 |

### 4.4.5. Five electromagnetic couplings: control algorithm

In the current version of the proposed experimental setups, the solenoids can be turned on (by supplying with voltage of peak-to-peak value equal to 11 V) or turned off. Duty cycle of a PWM signal can also be modified, what, in turn, impacts the behaviour of the electromagnetic couplings. Change of a duty cycle modulates the signal and defines what is the percentage of the signal's period when it is on. As the duty cycle varies, change of the induced electromagnetic force is also observed. This impacts vibroacoustic properties of the double-panel structure equipped with the couplings, what was examined in the described research.

Such setup is a basic one, and different improvements may be proposed to develop the control strategy. For instance, different number and coordinates of the couplings may be applied to the structure. Also, different duty cycle values may be examined in terms of their influence on vibroacoustics of the structure. Having the extended dataset of the results obtained for different experimental setups, one may develop a simple table-lookup algorithm of a low computational burden [153], and employ it for the control of the couplings. Such approach may lead to enhancement of both noise and vibration reduction for specific set of known inputs, as the optimal setup may be selected and enabled based on the mentioned table.

Complexity of the control system increases if the set of input features is unknown. Then, a strategy to estimate the outputs has to be determined. Nowadays, due to a fast development of machine learning techniques and open-source numerical libraries (e.g. sklearn [154]), one may take advantage of them to determine the best setup of the couplings, having the extended dataset with the research outcome already gathered. The numerical libraries allow to run various algorithms and obtain both predictions and their visualizations. However, there are many risks related to such methods. First, a model may be underfitted or overfitted. Lack of biases in the datasets is also important, as well as a relevance of input features, a proper split to training, test and validation sets, etc. [155]

Knowing the number of the couplings and of the activated solenoids, and duty cycle values, one may determine the best experimental setup for particular noise frequency and the corresponding Sound Transmission Loss estimate value. Such data may be stored in a dataset. However, when the outputs are unknown for

a particular frequency measured in a real time, then machine learning techniques may be applied in order to determine the most efficient control setup, using the existing dataset as a basis. In this example, STL estimate is selected as an acoustic indicator, but the choice of inputs and its number depends on the research needs. A multi-output regression algorithm may be employed to determine the values of all unknown outputs. An example of a block scheme of such strategy is presented in Fig. 66.

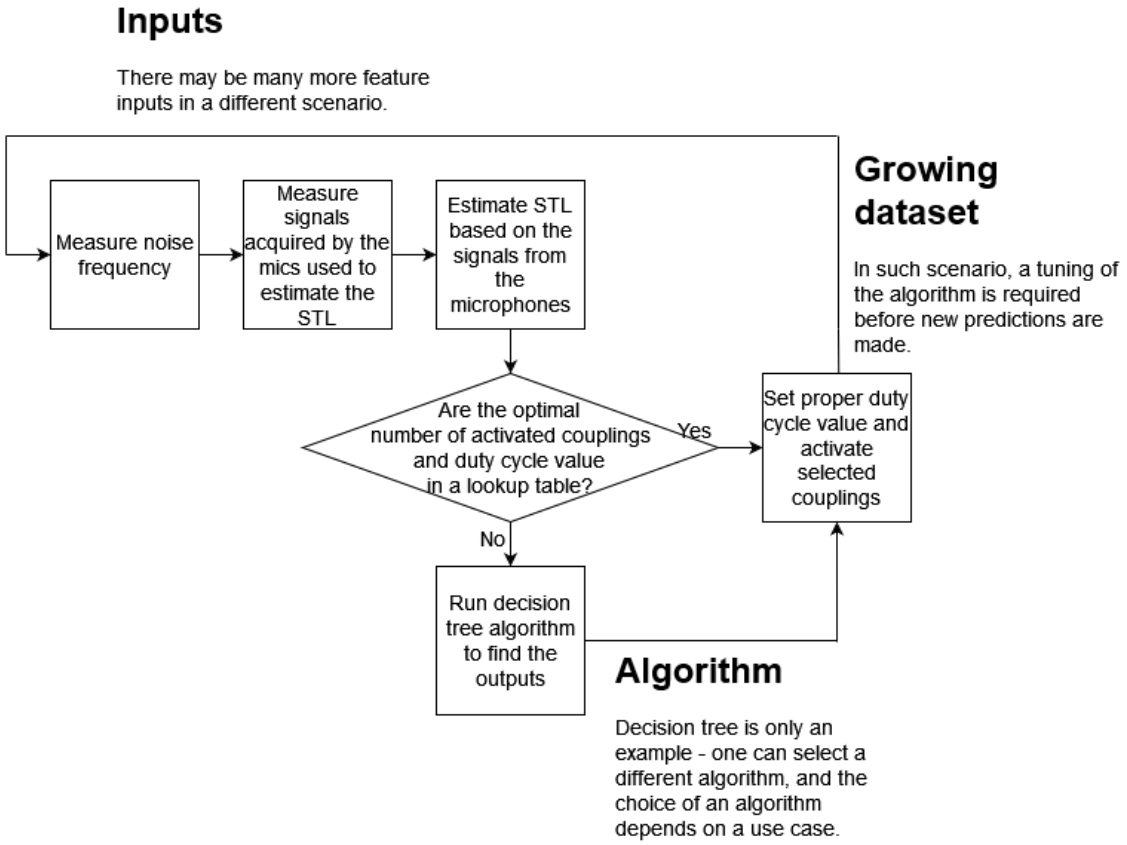


Figure 66: Exemplary scheme of a control strategy.

A real example, with specific outputs: number of the solenoids which are turned on, and duty cycle, is presented in Fig. The dataset consists STL estimates obtained for particular noise frequencies, in this case up to 500 Hz with a step of 1 Hz.

The described approaches may be extended in the future research to take into account environmental conditions such as room temperature and humidity of the air, or various vibroacoustic indicators and measures. Proper tuning of such algorithm based on the selected criteria may result in an increased efficiency of the proposed method. The scenario may also be analyzed in an opposite way, where the inputs and

outputs may be swapped, and a vibroacoustic indicator may be predicted based on the laboratory setup. Such approach may be helpful in case of a complex laboratory environment, which may be difficult to model it both analytically and numerically.

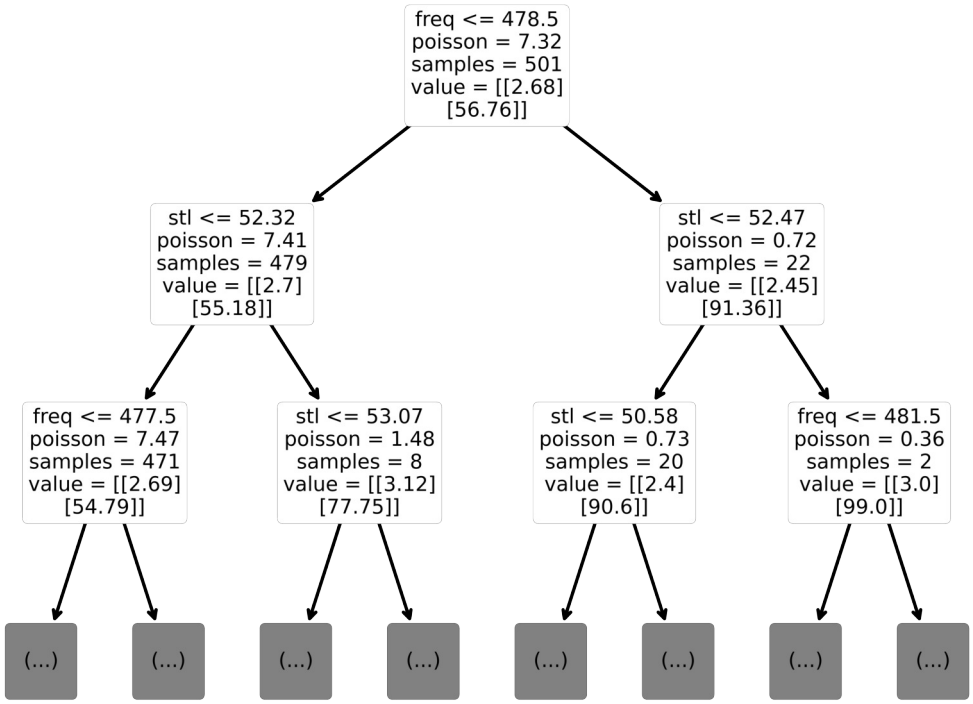


Figure 67: Part of the decision tree for multi-output regression (max. visualized depth = 2).

## 4.5. Conclusions

Semi-active modification of the double-panel structure by means of electromagnetic couplings is a novel approach to influence vibroacoustic properties of the structure in a way that may lead to vibration reduction on the radiating panel, and enhance noise insulation of the structure. Such effects may be achieved by introducing a different number of solenoids, choice of their positions, and change of duty cycle of a PWM signal. These factors impact the behaviour of the couplings between the panels. Another conditions influencing the results may be a manufacturing technology of the panels, as well as a way of mounting the solenoids to the panels.

Preliminary experiment with single solenoid between the panels of the double-panel structure showed that one coupling between the panels is not enough to provide

significant vibration reduction on the radiating panel. The only mode for which slight surface-averaged vibration was observed, was (1, 1). Hence, five couplings were then mounted between the panels.

First experiment with 5 solenoids between the panels was performed using MFCs as the vibration sensors. RMS levels of MFC-acquired signals were calculated to notice any changes for different setups. It was observed that activation of the coupling (an increase of duty cycle from 0% to non-zero value) has a stronger impact on the radiating panel's vibration than further increase of duty cycle. In most of the scenarios, only duty cycle equal to 99% allowed to achieve reduced vibration of the radiating panel locally. Two important phenomena were observed and confirmed during the experiment, based on the results. The first one is that vibration energy is transferred to different areas of the panel if the duty cycle increases for the specific coupling. The second one is that there is a significantly stronger transfer of vibrations from the incident panel to the radiating panel is all 5 couplings are activated, but only for a specific duty cycle value. Also, it was noticed that the central solenoid's activation had the most significant impact on the vibration reduction on the radiating panel, as the panel's edges are assumed to be fully clamped.

Another analysis was focused on the PSD estimates obtained from the MFC-acquired signals. The results showed that arbitrarily selected positions of the couplings may provide vibration reduction in a wide frequency band, but to achieve the best effects, probably an optimization algorithms should be developed. Setting duty cycle value to 99% provided the best results in terms of PSD estimates' decrease. However, this should not be a general rule, as the highest efficiency factor of all considered ones was related to the 'one coupling only' scenario. This also indicates that placing one of the couplings at the central point between the panels is beneficial in terms of vibration reduction over a wide frequency band.

In the next experiment, the influence of double-panel structure modification on its sound insulation performance was examined. As an indicator, an estimate of the Sound Transmission Loss was calculated, based on the signals acquired by the microphones. As the number of activated couplings between the panels and the duty cycle of PWM signal varied, noise insulation properties of the structure changed, allowing to select the best scenario for given tonal or narrowband noise, and change

the scenario online to respond to nonstationary noise.

The Sound Transmission Loss is a reliable indicator of the double-panel structure acoustic energy being reflected or dissipated. Increase of its value is desirable and shows an improvement of sound insulation of the structure. As the solenoids are employed in the role of electromagnetic couplings, it is shown that the proper choice of their setup may lead to better acoustic performance of the structure. However, it has to be done carefully, as the improper control of the couplings may lead to an opposite effect. Knowledge of both the best and the worst scenarios may help in the design of the double-panel structure modifications and would lead to a more efficient control system. The overall system thus should identify the frequency of the tonal or narrowband noise and select the best coupling scenario based on a look-up table of recommended settings. Such table can be defined during the installation stage and be fixed provided the environment conditions do not change too much to significantly change the structure response. Otherwise, a tuning should be performed, what may be the subject of further research.

The promising effect of coupling the structure with electromagnetic elements is observed in a wide frequency band, where STL is enhanced. Thus, the modified structure provides satisfactory results in terms of both vibration reduction and noise insulation.

It has been confirmed that employment of the double-panel structures for noise and vibration reduction is reasonable. One of the advantages of the double panels is the possibility to introduce couplings between the panels in the air cavity. Such structures may be part of the casings enclosing noise- and vibration-generating devices as their walls. Generally, double panels are lightweight, and thus they can be adapted for various industrial or household appliances.

# 5. Summary

## 5.1. Conclusions

This dissertation is concerned with noise and vibration reduction of a device enclosed in a thin-walled casing with the use of structural interaction. It consists of two main fields of research, which are: active structural acoustic control of a lightweight device casing in an enclosure with reflective walls inside, and the influence of the introduced double-panel structure modification on the structure's vibroacoustic properties. Besides an experimental part of the research presented in this dissertation, several models for single panels and double-panel structures were implemented to better understand the vibroacoustics of the employed structures.

In the first part of research, an active structural acoustic control approach was applied with the use of lightweight device casing placed at a wall, and then in a corner. The wall and the corner were prepared to provide reflective surfaces in the laboratory enclosure without a need to remove pyramid acoustic foam panels from its walls. Both wall and corner design aimed to provide as lowest as possible absorption coefficient value. The lightweight device casing was intentionally placed close to the reflective surfaces to impact active control performance. Distances between the casing and the wall were determined based on the principle known from the literature. In the experiment for the device casing placed at the reflective wall, a preliminary analysis of the primary and secondary paths was carried out. The results provided information about the most beneficial distances between the casing and the wall in terms of magnitudes to be reduced at the specific frequency bands. The research indicated a significant influence of the distance between the casing and the reflective wall on the magnitudes of the amplitude responses for both the primary and secondary paths. Trends of a magnitude increase/decrease for a change of distance between the casing and the wall were observed. As the amplitude responses of the primary and secondary paths increased in a similar manner, it was expected that they should be balanced and hence should not impact active control performance in a negative manner. In the next stage of research, the corner was built based on the previously prepared wall and—besides an analysis of the amplitude responses

of both the primary and secondary paths—an active control performance was examined. Proper selection of both error microphones' arrangement and a distance between the casing and the corner led to enhanced sound pressure level reduction in a wider frequency band, in comparison to the results obtained prior to this research for the casing located distant from the acoustic foam-covered laboratory enclosure walls. Another important observation was that the control system can be simplified (and the number of actuators can be reduced) if the device casing is placed close to the corner, due to the phenomenon of vibrational couplings between the opposite panels of the device casing. Also, when the casing is placed at the low distance from the corner, control system can be further simplified and the error microphones located in the narrow gap between the casing and the corner can be disabled. Such setup would be less efficient than the one with five error sensors arranged on the opposite side of the casing, but it would not impede active control algorithm's adaptation.

In the second part of research, double-panel structure modification by means of solenoids as the couplings was introduced in a rigid device casing. In the preliminary experiment, one electromagnetic coupling was placed between the panels of the structure and vibroacoustic analysis was carried out. The results were not satisfactory and led to a conclusion that more than one coupling should be mounted between the panels. One central coupling provided a slight vibration reduction on the radiating panel only for one of the modes, and enhanced vibration of the radiating panel for the other resonances. Hence, five couplings were then mounted between the panels. Vibrations were measured by means of Macro-Fiber Composites, and microphones were used to sense sound pressure levels inside and outside the rigid device casing. The results showed that vibrations of the radiating panel can be significantly reduced if the solenoids are enabled, and proper configuration of number of activated couplings and duty cycle value are selected. Another experiment results indicated that Sound Transmission Loss can be enhanced over the wide frequency band if a proper sequence of configurations at the particular frequencies is applied.

In this dissertation, specific applications of interactions in a double-panel structure, or between device casing panels and reflective enclosure walls, are discussed. The results indicated that proper use of reflective surfaces placed near a lightweight

device casing may lead to global noise reduction levels' enhancement over a wide frequency band, and that the results are at least of the same quality when compared to the research conducted in acoustic foam-covered laboratory enclosure. Introducing interactions between the panels of a double-panel structure by means of solenoids may lead to both Sound Transmission Loss enhancement over a wide frequency band, and vibration reduction in selected areas of the radiating panel.

## 5.2. Author's contribution

The author believes that her contributions are the following:

- Participation in laboratory setup building: design and implementation of the reflective surfaces used in the experiment for a lightweight device casing placed at a wall and in a corner.

- Proposal of different error microphones setups for a lightweight device casing placed in a corner.

- Participation in experimental validation and analysis of a lightweight device casing placed at a wall and in a corner.

- Implementation of an analytical model of Sound Transmission Loss of a double-panel structure fully clamped on an infinite acoustic rigid baffle of Xin et al. by means of numerical software.

- Participation in theoretical development of the concepts of the active, semi-active and passive couplings between the panels of a double-panel structure.

- Implementation, experimental validation and analysis of introduced semi-active couplings between the panels of a double-panel structure in terms of vibration RMS levels reduction.

- Implementation, experimental validation and analysis of introduced semi-active couplings between the panels of a double-panel structure in terms of vibration PSD estimates' levels reduction.

- Implementation, experimental validation and analysis of introduced semi-active couplings between the panels of a double-panel structure in terms of Sound Transmission Loss enhancement.
- Proposal of the selected machine learning techniques' application for modeling of Sound Transmission Loss of a double-panel structure with the semi-active couplings.

## 5.3. Research project and perspectives for future research

The research has been partially supported by the National Science Centre, under the Grant no. DEC-2017/25/B/ST7/02236. Besides the topics of this dissertation, other research problems have also been undertaken in the project:

- models' development for the purposes of optimizing the arrangement of sensors and actuators and shaping the frequency response,
- further development of passive methods with the use of optimally arranged additional masses and ribs,
- development of semi-active methods based on the shunt technology,
- employment of the sophisticated control algorithms characterized by a lower computational burden in the active control systems.

The conclusions drawn from the research described in this dissertation motivate to further develop the proposed setups and methods. The next steps in future research may be:

- development of different double-panel structure modifications by means of improved actuators which would not heat up and still would provide a possibility to be controlled in a non-binary way,
- optimization of the number and placement of the actuators between the panels of the double-panel structure,
- further employment of machine learning techniques for the purposes of modeling the complex, real environments, to predict vibroacoustic indicators of the examined structures,

- development of a theoretical basis with a set of general rules of how to locate device casing enclosing noise-generating device in an industrial or household enclosure with reflective walls; both distance from the surfaces as well as the design of control system should be taken into account.

Each of the mentioned perspectives constitutes a complex research challenge. However, these concepts motivate for further work on the noise and vibration control approaches to provide even better noise and vibration reduction for both single panels and double-panel structures employed in the casings enclosing a noise-generating device, placed in the real, complex environments.

# References

[1] C.-Y. Lin, P.-J. Tsai, K.-Y. Lin, C.-Y. Chen, L.-H. Chung, J.-L. Wu, and Y.L. Guo. Will daytime occupational noise exposures induce nighttime sleep disturbance? *Sleep Medicine*, 50:87–96, 2018.

[2] Y.-T. Lin, T.-W. Chen, Y.-C. Chang, M.-L. Chen, and B.-F. Hwang. Relationship between time-varying exposure to occupational noise and incident hypertension: A prospective cohort study. *International Journal of Hygiene and Environmental Health*, 226:113487, 05 2020.

[3] H.S. Sanjay, B. Hiremath, B. Prithvi, and P. Dinesh. Machine learning based assessment of auditory threshold perception in human beings. *SN Applied Sciences*, 2, 02 2020.

[4] I. Alimohammadi and H. Ebrahimi. Comparison between effects of low and high frequency noise on mental performance. *Applied Acoustics*, 126:131–135, 2017.

[5] S.L. Lusk, M. McCullagh, V.V. Dickson, and J. Xu. Position statement: Harmful effects of environmental noise exposures. *Nursing Outlook*, 64(4):395—396, 2016.

[6] A. Domingo-Pueyo, J. Sanz-Valero, and C. Wanden-Berghe. Disorders induced by direct occupational exposure to noise: Systematic review. *Noise and Health*, 18:229, 09 2016.

[7] M. Pawełczyk. *Feedback control of acoustic noise at desired locations.* Wydawnictwo Politechniki Slaskiej, Gliwice, 2005.

[8] S.M. Kuo and D.R. Morgan. Active noise control: a tutorial review. *Proceedings of the IEEE*, 87(6):943–973, 1999.

[9] F. Bunn and P. Zannin. Assessment of railway noise in an urban setting. *Applied Acoustics*, 104:16–23, 03 2016.

[10] G. Licitra, L. Fredianelli, D. Petri, and M. Vigotti. Annoyance evaluation due to overall railway noise and vibration in Pisa urban areas. *Science of The Total Environment*, 568, 01 2016.

[11] C. Iglesias Merchan, L. Diaz-Balteiro, and M. Soliño. Transportation planning and quiet natural areas preservation: Aircraft overflights noise assessment in a National Park. *Transportation Research Part D Transport and Environment*, 41:1–12, 12 2015.

[12] R. Guski, D. Schreckenberg, and R. Schuemer. WHO environmental noise guidelines for the European Region: A systematic review on environmental noise and annoyance. *International Journal of Environmental Research and Public Health*, 14:1539, 12 2017.

[13] D. Michaud, K. Feder, S. Keith, S. Voicescu, L. Marro, J. Than, M. Guay, A. Denning, D. McGuire, T. Bower, E. Lavigne, B. Murray, S. Weiss, and F. van den Berg. Exposure to wind turbine noise: Perceptual responses and reported health effects. *The Journal of the Acoustical Society of America*, 139:1443–1454, 03 2016.

[14] L. Fredianelli, M. Nastasi, M. Bernardini, F. Fidecaro, and G. Licitra. Pass-by characterization of noise emitted by different categories of seagoing ships in ports. *Sustainability*, 12:1740, 02 2020.

[15] M. Sibielak, W. Rączka, J. Konieczny, and J. Kowal. Optimal control based on a modified quadratic performance index for systems disturbed by sinusoidal signals. *Mechanical Systems and Signal Processing*, 64–65:498–519, 2015.

[16] B.A.T. Petersson. *General Introduction to Vibration*, chapter 11, pages 169–179. John Wiley & Sons, Ltd, 2007.

[17] H. Ayaz and F. Dehais. *Neuroergonomics: The Brain at Work and in Everyday Life*. Elsevier, 01 2019.

[18] Z. Li, Q. Zhang, F. Fan, and S. Shen. A method for calculating uncomfortable rates of people due to vertical floor vibrations using corresponding assessment

values based on fuzzy reliability theory. *Journal of Building Engineering*, 28:101061, 2020.

[19] T. Addabbo, A. Fort, E. Landi, R. Moretti, M. Mugnaini, L. Parri, and V. Vignoli. A wearable low-cost measurement system for estimation of human exposure to vibrations. In *2019 IEEE 5th International forum on Research and Technology for Society and Industry (RTSI)*, pages 442–446, 2019.

[20] J.L. Cueto, A.M. Petrovici, R. Hernández, and F. Fernández. Analysis of the impact of bus signal priority on urban noise. *Acta Acustica united with Acustica*, 103(4):561–573, 2017.

[21] D. Morley, K. Hoogh, D. Fecht, F. Fabbri, M. Bell, P. Goodman, P. Elliott, S. Hodgson, A.L. Hansell, and J. Gulliver. International scale implementation of the CNOSSOS-EU road traffic noise prediction model for epidemiological studies. *Environmental pollution (Barking, Essex : 1987)*, 206:332–341, 07 2015.

[22] L. Teti, G. de Leon, A. Del Pizzo, A. Moro, F. Bianco, L. Fredianelli, and G. Licitra. Modelling the acoustic performance of newly laid low-noise pavements. *Construction and Building Materials*, 247:118509, 06 2020.

[23] M.D. Rao. Recent applications of viscoelastic damping for noise control in automobiles and commercial airplanes. *Journal of Sound and Vibration*, 262(3):457 – 474, 2003. 2001 India-USA Symposium on Emerging Trends in Vibration and Noise Engineering.

[24] S.J. Elliott and P.A. Nelson. Active noise control. *IEEE Signal Processing Magazine*, 10(4):12–35, 1993.

[25] S. Elliott, J. Cheer, B. Lam, C. Shi, and W.-S. Gan. A wavenumber approach to analysing the active control of plane waves with arrays of secondary sources. *Journal of Sound and Vibration*, 419, 01 2018.

[26] C. Antoñanzas, M. Ferrer, M. de Diego, and A. Gonzalez. Blockwise frequency domain active noise controller over distributed networks. *Applied Sciences*, 6:124, 04 2016.

[27] S. Wrona and M. Pawełczyk. Active reduction of device narrowband noise by controlling vibration of its casing based on structural sensors. In *22nd International Congress on Sound and Vibration, Florence, Italy*, 07 2015.

[28] P. Loiseau, P. Chevrel, M. Yagoubi, and J.-M. Duffal. Robust active noise control in a car cabin: Evaluation of achievable performances with a feedback control scheme. *Control Engineering Practice*, 81:172–182, 2018.

[29] F. Fahy and P. Gardonio. 5 - transmission of sound through partitions. In F. Fahy and P. Gardonio, editors, *Sound and Structural Vibration (Second Edition)*, pages 277 – 373. Academic Press, Oxford, second edition edition, 2007.

[30] T. Murao, C. Shi, W.-S. Gan, and M. Nishimura. Mixed-error approach for multi-channel active noise control of open windows. *Applied Acoustics*, 127:305–315, 2017.

[31] B. Lam, C. Shi, D. Shi, and W.-S. Gan. Active control of sound through full-sized open windows. *Building and Environment*, 141:16–27, 2018.

[32] L. Leniowska and M. Sierżęga. Vibration control of a circular plate using parametric controller with phase shift adjustment. *Mechatronics*, 58:39–46, 2019.

[33] S. Kuo and D. Morgan. *Active Noise Control Systems: Algorithms and DSP Implementations*. Wiley-Interscience; 1st edition, 1996.

[34] S.J. Elliott. *Signal Processing for Active Control*. Academic Press, London, 2001.

[35] Q. Mao and S.J. Pietrzko. *Control of Noise and Structural Vibration. A Matlab-Based Approach*. Springer, London, 2013.

[36] A. **Chrapońska**, S. Wrona, J. Rzepecki, K. Mazur, and M. Pawełczyk. Active structural acoustic control of an active casing placed in a corner. *Applied Sciences*, 9(6):1059, 2019.

[37] M. Pawełczyk. *Application-Oriented Design of Active Noise Control Systems*. Academic Publishing House Exit, Warszawa, 2013.

[38] M. Misol and S. Algermissen. Remote sensing for a lining integrated active structural acoustic control system. In *9th EASN International Conference*, September 2019.

[39] A. **Chrapońska**, J. Rzepecki, K. Mazur, S. Wrona, and M. Pawełczyk. Influence of double-panel structure modification on vibroacoustical properties of a rigid device casing. *Archives of Acoustics*, 45:119–127, 02 2020.

[40] J. Rzepecki, A. **Chrapońska**, K. Mazur, S. Wrona, and M. Pawełczyk. Semi-active reduction of device casing vibration using a set of piezoelectric elements. In *20th International Carpathian Control Conference : ICCC 2019, Krakow-Wieliczka, 26-29 May 2019, Institute of Electrical and Electronics Engineers, pp.1-5, ISBN 978-1-7281-0703-5*, 2019.

[41] L. Zhao and F. Semperlotti. Embedded Acoustic Black Holes for semi-passive broadband vibration attenuation in thin-walled structures. *Journal of Sound Vibration*, 388:42–52, February 2017.

[42] T. Wei, B. Wang, J. Cao, and B. Bao. Experimental comparisons of two detection methods for semi-passive piezoelectric structural damping. *Journal of Vibration Engineering & Technologies*, 5:367–379, 09 2017.

[43] F. Xin, T. Lu, and C. Chen. Vibroacoustic behavior of clamp mounted double-panel partition with enclosure air cavity. *The Journal of the Acoustical Society of America*, 124 6:3604–12, 2008.

[44] A.J.B. Tadeu and D.M.R. Mateus. Sound transmission through single, double and triple glazing. experimental evaluation. *Applied Acoustics*, 62(3):307 – 325, 2001.

[45] L. Guo, J. Ge, and S. Liu. Analysis of vibration and acoustic characteristics of a simply supported double-panel partition under thermal environment. *Shock and Vibration*, 2020:1–11, 02 2020.

[46] D. Yao, J. Zhang, W. Ruiqian, and X. Xiao. Effects of mounting positions and boundary conditions on the sound transmission loss of panels in a niche. *Journal of Zhejiang University - Science A: Applied Physics & Engineering*, 21:129–146, 02 2020.

[47] M. Huang and M. Chen. Analysis of Sound Transmission Loss on infinite double-panel partition. pages 1–6, 12 2018.

[48] P.N. Thanh and T.I. Thinh. Vibroacoustic response of a finite simply supported double-composite plate filled with an air cavity. In *Advances in Engineering Research and Application*, pages 720–732, Cham, 2020. Springer International Publishing.

[49] Y. Liu and J.-C. Catalan. External mean flow influence on sound transmission through finite clamped double-wall sandwich panels. *Journal of Sound and Vibration*, 405:269 – 286, 2017.

[50] A. Sahu, P. Bhattacharya, A. Niyogi, and M. Rose. A mobility based vibroacoustic energy transmission simulation into an enclosure through a double-wall panel. *The Journal of the Acoustical Society of America*, 141:EL598–EL604, 06 2017.

[51] Y. Qin, G.-P. Shu, G.-G. Zhou, and J.-H. Han. Compressive behavior of double skin composite wall with different plate thicknesses. *Journal of Constructional Steel Research*, 157:297 – 313, 2019.

[52] P. Oliazadeh, A. Farshidianfar, and M.J. Crocker. Study of sound transmission through single- and double-walled plates with absorbing material: Experimental and analytical investigation. *Applied Acoustics*, 145:7 – 24, 2019.

[53] H.-S. Kim, S.-R. Kim, S.-H. Lee, Y.-H. Seo, and P.-S. Ma. Sound transmission loss of double plates with an air cavity between them in a rigid duct. *The Journal of the Acoustical Society of America*, 139:2324–2333, 05 2016.

[54] C. Bao and J. Pan. Experimental study of different approaches for active control of sound transmission through double walls. *The Journal of the Acoustical Society of America*, 102(3):1664–1670, 1997.

[55] X. Ma, K. Chen, S. Ding, and H. Yu. Physical mechanisms of active control of sound transmission through rib stiffened double-panel structure. *Journal of Sound and Vibration*, 371:2–18, 2016.

[56] L. Morzyński and G. Szczepański. Double panel structure for active control of noise transmission. *Archives of Acoustics*, 43(4):689–696, 2018.

[57] S. Wrona and M. Pawełczyk. Feedforward control of double-panel casing for active reduction of device noise. *Journal of Low Frequency Noise, Vibration and Active Control*, pages 3–5, 2018.

[58] I. Yahya. Analytical expression for sound transmission loss calculation: An improvement to the existing method after Singh and Katra. *Advances in Acoustics and Vibration*, 2009, 12 2009.

[59] C. Soussi, W. Larbi, and J.-F. Deü. *Experimental and Numerical Analysis of Sound Transmission Loss Through Double Glazing Windows: Proceedings of the Second International Conference on Acoustics and Vibration (ICAV2018), March 19-21, 2018, Hammamet, Tunisia*, pages 195–203. 01 2019.

[60] F.X. Xin, T.J. Lu, and C.Q. Chen. Dynamic response and acoustic radiation of double-leaf metallic panel partition under sound excitation. *Computational Materials Science*, 46(3):728 – 732, 2009. Proceedings of the 18th International Workshop on Computational Mechanics of Materials.

[61] M. Pawełczyk, J. Rzepecki, and S. Wrona. Polaktywny elektromagnetyczny tlumik drgan poprzecznych elementow powierzchniowych, Polish patent no. P.426875.

[62] Y. Li and J. Gao. Energy transmission in a mechanically-linked double-wall structure coupled to an acoustic enclosure. *The Journal of the Acoustical Society of America*, 117:2742–51, 06 2005.

[63] Q. Mao and H. Shen. Improvement on sound transmission loss through a double-plate structure by connected with a mass–spring–damper system. *Advances in Mechanical Engineering*, 9(7):1687814017713946, 2017.

[64] Q. Mao. Improvement on sound transmission loss through a double-plate structure by using electromagnetic shunt damper. *Applied Acoustics*, 158:107075, 2020.

[65] O. Akintoye. Analytical modelling of sound transmission through finite clamped double-wall panels with magnetic-linked stiffness. *Acoustics Australia*, 47, 04 2019.

[66] F. Langfeldt, H. Hoppen, and W. Gleine. Broadband low-frequency sound transmission loss improvement of double walls with Helmholtz resonators. *Journal of Sound and Vibration*, 476:115309, 2020.

[67] X. Ma, K. Chen, and J. Xu. Active control of sound transmission through orthogonally rib stiffened double-panel structure: Mechanism analysis. *Applied Sciences*, 9:3286, 08 2019.

[68] S.J. Pietrzko and Q. Mao. New results in active and passive control of sound transmission through double wall structures. *Aerospace Science and Technology*, 12(1):42–53, 2008.

[69] P. Sas, C. Bao, F. Augusztinovicz, and W. Desmet. Active control of sound transmission through a double panel partition. *Journal of Sound and Vibration*, 180(4):609 – 625, 1995.

[70] C.W. Isaac, M. Pawełczyk, and S. Wrona. Comparative study of sound transmission losses of sandwich composite double panel walls. *Applied Sciences*, 10:1543, 02 2020.

[71] C. Shen, J.-C. Catalan, and Y. Liu. Effects of external and air gap flows on sound transmission through finite clamped double-panel sandwich structures. *Composite Structures*, 203:286 – 299, 2018.

[72] W.C. Tang, H. Zheng, and C.F. Ng. Low frequency sound transmission through close-fitting finite sandwich panels. *Applied Acoustics*, 55(1):13 – 30, 1998.

[73] C. Shen, H. Zhang, and Y. Liu. Analytical modelling of Sound Transmission Loss across finite clamped triple-wall sandwich panels in the presence of external mean flow. *Applied Mathematical Modelling*, 73:146 – 165, 2019.

[74] P. Gulia and A. Gupta. Enhancing the Sound Transmission Loss through acoustic double panel using sonic crystal and porous material. *The Journal of the Acoustical Society of America*, 144:1435–1442, 09 2018.

[75] N.G.R. de Melo Filho, L. Van Belle, C. Claeys, E. Deckers, and W. Desmet. Dynamic mass based sound transmission loss prediction of vibro-acoustic metamaterial double panels applied to the mass-air-mass resonance. *Journal of Sound and Vibration*, 442:28 – 44, 2019.

[76] N. Filho, C. Claeys, E. Deckers, and W. Desmet. Metamaterial foam core sandwich panel designed to attenuate the mass-spring-mass resonance sound transmission loss dip. *Mechanical Systems and Signal Processing*, 139:106624, 05 2020.

[77] T. Fu, Z. Chen, D. Yu, X. Wang, and W. Lu. Sound transmission from stiffened double laminated composite plates. *Wave Motion*, 72:331–341, 2017.

[78] H. Qiao, Z. He, W. Jiang, and W. Peng. Sound transmission of periodic composite structure lined with porous core: Rib-stiffened double panel case. *Journal of Sound and Vibration*, 440:256 – 276, 2019.

[79] H.-S. Kim, S.-R. Kim, B.-K. Kim, P.-S. Ma, and Y.-H. Seo. Sound transmission loss of multi-layered infinite micro-perforated plates. *J Acoust Soc Am*, 147 1:508, 2020.

[80] H.-S. Kim, P.-S. Ma, B.-K. Kim, S.-H. Lee, and Y.-H. Seo. Sound transmission loss of multi-layered elastic micro-perforated plates in an impedance tube. *Applied Acoustics*, 166:107348, 2020.

[81] A. **Chrapońska**, J. Rzepecki, C.W. Isaac, K. Mazur, and M. Pawełczyk. Spectral analysis of Macro-Fiber Composites measured vibration of double-panel structure coupled with solenoids. *Sensors*, 20:3505, 06 2020.

[82] J. Rzepecki, A. **Chrapońska**, S. Budzan, C.W. Isaac, K. Mazur, and M. Pawełczyk. Chladni figures in modal analysis of a double-panel structure. *Sensors*, 20, 07 2020.

[83] M. Pawełczyk, S. Wrona, K. Mazur, A. **Chrapońska**, and J. Rzepecki. Dwupanelowa aktywna bariera akustyczna, Polish patent application no. P.430012.

[84] M. Pawełczyk, S. Wrona, K. Mazur, A. **Chrapońska**, and J. Rzepecki. Dwupanelowa polaktywna bariera akustyczna, Polish patent application no. P.430013.

[85] M. Pawełczyk, S. Wrona, K. Mazur, A. **Chrapońska**, and J. Rzepecki. Dwupanelowa autonomiczna bariera akustyczna, Polish patent application no. P.430014.

[86] S. Wrona and M. Pawełczyk. Optimal placement of actuators for active structural acoustic control of a light-weight device casing. In *Proceedings of the Annual Congress of the International Institute of Acoustics and Vibration (IIAV), Athens, Greece, July 2016*, 07 2016.

[87] S. Wrona, K. Mazur, J. Rzepecki, A. **Chrapońska**, and M. Pawełczyk. Reduction of compressor noise by the active casing approach. In *26th International Congress on Sound and Vibration : ICSV26, Montreal, Canada, 7-11 July 2019, 2019, [b.m.], Canadian Acoustical Association, 980 s., ISBN 978-1-9991810-0-0*, 07 2019.

[88] K. Mazur, S. Wrona, A. **Chrapońska**, J. Rzepecki, and M. Pawełczyk. FXLMS with Multiple Error Switching for Active Noise-Cancelling Casings. *Archives of Acoustics*, 44(4), 2019.

[89] A. **Chrapońska**, S. Wrona, J. Rzepecki, K. Mazur, and M. Pawełczyk. Secondary paths analysis of an active casing placed at a wall. In *Proceedings of 2018 Joint Conference Acoustics, 11-14 September 2018, Ustka, Poland / Marszal J., Kochańska I. (eds.), 2018, Institute of Electrical and Electronics Engineers, pp.1-5, ISBN 978-1-5386-7115-3*, pages 1–9, 09 2018.

[90] S. Wrona, K. Mazur, J. Rzepecki, A. **Chrapońska**, and M. Pawełczyk. Resilience and energy-based analysis of an active noise-reducing casing. In *Carletti E., Crocker M., Pawełczyk Marek [et al.] (eds.): Advances in acoustics, noise and vibration - 2021 : Proceedings of the 27th International Congress on Sound and Vibration, Proceedings of the International Congress on Sound and Vibration, 2021, Politechnika Śląska, 1600 p., ISBN 978-83-7880-799-5.* Silesian University of Technology, Gliwice, 07 2021.

[91] S. Wrona and M. Pawełczyk. Feedforward control of a light-weight device casing for active noise reduction. *Archives of Acoustics*, 41:499–505, 03 2016.

[92] K. Mazur, S. Wrona, A. **Chrapońska**, J. Rzepecki, and M. Pawełczyk. Synchronized switch damping on inductor for noise-reducing casing. In *26th International Congress on Sound and Vibration : ICSV26, Montreal, Canada, 7-11 July 2019, 2019, [b.m.], Canadian Acoustical Association, 980 p., ISBN 978-1-9991810-0-0*, 07 2019.

[93] J. Rzepecki, A. **Chrapońska**, S. Budzan, C.W. Isaac, K. Mazur, and M. Pawełczyk. Chladni figures in modal analysis of a double-panel structure. *Sensors*, 20(15), 2020.

[94] S. Wrona, K. Mazur, J. Rzepecki, A. **Chrapońska**, and M. Pawełczyk. Sound transmission through a thin plate with shaped frequency response. *Archives of Acoustics*, vol. 44(No 4):731–738, 2019.

[95] K. Mazur, J. Rzepecki, A. **Chrapońska**, S. Wrona, and M. Pawełczyk. Vibroacoustical performance analysis of a rigid device casing with piezoelectric shunt damping. *Sensors*, 21(7), 2021.

[96] A. **Chrapońska**, J. Rzepecki, C.W. Isaac, K. Mazur, S. Wrona, and M. Pawełczyk. Vibroacoustical properties of a double-panel structure with stiffness-varying couplings. In *Carletti E., Crocker M., Pawełczyk Marek [et al.] (eds.): Advances in acoustics, noise and vibration - 2021 : Proceedings of the 27th International Congress on Sound and Vibration, Proceedings of the International Congress on Sound and Vibration, 2021, Politechnika Śląska,*

*1600 p., ISBN 978-83-7880-799-5*. Silesian University of Technology, Gliwice, 07 2021.

[97] J. Rzepecki, A. **Chrapońska**, K. Mazur, C.W. Isaac, S. Wrona, and M. Pawełczyk. Analysis of noise emission of a device enclosed in a rigid casing with modified double-panel wall. In *Carletti E., Crocker M., Pawełczyk Marek [et al.] (eds.): Advances in acoustics, noise and vibration - 2021 : Proceedings of the 27th International Congress on Sound and Vibration, Proceedings of the International Congress on Sound and Vibration, 2021, Politechnika Śląska, 1600 p., ISBN 978-83-7880-799-5*. Silesian University of Technology, Gliwice, 07 2021.

[98] S. Wrona and M. Pawełczyk. Shaping frequency response of a vibrating plate for passive and active control applications by simultaneous optimization of arrangement of additional masses and ribs. Part II: Optimization. *Mechanical Systems and Signal Processing*, 70-71:699 – 713, 2016.

[99] F. Xin and T. Lu. Analytical and experimental investigation on transmission loss of clamped double panels: Implication of boundary effects. *The Journal of the Acoustical Society of America*, 125:1506–17, 04 2009.

[100] Soundlabs Group Ex-1 Exciter Speaker. `https://www.soundlabsgroup.com.au/p/M-162710/EX-1+Exciter+Speaker`. Accessed: 2022-01-27.

[101] Beyerdynamic MM1 - Thomann Polska. `https://www.thomann.de/pl/beyerdynamic_mm1.htm`. Accessed: 2022-01-27.

[102] MFC (TM) P2 Type. `https://www.smart-material.com/MFC-product-P2V2.html`. Accessed: 2022-01-27.

[103] L. Leniowska and D. Mazan. MFC sensors and actuators in active vibration control of the circular plate. *Archives of Acoustics*, 40:257–265, 06 2015.

[104] M. Danesh and A. Ghadami. Sound transmission loss of double-wall piezoelectric plate made of functionally graded materials via third-order shear deformation theory. *Composite Structures*, 219:17–30, 2019.

[105] J. Eargle. *Loudspeaker handbook*, pages 96–98. Springer Science+Businness Media, LLC, 2003.

[106] R. Merz. Honeycomb speaker system, , US patent no. us9838789b2, 2017.

[107] F. Heuchel, E. Fernandez-Grande, F. Agerkvist, and E. Shabalina. Active room compensation for sound reinforcement using sound field separation techniques. *The Journal of the Acoustical Society of America*, 143:1346–1354, 03 2018.

[108] T. Zechner. *Room Acoustics in Home Theaters*. PhD thesis, Graz University of Technology, 02 2014.

[109] M. Long. 18 - sound reinforcement systems. In M. Long, editor, *Architectural Acoustics (Second Edition)*, pages 673 – 721. Academic Press, Boston, second edition edition, 2014.

[110] M. Long. 21 - design of studios and listening rooms. In M. Long, editor, *Architectural Acoustics (Second Edition)*, pages 829 – 871. Academic Press, Boston, second edition edition, 2014.

[111] H. Kuttruff. *Room Acoustics, Fifth Edition*. Taylor & Francis, 2009.

[112] Sound Absorption Coefficient Chart | JCW Acoustic Supplies. `https://www.acoustic-supplies.com/absorption-coefficient-chart/`. Accessed: 2022-01-27.

[113] Free 3D Modeling Software | 3D Design Online | SketchUp Free Subscription. `https://www.sketchup.com/plans-and-pricing/sketchup-free`. Accessed: 2022-02-03.

[114] S. Pietrzko. *Contributions to Noise and Vibration Control Technology*. AGH University of Science and Technology: Cracow, Poland, 2009.

[115] K. Mazur, S. Wrona, and M. Pawełczyk. Design and implementation of multichannel global active structural acoustic control for a device casing. *Mechanical Systems and Signal Processing*, 98:877–889, 2018.

[116] K. Mazur and M. Pawełczyk. Internal model control for a light-weight active noise-reducing casing. *Archives of Acoustics*, 41, 03 2016.

[117] P.A. Nelson and S.J. Elliott. *Active Control of Sound*. Elsevier Science, 1992.

[118] D. Bismor, K. Czyż, and Z. Ogonowski. Review and comparison of variable step-size LMS algorithms. *The International Journal of Acoustics and Vibration*, 21:24–39, 03 2016.

[119] A. Barkefors, M. Sternad, and L.-J. Brannmark. Design and analysis of linear quadratic gaussian feedforward controllers for Active Noise Control. *Audio, Speech, and Language Processing, IEEE/ACM Transactions on*, 22:1777–1791, 12 2014.

[120] Y. Jiang, S. Chen, H. Meng, Z. Zhou, and W. Lv. A novel adaptive step-size hybrid active noise control system. *Applied Acoustics*, 182:108285, 2021.

[121] W. Li, W. Wang, B. Li, and Z. Yang. Error signal differential term feedback enhanced variable step size FxLMS algorithm for piezoelectric active vibration control. *Shock and Vibration*, 2020.

[122] S. Elliott, I. Stothers, and P. Nelson. A Multiple Error LMS algorithm and its application to the active control of sound and vibration. *Acoustics, Speech and Signal Processing, IEEE Transactions on*, ASSP-35:1423 – 1434, 11 1987.

[123] S. Wrona, K. Mazur, and M. Pawełczyk. Internal model control of a washing machine casing for active noise reduction. In *24th International Congress on Sound and Vibration, London, United Kingdom*, 07 2017.

[124] Krzysztof Mazur, Stanislaw Wrona, and Marek Pawelczyk. Design and implementation of multichannel global active structural acoustic control for a device casing. *Mechanical Systems and Signal Processing*, 98:877–889, 2018.

[125] J. Wiora, S. Wrona, and M. Pawełczyk. Evaluation of measurement value and uncertainty of sound pressure level difference obtained by active device noise reduction. *Measurement*, 96:67–75, 2017.

[126] R.R. Leitch and M.O. Tokhi. Active noise control systems. *IEE Proceedings A (Physical Science, Measurement and Instrumentation, Management and Education, Reviews)*, 134:525–546(21), June 1987.

[127] G. Weinreich and E.B. Arnold. Method for measuring acoustic radiation fields. *The Journal of the Acoustical Society of America*, 68(2):404–411, 1980.

[128] B. Rafaely. Analysis and design of spherical microphone arrays. *IEEE TRANSACTIONS ON SPEECH AND AUDIO PROCESSING*, 13(1):135–143, JAN 2005.

[129] G.B. Arfken and H.J. Weber. *Mathematical methods for physicists*. Elsevier Acad. Press, 2008.

[130] R.H. Hardin and N.J.A. Sloane. Mclaren's improved snub cube and other new spherical designs in three dimensions. *Discrete & Computational Geometry*, 15(4):429–441, Apr 1996.

[131] K. Mazur and M. Pawełczyk. Active noise-vibration control using the filtered-reference LMS algorithm with compensation of vibrating plate temperature variation. *Archives of Acoustics*, 36(1):65–76, 2011.

[132] O. Hassan and J. Davy. Building acoustics and vibration: Theory and practice. *The Journal of the Acoustical Society of America*, 127:1168, 02 2010.

[133] O.E.V. Kaiser. *Active control of sound transmission through a double wall structure*. PhD thesis, ETH Zürich, 2001.

[134] M. Risoud, J.-N. Hanson, F. Gauvrit, C. Renard, P.-E. Lemesre, N.-X. Bonne, and C. Vincent. Sound source localization. *European Annals of Otorhinolaryngology, Head and Neck Diseases*, 135(4):259–264, 2018.

[135] S. Timoshenko and W. Woinowski-Krieger. *Theory of Plates and Shells*. McGraw-Hill, New York, 2 edition, 1959.

[136] D.J. Gorman. *Free Vibration Analysis of Rectangular Plates*. Elsevier, New York, 1982.

[137] G.B. Chai. Free vibration of rectangular isotropic plates with and without a concentrated mass. *Computers & Structures*, 48(3):529–532, 1993.

[138] S. Alisjahbana. Dynamic response of clamped orthotropic plates to dynamic moving loads. In *The 13 World Conference on Earthquake Engineering, Vancouver, BC, Canada*, 08 2004.

[139] I.B. Elishakoff. Vibration analysis of clamped square orthotropic plate. *AIAA Journal*, 12(7):921–924, 1974.

[140] T. Sakata, K. Takahashi, and R.B. Bhat. Natural frequencies of orthotropic rectangular plates obtained by iterative reduction of the partial differential equation. *Journal of Sound and Vibration*, 189(1):89–101, 1996.

[141] R. Assaf and E. Elhachem. Noise and vibration pollution: Analytical analysis of double-leaf partition. *Energy Procedia*, 74:1265 – 1273, 2015. The International Conference on Technologies and Materials for Renewable Energy, Environment and Sustainability –TMREES15.

[142] R.J.M. Craik and R.S. Smith. Sound transmission through double leaf lightweight partitions part I: airborne sound. *Applied Acoustics*, 61(2):223 – 245, 2000.

[143] T. Fu, Z. Chen, H. Yu, Z. Wang, and X. Liu. An analytical study of sound transmission through stiffened double laminated composite sandwich plates. *Aerospace Science and Technology*, 82-83:92 – 104, 2018.

[144] W. Larbi, J.F. Deü, and R. Ohayon. Vibroacoustic analysis of double-wall sandwich panels with viscoelastic core. *Computers & Structures*, 174:92 – 103, 2016. CIVIL-COMP.

[145] Q. Mao and S. Pietrzko. Experimental study for control of sound transmission through double glazed window using optimally tuned Helmholtz resonators. *Applied Acoustics*, 71(1):32 – 38, 2010.

[146] W. Larbi, J. Deü, and R. Ohayon. Finite element reduced order model for noise and vibration reduction of double sandwich panels using shunted piezo-

electric patches. *Applied Acoustics*, 108:40 – 49, 2016. Applied Acoustics in Multiphysic systems.

[147] A. Jakob and M. Möser. Active control of double-glazed windows. part I: Feedforward control. *Applied Acoustics*, 64(2):163 – 182, 2003.

[148] M. Mohri, A. Rostamizadeh, and A. Talwalkar. *Foundations of Machine Learning*. MIT press, Cambridge, 2nd edition, 2018.

[149] G.D. Hutcheson. Ordinary least-squares regression. In *The SAGE Dictionary of Quantitative Management Research*, pages 224–228. SAGE Publications Ltd, London, 1st edition, 2011.

[150] N. Joshi, G. Singh, S. Kumar, R. Jain, and P. Nagrath. Airline prices analysis and prediction using Decision Tree Regressor. In *International Conference on Recent Developments in Science, Engineering and Technology*, pages 170–186. Springer, 2019.

[151] M. Segal. Machine learning benchmarks and Random Forest regression. In *Technical Report, Center for Bioinformatics & Molecular Biostatistics, University of California, San Francisco*, pages 1–14, 2003.

[152] A. Stenger and R. Rabenstein. Adaptive Volterra filters for nonlinear acoustic echo cancellation. In *NSIP*, 1999.

[153] U.F. Siddiqi and S.M. Sait. A neighborhood search-based heuristic for the fixed spectrum frequency assignment problem. *Arabian Journal for Science and Engineering*, 44(4):2985–2994, 2019.

[154] scikit-learn: machine learning in python — scikit-learn 1.0.2 documentation. `https://scikit-learn.org/stable/`. Accessed: 2022-01-27.

[155] S.B. Lee, X. Gui, M. Manquen, and E.R. Hamilton. Use of training, validation, and test sets for developing automated classifiers in quantitative ethnography. In *International Conference on Quantitative Ethnography*, pages 117–127. Springer, 2019.

# Index